Range-based Navigation of AUVs Operating Near Ship Hulls

by

Michael A. Kokko

Submitted to the Department of Mechanical Engineering
in partial fulfillment of the requirements for the degree of

Master of Science in Mechanical Engineering

at the

MASSACHUSETTS INSTITUTE OF TECHNOLOGY

June 2007

Author . . . . . .
Department of Mechanical Engineering
May 21, 2007

Certified by . . . . . .
Dr. Franz S. Hover
Principal Research Engineer
Thesis Supervisor

Certified by . . . . . .
Dr. John J. Leonard
Associate Professor
Thesis Supervisor

Accepted by . . . . . .
Dr. Lallit Anand
Graduate Officer, Department of Mechanical Engineering

Range-based Navigation of AUVs Operating Near Ship Hulls

by

Michael A. Kokko

Submitted to the Department of Mechanical Engineering
on May 21, 2007, in partial fulfillment of the
requirements for the degree of
Master of Science in Mechanical Engineering

Abstract

In-water ship hull inspection is essential for both routine preventative maintenance as well as for timely detection and neutralization of limpet mines planted on military and commercial vessels. While a host of inspection methods have been proposed for this task, Autonomous Underwater Vehicles (AUVs) are particularly well-suited for such missions as they require neither constant human supervision nor a restrictive tether as do Remotely Operated Vehicles (ROVs). MIT and Bluefin Robotics have jointly developed a Hovering AUV (HAUV) for the inspection of ship hulls and other submerged marine structures which has been successfully demonstrated to achieve a coverage rate on the order of 700m^2/hour with centimeter-scale resolution for a variety of hull types.

AUV navigation often involves dead reckoning based on velocity measurements from an acoustic Doppler Velocity Log (DVL) sensor. As this strategy is inherently susceptible to drift, related efforts seek to generate vehicle position updates through either Simultaneous Localization and Mapping (SLAM) or the use of external sensor networks. In this work we propose a unique localization approach which relies on range measurements taken to surfaces of known curvature. The algorithm is developed for navigating relative to simple parabolic curvatures and is tested both in simulation and on a floating raft robot. Localization and servoing are demonstrated in real-time to achieve estimated position deviations within millimeters of their expected values.

In addition to exploring other facets of hull-relative navigation, this thesis also documents a significant mechanical redesign of certain HAUV components.

Thesis Supervisor: Dr. Franz S. Hover
Title: Principal Research Engineer

Thesis Supervisor: Dr. John J. Leonard
Title: Associate Professor

Acknowledgments

The past two years here at MIT have flown by and there are many people who have helped make this a successful experience. First of all, I am immensely grateful to my advisors Dr. Franz Hover and Dr. John Leonard for their support and for all the opportunities they have provided. Additionally, Matt Walter, Jacques Leederkerken, Andrew Patrikalakis, Dan Walker, and Rob Williams helped get me up to speed on work in the marine robotics field and gave me invaluable advice on various technical aspects of my projects. I also worked closely with many Bluefin Robotics employees on the HAUV and HAUV1B vehicles including Jerome Vaganay, Mike Elkins, and Steve Summit.

In addition to my research I took six classes at MIT including both Mechatronics and Digital Control Systems with Professor David Trumper. These were probably two of the toughest (or at least most time-consuming!) courses of my college career, but I learned a great deal from Professor Trumper and appreciate his dedication to teaching and commitment to practical, hands-on learning.

Aside from research and classes I have also been very involved with the MIT Outing Club during the course of my graduate studies. I've been hooked ever since my introductory 32.5 mile Pemi Loop day hike and it seems that there were always MITOC folks ready to head up to New Hampshire for much-needed weekend breaks from school. These same crazy folks also encouraged me to start running marathons, and with three under my belt I seem to be hooked on that now as well. Without this balance of work and play earning a master's degree would have been much more difficult.

As always, I also appreciate the endless support from my friends and family. My parents have always stood by me and have provided a steady supply of gluten-free nourishment which has helped me through many late nights of drawing bode plots and debugging MATLAB code. Leaving MIT will be bittersweet, but I look forward to future projects, learning, and adventures in the working world.

Contents

List of Figures

List of Tables

Chapter 1

Introduction

This thesis considers the problem of Autonomous Underwater Vehicle (AUV) navigation as it relates to inspecting ship hulls. Chapter 1 explains the ship hull inspection problem as well as the Hovering AUV (HAUV) platform for which navigation algorithms are later developed. An improved design for the HAUV is presented in Chapter 2 and Doppler Velocity Log (DVL) range-based algorithmic development for navigation is covered in Chapter 3. While the main algorithm in Section 3.3 performs localization using range measurements to a known curved surface, additional ideas are also explored which seek to expand these techniques to identifying sharp target features whose locations can be extracted and used in a Simultaneous Localization and Mapping (SLAM) framework. Chapter 4 describes a platform which was developed to test real-time range-based navigation and also presents results from the algorithms developed in Chapter 3. Finally, applications to the HAUV are discussed.

1.1 Overview of Ship Hull Inspection

With a recent rise in highly-publicized, global terrorist activities, the national and international communities have become increasingly focused on security, especially within the transportation sector. The World Trade Center attacks of September 11, 2001, for example, immediately and drastically changed the daily operations of the commercial airline industry. Although somewhat less publicized, port and har-

bor security has also increased in response to both specific and perceived threats. Authorities including the United States Navy and the North Atlantic Treaty Organization (NATO) are particularly concerned with terrorists affixing limpet mines to ship hulls prior to arrival in port. This concern is amplified by the knowledge that many seaports are located in close proximity to both major population centers and storage facilities for hazardous and explosive materials.

In response to this threat, the US Navy now inspects the hulls of its ships using teams of trained divers. Although effective, this method is dangerous and time consuming, and it requires a large number of divers to achieve 100% coverage in typically murky harbor conditions. Since improving the safety and efficiency of these inspections is a high priority item for the Navy, the Office of Naval Research is currently funding an array of research initiatives to tackle this problem. Proposed inspection technologies include hand-held sonar systems, pole-mounted sensors, Remotely-Operated Vehicles (ROVs), and Autonomous Underwater Vehicles (AUVs). The present effort is concerned with the development, navigation, and control of a hovering AUV for ship hull inspection.

1.2 HAUV Background

1.2.1 Vehicle History and Development

The Hovering Autonomous Underwater Vehicle (HAUV) was developed by the MIT Sea Grant College Program in conjunction with Bluefin Robotics beginning around the fall of 2002. The prototype vehicle measures roughly 1.0m x 0.7m x 0.4m and weighs around 100kg [18, 17]. Equipped with both a DVL and a Sound Metrics DIDSON imaging sonar, the HAUV has been designed to servo laterally along a ship hull, inspecting its surface for the presence of mines. Since both compass and GPS signals are useless in these conditions, the HAUV integrates velocity estimates derived from DVL beam measurements to track its position along the hull. Meanwhile, the DIDSON captures high-resolution imagery which can later be reconstructed in the

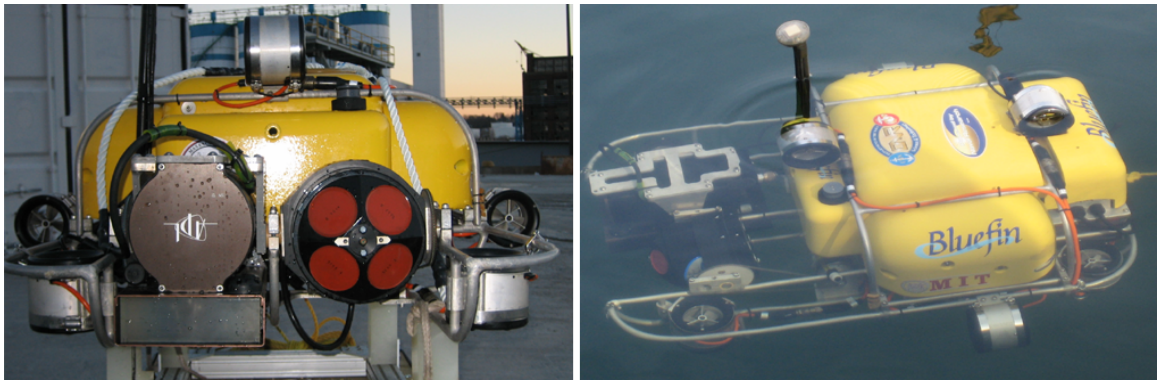

Figure 1-1: Two views of the Hovering Autonomous Underwater Vehicle (HAUV). The starboard sensor is a Dual-frequency IDentification SONar (DIDSON) and the port is a Doppler Velocity Log (DVL).

form of a mosaic to view the entire inspection area.

1.2.2 Structure and Systems of the HAUV

Mechanical Structure

As shown in Figure 1-1, the HAUV components are affixed to a frame fabricated from welded $\frac{1}{2}''$ aluminum rod. The weight of the vehicle is offset by a polyurethane foam shell which attaches by means of a hinged, cage-like frame. Once deployed, the vehicle is trimmed with small ballast weights to eliminate any static roll or pitch and to achieve a slightly positive buoyancy.

Sensors

The DIDSON and DVL are both mounted in sensor bays in the forward section of the HAUV (see Figure 1-1). The two sensors are coupled to separate pitch actuators by means of chain and sprocket transmissions which control their vehicle-relative pitches. In addition to the DIDSON and DVL, the vehicle is equipped with an altimeter, a GPS receiver, a Leica DMC-SX magnetic compass, and a Honeywell HG1700 inertial measurement unit which all reside within the Main Electronics Housing (MEH). Each of the two main sensors are described in detail below:

- **DIDSON Imaging Sonar:** The primary sensor aboard the HAUV is a Dual Frequency Identification Sonar (DIDSON) from Sound Metrics Corp of Chesapeake, VA. The DIDSON is an expensive (roughly $80K) sensor which provides the acoustic equivalent of video imagery in environments where the use of standard optical vision is impractical. As implied by its name, the DIDSON can operate at either 1.1MHz or 1.8MHz. In the present application, frames are captured at 5Hz.

- **DVL:** The Doppler Velocity Logger (DVL) from Teledyne RDI is a four-beam 1200kHz sonar sensor which is widely employed in the marine industry to measure either the velocity profile of a water column or the relative motion between a water craft and a fixed surface (i.e., the sea floor). A DVL is used on the HAUV for the latter purpose, tracking its motion relative to a target ship hull. The sensor communicates with the vehicle over a standard serial interface and data is available at roughly 10Hz.

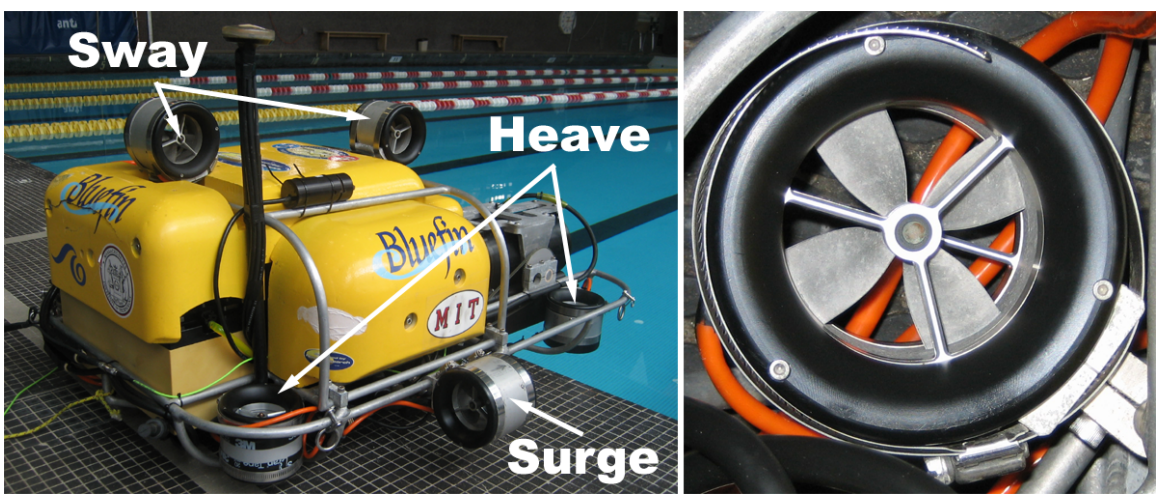

Figure 1-2: Placement of the HAUV thrusters (left) and a close-up of a single thruster (right). Note that the surge and heave thrusters are symmetric on either side of the vehicle.

Actuators

The HAUV is actuated by means of eight custom electric thrusters from UK-based TSL Technology. These thrusters are unique in that they are hub-less, that is the propeller is itself the rotor. Manufacturer specifications indicate that 50N of thrust is available from each unit at 100W[1]. The eight thrusters are arranged on the vehicle as follows: four are placed at the corners of the vehicle for control authority in the heave direction, two are placed a-midships extending from either side of the vehicle for surge propulsion, and two are secured above the foam to exert force in the sway direction (see Figure 1-2). All eight thrusters are connected to a custom control board which was also produced by TSL Technology. Detailed information regarding the design and performance of the thrusters used on the HAUV is available in [13].

Electronics

The computational center of the HAUV is a PC104-type CPU which is contained within the MEH. This computer runs Debian Linux and controls the vehicle through a proprietary Bluefin software package named Huxley. Communication with the vehicle can be established via a radio frequency (RF) modem, wireless ethernet, or a fiber optic tether; however, communication is unnecessary once a mission has been initiated as the system is fully autonomous. In addition to the MEH, a junction box within the vehicle houses the thruster control board. All components are powered by a 1.5kWh lithium polymer battery supplied by Bluefin.

1.2.3 Inspection with the HAUV

The process of inspecting a ship hull with the HAUV involves autonomous vehicle navigation relative to the target coupled with the recording of DIDSON imagery. At this point the focus is primarily on navigation and assurance of complete coverage rather than mine detection within individual frames of sonar data. Typically the

[1]The original thruster specifications indicate that the design was capable of 200W per channel. As of April 2007, TSL has revised this specification downward to 100W.

vehicle runs autonomously according to a pre-programmed mission plan, but operators maintain a tethered fiber-optic connection to the vehicle for the sole purpose of displaying real-time DIDSON imagery.

Upon deployment, the HAUV has the ability to operate just below the surface of the water where it generally receives relatively good GPS position updates. The vehicle can thus travel to a prescribed location if it is not deployed near the target ship hull. Once in proximity of the inspection site, the vehicle dives and surges towards the hull until DVL lock is achieved. From this point forward, the HAUV attempts to remain normal to the ship hull in its yaw direction, parallel to the sea floor in the roll and pitch directions, and offset from the hull by a fixed distance on the order of 1m.

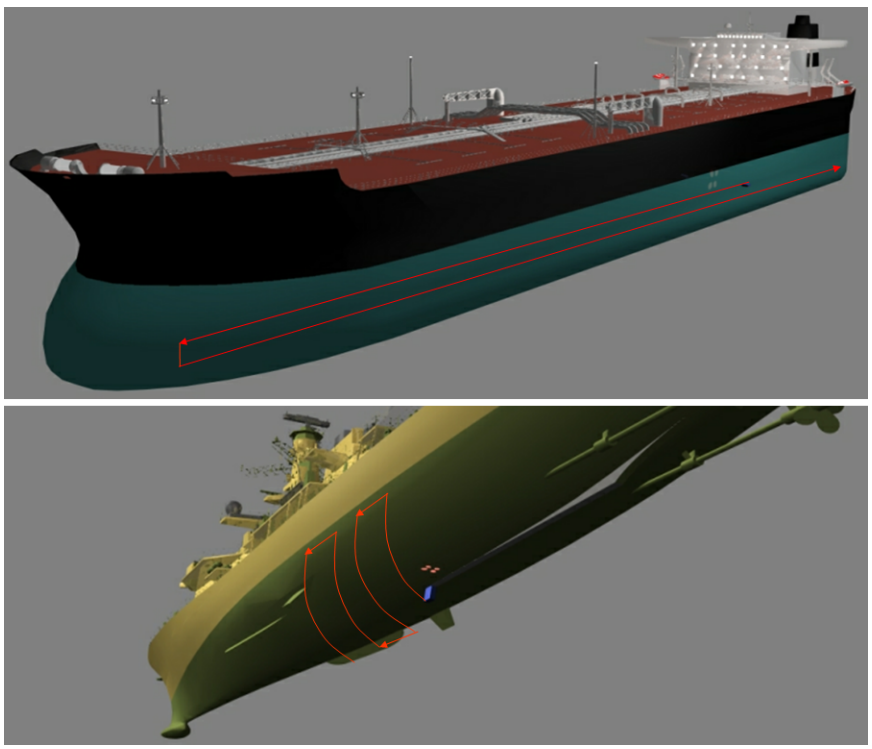

Figure 1-3: Horizontal slicing (top) and vertical slicing (bottom) inspection methods. Images courtesy of the MIT Sea Grant Program. This figure has also appeared in [18, 17].

The actual survey procedure can be performed in either horizontal or vertical slices as shown in Figure 1-3. Most commonly, the HAUV begins by transiting the length of the inspection area in the sway direction at its initial depth. The vehicle

then follows the hull curvature downward for approximately 1m and transits back along the length of the inspection area. This horizontal slicing process is repeated until a preset maximum depth is achieved. Vertical slicing is similar except that the HAUV initially dives to the maximum depth, then transits a short distance along the hull laterally, and finally returns to its initial depth. Vertical slices continue until the vehicle reaches the end of the inspection area.

During the inspection process the DVL is pitched so that it remains normal to the ship hull. Likewise, the DIDSON grazing angle is maintained at roughly 20° for optimal image quality. Figure 1-4 illustrates the relative positioning of the two sensors at various depths relative to the target ship hull.

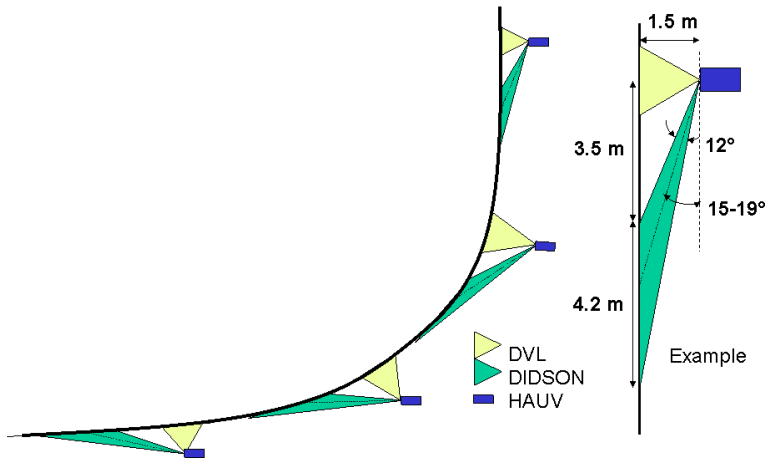

Figure 1-4: Relative positioning of the DIDSON and DVL sensors throughout a vertical slice. Image courtesy of MIT Sea Grant and Bluefin Robotics. This figure has also appeared in [18, 17].

1.2.4 Recent Vehicle Demonstrations

HULSFest in San Diego, California

The HAUV was among several autonomous and remotely-operated vehicles to demonstrate its capabilities at HULSFest 2006 which was held at SPAWAR SCSD in San Diego during late February and early March. During this exhibition, the HAUV in-

spected the flat-bottomed R/V *Acoustic Explorer* (see Figure 3-1) which was rich with features including cooling fins, zinc anodes, and purposely-placed Mine-Like Objects (MLOs). The vehicle successfully inspected its target area on several occasions and retrieved sonar imagery of potential mines. Figure 1-5 shows a horizontal slice mosaic constructed using vehicle navigation data from one of the HULSFest missions. Many additional details regarding the HAUV's performance at HULSFest can be found in [17].

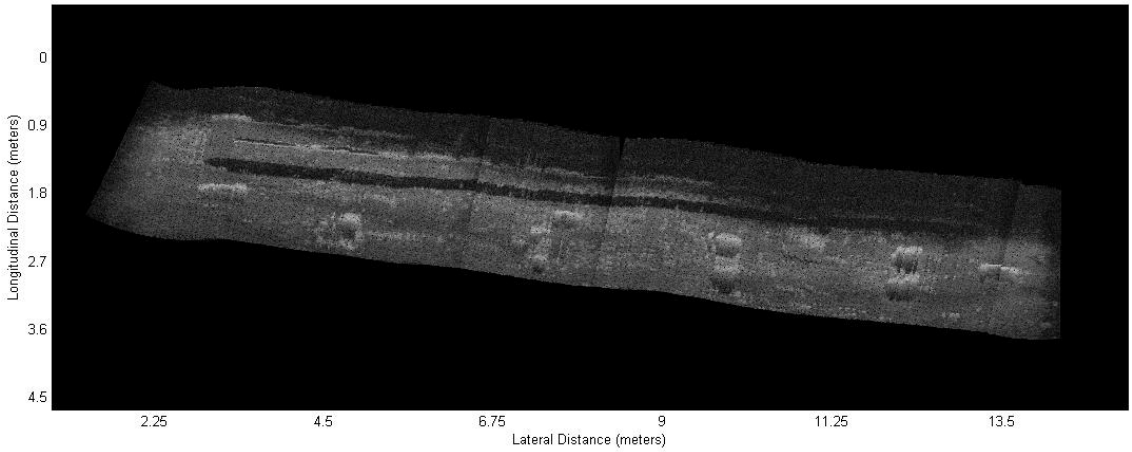

Figure 1-5: Mosaic of DIDSON imagery from an inspection run at HULSFest. This mosaic and others from recent HAUV trials were constructed using a MATLAB script which assembles DIDSON frames based solely on vehicle navigation data. No feature matching or image processing algorithms were employed to create these mosaics.

Harbor Protection Trials in LaSpezia, Italy

In March of 2006 NATO held a Harbor Protection Trial at an Italian naval base in LaSpezia. During this demonstration the HAUV inspected a large section of a moored SAURO-class submarine. While the HAUV had not previously operated on a hull with such high curvature, the demonstration was relatively successful and the HAUV achieved good coverage and completed its mission despite a loss of shore power at the operator's station. Additional information on this demonstration is available in [17].

Figure 1-6: The HAUV (circled in red) inspecting a submarine at the 2006 HPT demo in LaSpezia, Italy. This mission lasted roughly 15 minutes during which the vehicle performed five horizontal slices along the forward 30 meters of the hull [17].

1.2.5 Current Development Initiatives

Throughout the vehicle's early development, the HAUV team focused on inspecting only the larger, relatively un-contoured sections of ship hulls. While these areas can now be inspected with relative ease, navigation in areas with high curvature or numerous protrusions (i.e., running gear) presents much more of a technical challenge. Standard velocity-based navigation is not an option in these areas as the DVL cannot obtain a meaningful lock on complex geometric structures. Additionally many hazards and obstacles are present in such environments that must be avoided.

There is a definite need to inspect the more complicated areas of ship hulls, so the HAUV team is now focused on implementing DIDSON and vision -based Simultaneous Localization and Mapping (SLAM) algorithms for navigation. Additionally, Section 3.3 of this thesis presents a method of utilizing DVL *range* returns to localize

the vehicle relative to a surface of known curvature.

Chapter 2

Design of the HAUV1B

In the fall of 2005, an effort was undertaken to redesign certain mechanical aspects of the HAUV. Of specific interest were reducing the vehicle's size and weight with the intent that eventually a single person will be able to transport and deploy the inspection system. The project team also identified that streamlining the body foam and relocating thrusters to reduce undesired moment arms could result in significant efficiency improvements. A new welded aluminum frame and polyurethane foam shell were designed and fabricated with the intention of integrating all existing internal components (electronics, thrusters, battery, etc) into the new 'HAUV1B.' After the frame and foam had been fabricated, however, it was decided that having two operational vehicles would be beneficial and Bluefin Robotics assumed responsibility for constructing the HAUV1B. This section details the process by which the new frame and foam were designed.

2.1 Design Requirements

As mentioned above, several requirements were identified for the HAUV1B mechanical design:

1. **Reduce vehicle weight:** The initial HAUV prototype weighs approximately 100kg (220 lb.) which makes it impractical to deploy alone and even difficult with two people when the vehicle must be lowered into the water or raised back

out. In addition to making deployment more manageable, reducing the vehicle mass and inertia would lower the thruster power requirements and increase battery life. Specific component weights are shown Table 2.1.

Component	**kg**
Battery	14.9
Foam	12.2
Ballast Weight	10.4
Thrusters (8)	10.1
Main Electronics Housing	8.9
DIDSON	7.2
DVL	6.3
Oil in Junction Box	5.6
Pitch Actuators (2)	4.2
Junction Box Cover	2.5
Junction Box Bottom	?
Chassis	?
Wet Cabling	?
Total Measured Weight	82.3
Net Vehicle Measured Weight	103.9
Unallocated Weight	21.6

Table 2.1: HAUV component weights as measured by Bluefin Robotics. Note that not all components were weighed, thus, there is a discrepancy between the total vehicle weight and the sum of its component weights.

2. **Reduce vehicle volume:** In addition to being heavy, the HAUV takes up a lot of space. This again makes the vehicle awkward to transport and deploy. It should be noted that an explicit relationship exists between weight and volume in that the vehicle must be maintained at roughly neutral buoyancy ($\rho_{net} \approx 1000\text{kg/m}^3$). Since this target density is achieved by adding syntactic foam once the main vehicle weight has been established, a lighter vehicle should by definition occupy less volume.

3. **Streamline foam body:** As seen in Figure 1-1, the original HAUV foam is large and boxy when viewed from any direction. While the foam for the HAUV1B must serve the same purpose, it was desired that this foam be better distributed and contoured such that the vehicle assumes a more streamlined

profile, especially in the sway direction for efficient horizontal slicing (see Section 1.2.3).

4. **Reposition thrusters:** Many of the thrusters on the HAUV are positioned at significant distances from the vehicle's center of mass. This can be useful for making pitch, roll, or yaw adjustments; however, poor thruster placement can create undesired moments which must be counteracted with additional effort. The two sway thrusters, for example, are mounted near the top of the vehicle which induces a roll moment whenever the vehicle transits in the sway direction. This roll must be counteracted by increasing power to at least two of the heave thrusters. Since horizontal surveys require long stretches of sway motion (see Section 1.2.3), relocating these thrusters could provide substantial energy savings and thereby increase the maximum mission duration.

In addition, the most consequential design constraint was imposed by the initial assumption that all existing internal vehicle components would be integrated into the new HAUV1B. Thus, components were essentially fixed in size and could only be rearranged within the design volume.

2.2 The Design Process

Sensors lie at the heart of the ship hull inspection problem, so the HAUV1B design began with consideration of the vehicle's sensing requirements. As outlined in Section 1.2.1, the HAUV relies on a DIDSON imaging sonar to record acoustic 'video' of the target ship hull and a DVL for hull-relative navigation. Given the relatively large size of these two sensors and the functional necessity for them to face the target hull, it was decided that the original vehicle's adjacent sensor bay layout should be carried directly into the new design.

With the sensor bay remaining mostly unchanged, the other internal components could then be distributed within the desired vehicle volume. To the extent that it was possible, these components were arranged to align the net centers of mass and volume

in the horizontal plane close to the vehicle's geometric center. For this reason, the battery was placed as far aft as possible. Other lighter components like the junction box were positioned with emphasis on ease of access and minimization of cabling.

Revising the thruster placement was one of the major HAUV1B design criteria, and a good deal of effort went into choosing new locations to minimize both stream interactions and force moment arms. Most of the HAUV's survey motion occurs in the lateral (cross-body) direction, so it was especially important to place the sway thrusters close to the vertical center of mass. It should also be noted that thrusters were mounted in such a way that they can remain in place when removing the foam body. Since the most logical placement for the surge thrusters fell outside the space of the frame, pockets were designed into the new foam to allow for these two actuators to be rotated inward during transport.

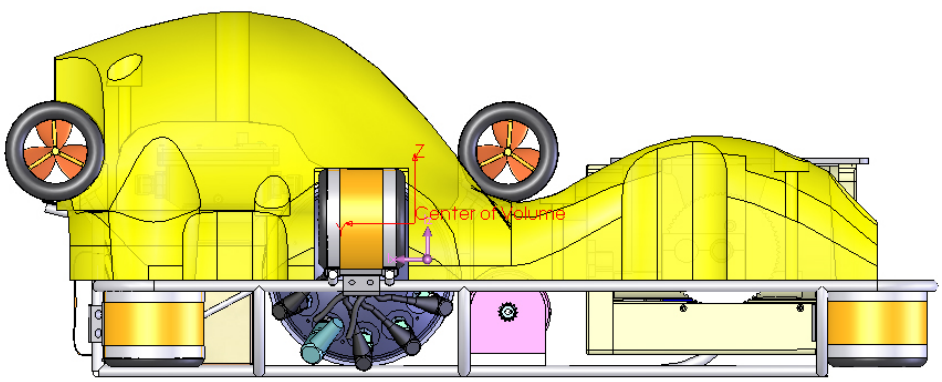

Figure 2-1: An example of aligning the centers of mass and volume (buoyancy) in the HAUV1B design. In this case, more foam is needed forward of the center of mass to eliminate a small forward pitching moment.

The HAUV1B frame was constructed from welded $\frac{1}{2}''$ aluminum rod as was the initial prototype vehicle. The overall weight of the structure (14.2lb for the new design) is fairly small compared to the other vehicle components. Aluminum round-stock was chosen as it is much cheaper and easier to form than composites which may have provided some additional weight savings. For future, mass-produced HAUV designs, it may become cost effective to switch to a lighter material and fabricate the frame by another means (i.e., plastic injection-molding, heat forming, or use of

composite materials).

Once all internal components had been positioned relative to the new frame, the external foam body was designed. In accordance with the design requirements explained in Section 2.1, the foam was contoured in a streamlined fashion (especially in the sway direction). Figure 2-2 illustrates the evolution of the HAUV1B body with the final design pictured in the lower right. While manufacturing costs increase rapidly for complex geometries, these expenses are justified in the case of the HAUV1B in that they represent only a small fraction of the overall vehicle cost.

The general foam design required some fine tuning in order to balance and trim the vehicle model. Since an exact vehicle weight was unknown, extra foam was added generously with the knowledge that it is easier to machine an internal cavity than it is to add foam to a highly-contoured shell during assembly. Figure 2-1 shows that a significant righting moment was maintained while trimming the pitch. In the end, seven pieces of foam were designed: the main body, two upper arms, two lower arms, an MEH cradle, and a battery shim. These seven pieces have a combined volume of 0.04621m^3 and a mass of 11.1kg; however, not all of the foam was needed on the final vehicle due to the conservative nature of the design.

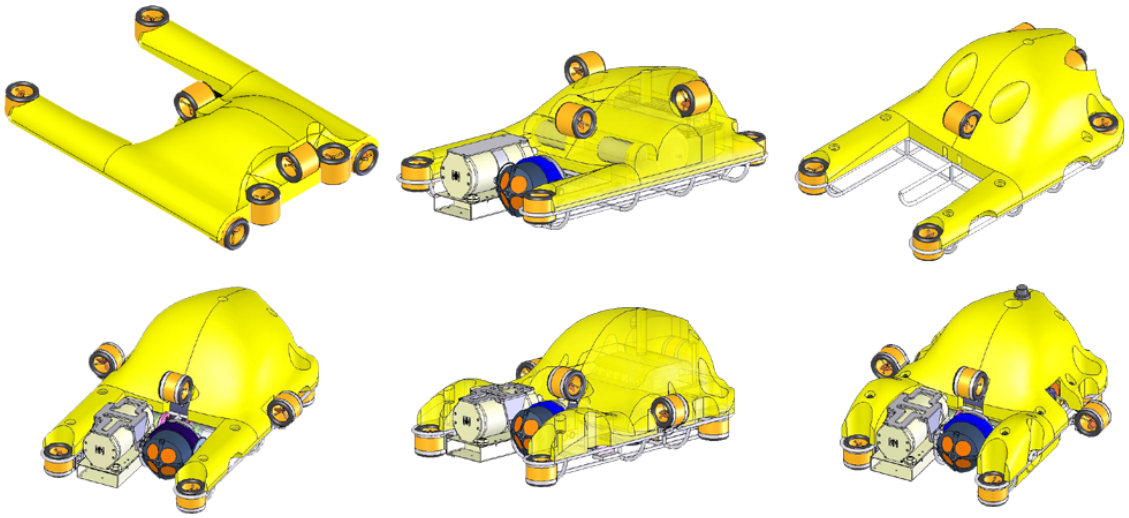

Figure 2-2: Foam and frame design iterations (left to right, top to bottom): initial foam layout, foam and frame together, through-body thruster option, flat-arm foam design, contoured-arm foam design, and the final design with upper and lower contoured arm foam.

Other features incorporated into the HAUV1B design include:

- Battery is easily accessible without removing any foam
- Foam is removable in pieces without the need for a second 'cage' frame
- Four lifting points were added

2.3 Final Design

Figure 2-3 illustrates the final HAUV1B vehicle design. Unfortunately significant weight and volume reductions were not realizable due largely to the constraint that all sensors and internal components were to be reused. With the bulk of the vehicle mass fixed, a corresponding volume of foam had to be added to achieve neutral buoyancy. The new vehicle is roughly 3″ shorter in length and 1″ narrower in width than the original prototype (see Figure 2-4). The projected HAUV1B weight is roughly 10kg lighter than the HAUV due mostly to component modifications made by Bluefin during the HAUV1B design process. To achieve a significantly lower vehicle weight and volume, internal components must all be examined and redesigned; simply revising the external packaging can not possibly have a dramatic effect.

2.4 Fabrication

The HAUV1B foam and frame were both fabricated in the spring of 2006. The MIT Central Machine Shop welded the aluminum frame and Ideal Instrument of Canton, MA machined the seven-piece foam ensemble using General Plastics R-3315 Last-A-Foam[1]. During the fabrication process, the project sponsor decided to transfer responsibility for completing the HAUV1B to personnel at Bluefin Robotics. Thus, after initial fit checks and slight modifications, Bluefin ordered the remaining internal components and assembled the new vehicle. Figure 2-5 shows the HAUV1B being assembled in the Bluefin laboratory.

[1]Specifications for this 240kg/m^3 rigid polyurethane foam are available online from General Plastics at http://www.generalplastics.com/uploads/pdf/R3315.pdf

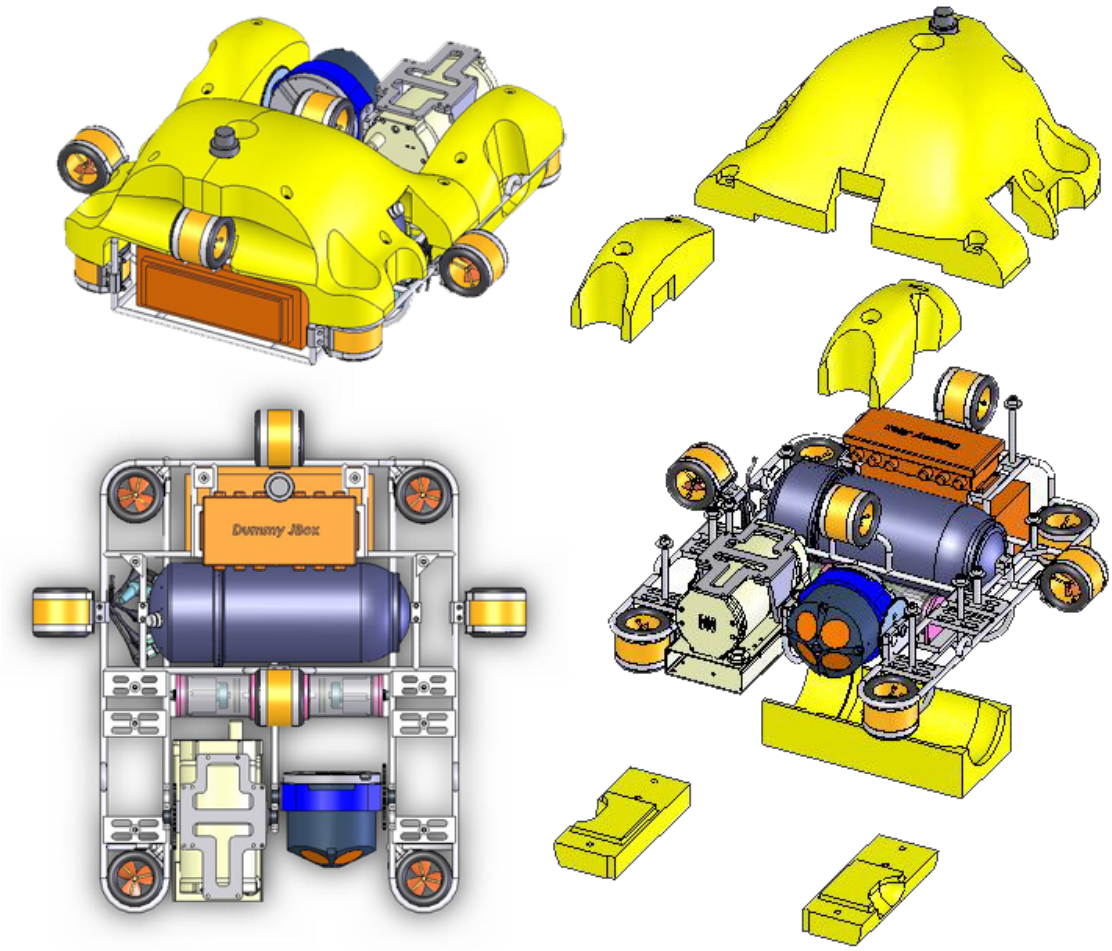

Figure 2-3: Final CAD design of the HAUV1B.

2.5 Status and Future Work

At the time of this writing, the HAUV1B had been assembled and tested in controlled environments. Initial wet tests were performed in a tank at MIT during which the thruster mapping matrix (similar to $\mathbf{M}^+$ in (3.11) and (3.15)) and independent compensators for roll, pitch, yaw, and depth were tuned. Once the mapping matrix was corrected to reflect the differences between HAUV and HAUV1B thruster locations, the individual controllers required very little tuning. Data from the final tuning tank test are provided in Figure 2-6. The HAUV1B is scheduled to appear in hull inspection demonstrations at AUVFest in Panama City, FL during the month of

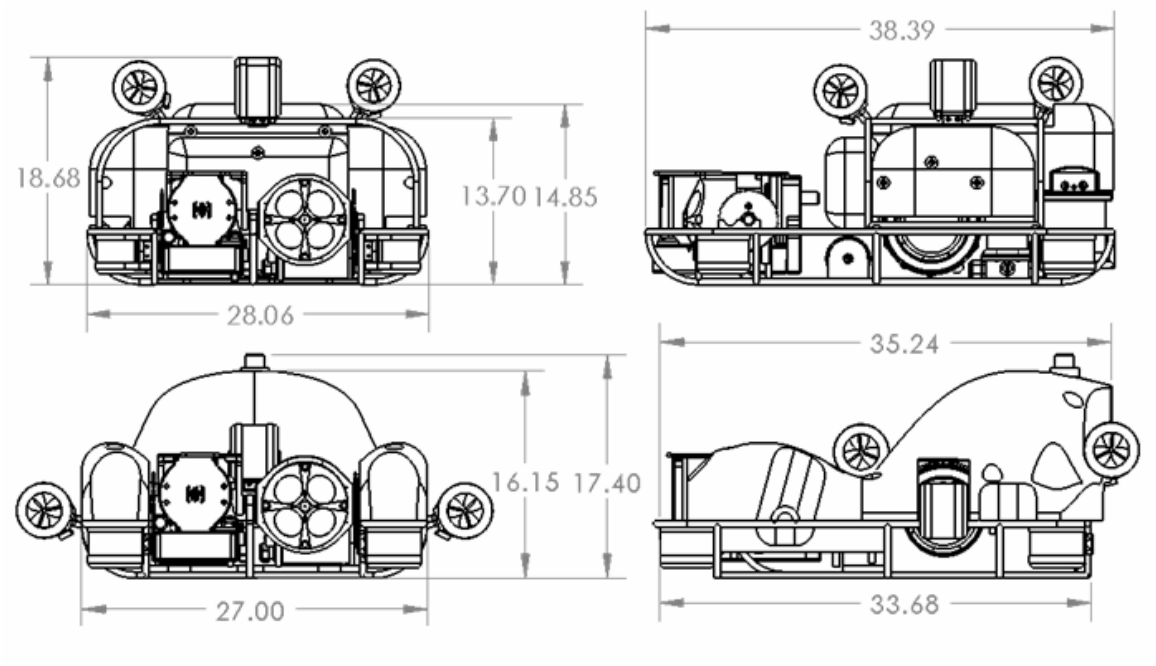

Figure 2-4: Comparison of the external dimensions of the HAUV and the HAUV1B. All dimensions are given in inches.

June 2007. Having a second vehicle during these demonstrations and afterwards will be beneficial as it will allow Bluefin to concentrate on vehicle operations and MIT to focus on developing improved navigation algorithms. While it is still too early to fully quantify the effectiveness of the new HAUV1B design, this should be monitored over the next several months and the resulting information used to improve future HAUV designs.

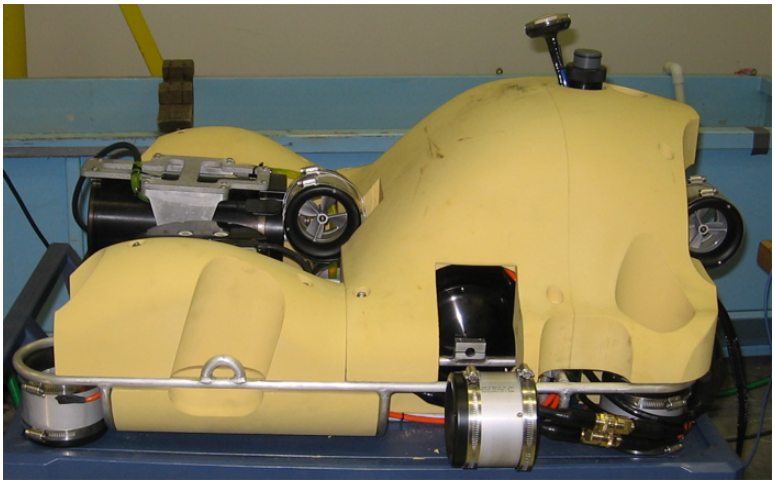

Figure 2-5: The HAUV1B during initial assembly. Photograph courtesy of Bluefin Robotics.

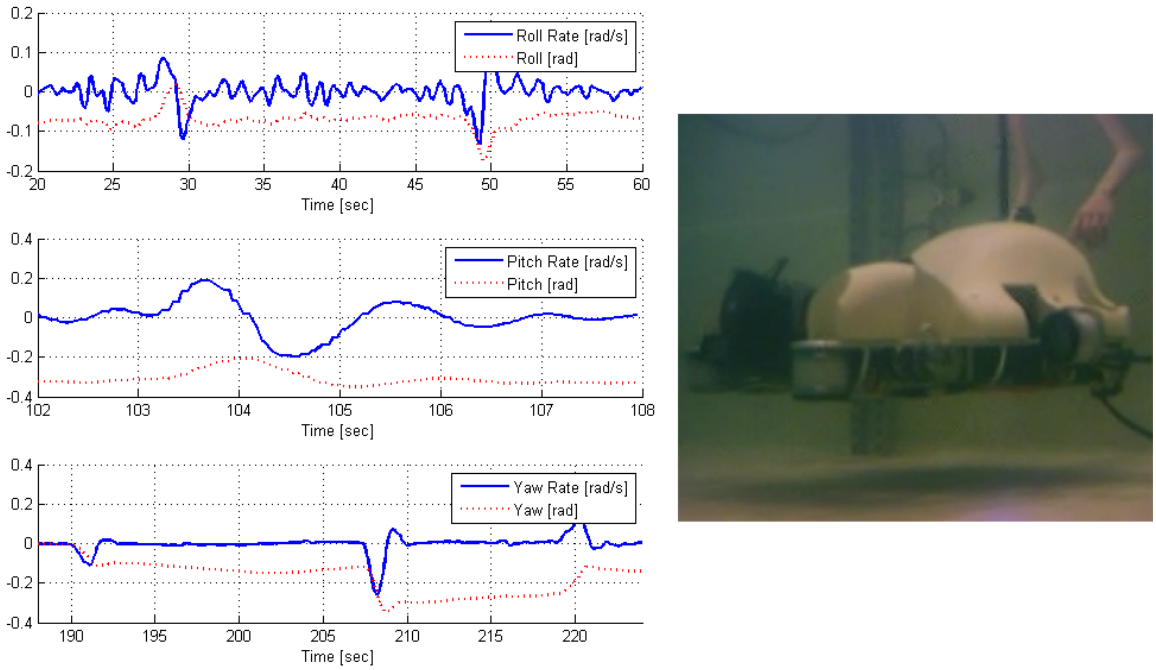

Figure 2-6: Roll, pitch, and yaw data collected during initial low-level servo tuning. Each angular degree of freedom was disturbed independently to observe the response characteristics. Roll is driven to zero with both proportional and derivative gains while both pitch and yaw use only derivative terms.

Chapter 3

DVL Navigation Algorithms

Many autonomous vehicles rely on navigation data obtained from absolute position and orientation sensors including GPS units and compasses; however, it is often necessary to operate vehicles in environments that preclude the use of such sensors. The present application, for example, involves inspecting ship hulls with an AUV in harbor environments where neither GPS nor compass readings are available. Currently, the HAUV's odometry is generated by means of a four-beam Teledyne RDI Doppler Velocity Log (DVL) sensor which tracks relative motion between the AUV and its target hull (see Section 1.2.3). Integrating this DVL velocity yields a hull-relative position which is initially fairly accurate but is prone to significant drift over time.

Various other sensor-based navigation strategies have been developed for autonomous agents and have potential applicability to the ship hull inspection task. One approach is to deploy a calibrated network of transponders to generate localization information [19]. A Sonic High Accuracy Ranging and Positioning System (SHARPS) package has been purchased from Marine Sonic Technology, Ltd. for obtaining decent ground-truth data in testing and could eventually be utilized in closed-loop vehicle control. An alternative approach is to use acoustic or optical images to estimate the 3D structure of the ship hull and concurrently estimate the agent's pose as in [3, 5, 15]. Current work by Leonard, Walter, et. al. seeks to implement such a Simultaneous Localization and Mapping (SLAM) framework as in [3, 4] with images captured by the DIDSON and possibly a digital video camera (in

non-turbid environments). SLAM is an appealing choice for this problem because a typical horizontal or vertical survey mission might include many 'loop closures' or local target re-visitations which lend themselves to recursive navigation updates.

While appealing, full SLAM may not be necessary for all ship hull inspection tasks. Since in this case we are mostly concerned with the localization aspect of AUV navigation, a SLAM-constructed map of somewhat arbitrary features on the target hull would be considered a side product of estimating the agent's state rather than a primary result of the inspection. Furthermore, since we often have access to a prior map of the target ship hull in the form of ship's lines or a full CAD model, simple sensors (such as acoustic range-finders) can be used to perform accurate localization in the large, non-complex areas of a ship hull. This chapter develops methods for applying few range measurements taken at known angles relative to the agent's heading to estimating its current position. Several observation geometries are considered, and a method for utilizing models based on multiple curves is proposed.

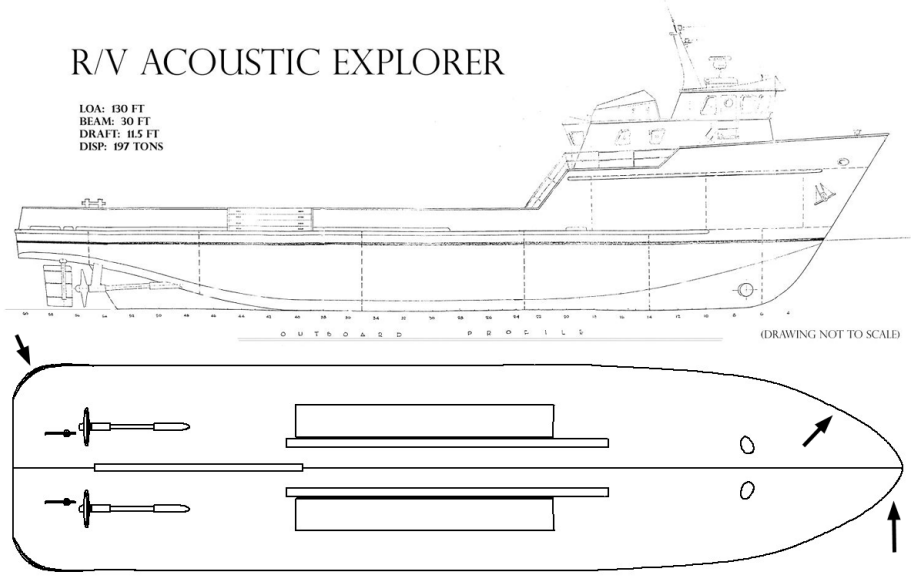

Figure 3-1: Lines of the R/V *Acoustic Explorer* with arrows indicating the sections in which curvature-based navigation would be possible. Note that these are two separate drawings (top and bottom) which are not to scale. Images provided by the Office of Naval Research.

3.1 Applications and Assumptions

The basic principle behind range-based navigation is that the two-dimensional point of origin of a set of n rays can be analytically calculated by observing the points of intersection between these rays and a surface of known curvature. For example, Section 3.3 shows that a vehicle position estimate can be generated from two range measurements to a parabolic wall when the agent's world-relative heading is known. While the shape of most real ship hulls or other inspection targets cannot be accurately modeled by a single simple parabola, the estimation algorithm can be expanded to navigate relative to a surface composed of multiple quadratic functions spliced together at known points (see Section 3.5). The lines of the R/V *Acoustic Explorer* shown in Figure 3-1, for example, have distinct sections of high curvature which could be modeled as series of known functions for use in range-based navigation. Figure 3-2 outlines an intuitive procedure for integrating prior knowledge of curved, submerged objects into the estimation scheme.

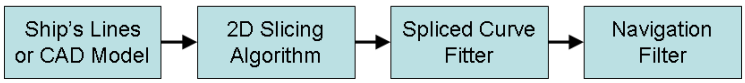

Figure 3-2: A system-level view of processing *a priori* hull geometry information for use in AUV position estimation. Prior models and drawings can be converted into two-dimensional ship's lines (as in the lower portion of Figure 3-1) which can then be decomposed into a series of spliced functions. Section 3.5 explains how an AUV can navigate relative to these curves using simple range measurements.

Admittedly, not all ship hulls have sufficient curvature to permit this type of localization with acceptable accuracy. Range-based navigation is still applicable in these situations, however, because range measurements can also be used to detect sharp features like sea chests, cooling fins, and hard corners on the hull. Section 3.6 presents experimental DVL range data which show how a small collection of features can be easily identified. Presuming the locations of these features are known *a priori*, agent localization and thus navigation updates are possible. Even when such sharp features are not mapped precisely prior to inspection, their locations can be tracked

through a simple SLAM system which also provides for agent navigation updates.

The algorithms developed in this chapter assume that accurate range measurements (subject to small, well-modeled Gaussian noise) are available at known vehicle-relative headings. These assumptions hold reasonably well for high frequency, narrow beam sonar systems where wavefronts are likely to return from nearly the desired point on a target by means of specular reflection. The target-point precision decreases with increasing beam width, though, and scattering becomes more prevalent at lower beam frequencies (when the wavelength approaches the order of the target curvature) [16, 10]. The DVL mounted on the HAUV has a beamwidth[1] of 1.3° (at 1200kHz) to 3.9° (at 300kHz). Data presented in Figure 3-13 suggests that the DVL is capable of detecting target surfaces at fairly high angles of incidence when operated at 1200kHz.

We consider range measurements to both flat and concave target surfaces in the following sections. While there is no theoretical algorithmic difference between taking range measurements to a concave or a convex surface, the physics of sonar reflection again introduce sensor-specific observation differences between these cases. Especially of interest are the issues of cross-talk between sonar range-finders and the accuracy of returns originating from regions of high curvature. Additionally, the algorithms presented in this chapter do not account for acoustic properties of the target which could affect range measurement accuracy in certain situations.

While both navigation relative to deployed sensor networks (LBL, SBL, USBL, SHARPS, etc.) and SLAM can be more robust than range-based navigation for certain sensor and curvature combinations, this strategy has the advantages of requiring no external transducer network or image processing, and involving only limited (if any) feature detection capabilities. Furthermore, the range-based navigation algorithms are scalable to incorporate different numbers of range measurements. For example, the parabolic curvature algorithm needs at least two range measurements, but it can accept data from scanning range-finders which yield tens to hundreds of

[1]Specifications as reported in the *Navigator ADCP/DVL User's Guide* which can be found online from several sources including: http://4dgeo.whoi.edu/panama-doc/Instruments/Manuals/Nav_Users_Guide.pdf

ranges at known angles. The equations presented in Section 3.3.4 show clearly how data from many sensors can be combined in a Kalman filter framework to improve the overall agent position estimate.

3.2 Navigation Relative to Flat Surfaces

One of the simplest cases of range-based navigation uses a pair of sonar beams to regulate vehicle heading and normal separation relative to a flat surface. Figure 3-3 illustrates the geometry of this situation. Notice that θ_v represents vehicle heading

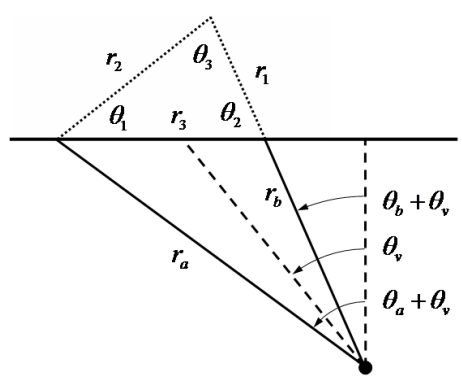

Figure 3-3: Geometry for range-based navigation when observing a flat surface.

while the angles $\{\theta_a, \theta_b\}$ represent the positioning of range sensors relative to the vehicle's forward direction. These angles, in addition to the sensor range returns $\{r_a, r_b\}$, can be combined to define the rest of the quantities labeled in Figure 3-3:

$$\theta_1 = \frac{1}{2}(\theta_a + \theta_b) + \theta_v \tag{3.1}$$

$$\theta_2 = \frac{\pi}{2} - (\theta_b + \theta_v) \tag{3.2}$$

$$\theta_3 = \frac{1}{2}(\pi + \theta_b - \theta_a) \tag{3.3}$$

$$r_1 = r_a - r_b \tag{3.4}$$

$$r_2 = \sqrt{2r_a^2(1 - \cos(\theta_a - \theta_b))} \tag{3.5}$$

$$r_3 = \sqrt{r_1^2 + r_2^2 - 2r_1 r_2 \cos(\theta_3)} \tag{3.6}$$

Given these definitions, the law of sines is applied to the upper triangle in Figure 3-3 through (3.7) to determine the vehicle's relative heading. A control loop can be built around this synthetic yaw measurement to regulate vehicle heading to a desired value. Additionally, given the agent's yaw angle as in (3.7), it is trivial to calculate its normal distance from the flat target surface. One possible computation of that quantity which may also be regulated in a separate control loop is given by (3.8).

$$\theta_v = \arcsin\left(\frac{r_1}{r_3}\sin(\theta_3)\right) - \frac{1}{2}(\theta_a + \theta_v) \tag{3.7}$$

$$d_\perp = \frac{1}{2}\left[r_a\cos(\theta_a + \theta_v) + r_b\cos(\theta_b + \theta_v)\right] \tag{3.8}$$

Equations (3.7) and (3.8) give the two vehicle parameters (yaw and planar y position) that can be extracted from range measurements to a flat wall and regulated by a mobile agent assuming complete control authority over the problem's three degrees of freedom. Notice that a flat target is not rich enough to allow for estimation of agent position parallel to the surface. When operating in this type of environment, along-target position must be estimated by another means, such as integrating the relevant relative velocity provided by a sensor similar to the DVL. Many situations are encountered in ship hull inspection, however, where the target for range-based navigation is not flat, but rather, has ample curvature for use in estimating the along-target position. The remaining sections in this chapter deal with exploiting such curvature and other features of interest for more accurate agent localization.

3.3 Navigation Relative to Parabolic Surfaces

3.3.1 Overview of Algorithm

Although range-only observations taken from a mobile agent to a flat surface can resolve only two of the three vehicle degrees of freedom, complete planar vehicle position can be determined once the target surface is given curvature. This section develops an algorithm which generates a vehicle position estimate $\{x_v, y_v\}$ based on

two range measurements $\{r_a, r_b\}$ taken at agent-relative bearings $\{\theta_a, \theta_b\}$ to a known parabolic target. An explicit analytic relationship exists between these quantities (see Section 3.3.3) which not only enables position estimates, but also an error mapping between the range measurements and the estimated quantities. With this information, geometric position estimates can be used as measurements in an Extended Kalman Filter (EKF) which produces an optimal estimate of the agent's planar location. It is also shown that when excessive range data are available, position estimates can be developed for each combination of two range measurements and all $\{x_v, y_v\}$ pairs can be incorporated into the same EKF.

Similar work has been done by Madhavan and Durrant-Whyte [9] in which they navigate based on points of maximum curvature extracted from observed surfaces. Several other authors including Sekmen [12] have considered the problem of identifying the location and curvature of cylindrical targets from a mobile agent. Kondo and Ura also use curvature in [7] and [8] to track features with their AUV remaining at a desired relative heading. The present approach differs from these in that we produce actual vehicle position estimates by exploiting the known geometric properties of an observed surface.

A simple dynamic model of the HAUV is first developed in Section 3.3.2 for use in simulation and also with an Extended Kalman Filter. The parabolic observation model is derived in Section 3.3.3 and noise properties of this localization approach are also presented. Section 3.3.5 shows the results of a simulated vehicle controlled based on the output of an Extended Kalman Filter.

3.3.2 Vehicle Dynamic Model

A state-space model of a simplified HAUV-like system can be developed for use in simulation. The vehicle states are taken to include vehicle-relative velocities (two planar and one rotational) as well as global Cartesian locations and vehicle yaw. That is:

$$\mathbf{x}(t) = \begin{bmatrix} u & v & \dot{\theta}_v & x_v & y_v & \theta_v \end{bmatrix}^T \tag{3.9}$$

The simplified HAUV model is actuated by means of four thrusters placed along its exterior perimeter as shown in Figure 3-4. The corresponding system input vector is thus given by:

$$\mathbf{u_t}(t) = \begin{bmatrix} F_A & F_B & F_C & F_D \end{bmatrix}^T \tag{3.10}$$

The generalized vehicle inputs $\mathbf{u_v}(t)$ are related to the individual thruster forces $\mathbf{u_t}(t)$ by means of a thruster mapping matrix $\mathbf{M}$:

$$\mathbf{u_v}(t) = \mathbf{M}\mathbf{u_t}(t) \tag{3.11}$$

$$\begin{bmatrix} X \\ Y \\ M \end{bmatrix} = \begin{bmatrix} -1 & 0 & 1 & 0 \\ 0 & 1 & 0 & -1 \\ r_v & r_v & r_v & r_v \end{bmatrix} \begin{bmatrix} F_A \\ F_B \\ F_C \\ F_D \end{bmatrix}$$

At low velocities, when the effects of hydrodynamic drag on the system are negligible, the system dynamics propagate as:

$$\dot{\mathbf{x}}(t) = \mathbf{f}(\mathbf{x}(t), \mathbf{u_v}(t), t) + \mathbf{w}(t) \tag{3.12}$$

$$\mathbf{z_k} = \mathbf{h}(\mathbf{x}(t_k)) + \mathbf{v_k} \tag{3.13}$$

In this representation, $\mathbf{x}(t)$ are the vehicle states, $\mathbf{u_v}(t)$ are the control inputs, $\mathbf{z_k}$ are the measurements, and $\mathbf{w}(t)$ and $\mathbf{v_k}$ add Gaussian noise with respective variances of $\mathbf{Q}$ and $\mathbf{R}$. Notice that the vehicle state vector propagates continuously while the measurements are made in discrete time. The nonlinear state propagation function $\mathbf{f}(\mathbf{x}(t), \mathbf{u_v}(t), t)$ can be defined as:

$$\mathbf{f}(\mathbf{x}(t), \mathbf{u_v}(t), t) = \begin{bmatrix} X/m & Y/m & M/J & c_1 & c_2 & \dot{\theta}_v \end{bmatrix}^T \tag{3.14}$$

where:

$$c_1 = u\cos\theta_v - v\sin\theta_v$$
$$c_2 = u\sin\theta_v + v\cos\theta_v$$

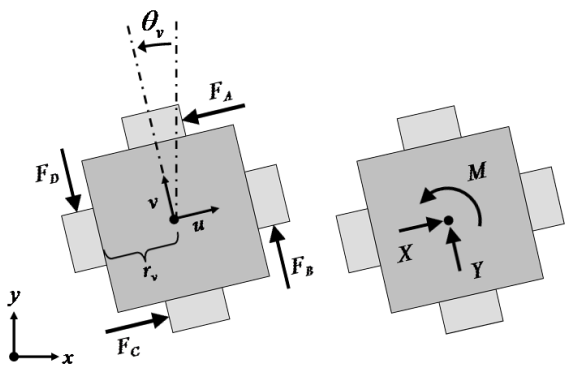

Figure 3-4: Free-body diagram of the simplified HAUV dynamic model indicating chosen thrust and yaw conventions.

Vehicle mass m and inertia J properties were chosen considering a neutrally buoyant rectangular prism of dimensions 1.0m x 1.0m x 0.5m which represents a more symmetrical version of the HAUV. The simulated mass is 512.5kg and the simulated inertia is 85.4kg·m^2; these parameters were chosen for neutral buoyancy. The variables X, Y, and M in (3.14) are the horizontal, vertical, and rotational control signals as defined in (3.11) and Figure 3-4.

A simple PD control scheme was developed to drive the estimated state $\hat{\mathbf{x}}(t)$ to a reference state $\mathbf{x_r}(t)$ by means of an error vector $\tilde{\mathbf{x}}(t) = \mathbf{x_r}(t) - \hat{\mathbf{x}}(t)$. The controller was developed with dynamics linearized about the hovering condition which provides a means for selecting an adequate compensator of the form $\mathbf{u_v}(t) = -\mathbf{K_c}\tilde{\mathbf{x}}(t)$. This vector of desired control efforts $\mathbf{u_v}(t)$ can be related to the desired thruster forces $\mathbf{u_t}(t)$ by means of the Moore-Penrose pseudoinverse of the thruster mapping matrix $\mathbf{M}^+$ from (3.11):

$$\mathbf{u_t}(t) = \mathbf{M}^+\mathbf{u_v}(t) \tag{3.15}$$

The proportional and derivative control gains were chosen to place the compensated system poles such that the θ_v step response settles in roughly 0.5 seconds while the x_v and y_v responses settle about four times slower (each with minimal overshoot). These selections are consistent with the dynamic performance of the actual vehicle in

operation.

$$\mathbf{K_c} = \begin{bmatrix} 1610 & 0 & 0 & 1412 & 0 & 0 \\ 0 & 1610 & 0 & 0 & 1412 & 0 \\ 0 & 0 & 1073 & 0 & 0 & 4941 \end{bmatrix} \tag{3.16}$$

Figure 3-5 shows step responses of the three position states using the controller defined by the gains in (3.16). Notice that the x_v and y_v responses are not identical due to the nonzero heading command. As θ_v increases, this difference in responses becomes more pronounced.

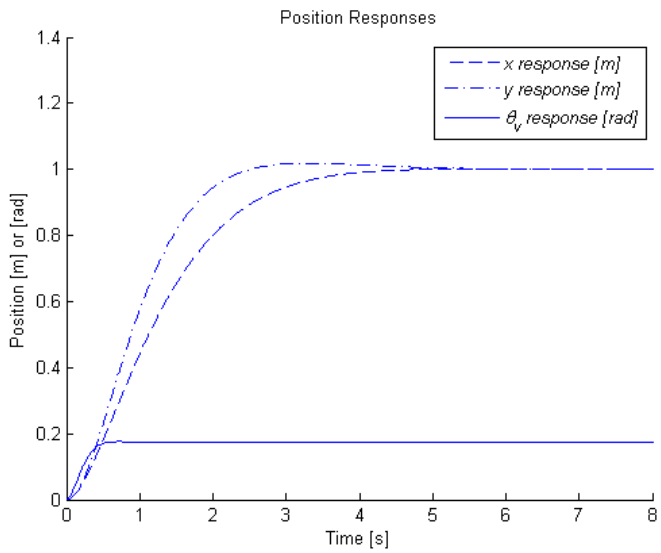

Figure 3-5: Step response of x_v, y_v, and θ_v states.

3.3.3 Parabolic Observation Model

In addition to velocity data, the DVL returns a range measurement for each beam. We can pitch the sensor down 22° to emulate a pair of range-finding beams which lie in-plane with the vehicle and are separated by 41.4°. Similarly, we model the sensor as a set of observations taken at fixed bearings relative to the vehicle's longitudinal axis but do not limit the modeled sensor to two beams. We assume that an accurate yaw position θ_v is available at least in the short term from an inertial measurement

unit[2], and that range measurements are taken against a pocket of known parabolic ($y = A_w x^2 + B_w$) curvature. With these assumptions in addition to those explained in Section 3.1, two range measurements $\{r_a, r_b\}$ taken at bearings $\{\theta_a, \theta_b\}$ are sufficient to produce an estimate of vehicle planar position $\{x_v, y_v\}$. Note that although A_w must be negative to model a pocket at zero vehicle yaw, there is no algorithmic difference between estimating vehicle pose by observing either a parabolic pocket or a parabolic protrusion.

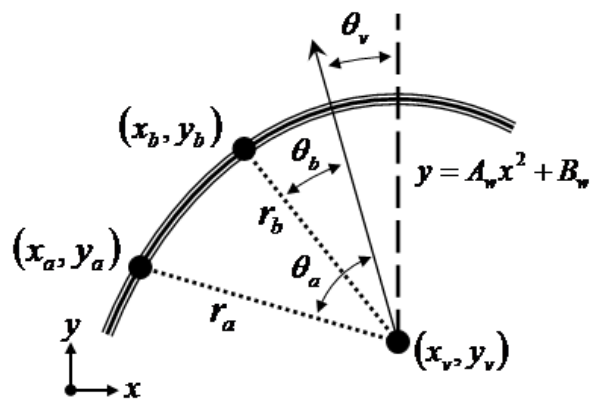

Figure 3-6: Observation geometry modeled to simulate range data received from the DVL sensor on the HAUV. For the DVL case, $\theta_a = +20.7°$ and $\theta_b = -20.7°$.

$$x_v = \frac{r_a c_a / A_w - r_b c_b / A_w - r_a^2 s_a^2 + r_b^2 s_b^2}{-2 r_a s_a + 2 r_b s_b} \tag{3.17}$$

$$y_v = \frac{1}{2}\left\{A_w\left[(x_v - r_a s_a)^2 + (x_v - r_b s_b)^2\right] + 2B_w - r_a c_a - r_b c_b\right\} \tag{3.18}$$

where:

$$s_a = \sin(\theta_v + \theta_a) \quad s_b = \sin(\theta_v + \theta_b)$$
$$c_a = \cos(\theta_v + \theta_a) \quad c_b = \cos(\theta_v + \theta_b)$$

While only two range measurements are needed to develop a position estimate, it is clear that this procedure can be applied to the general case of an n-beam scenario where $n \geq 2$. When redundant range information ($n > 2$) is available, $m = \frac{n!}{2(n-2)!}$

[2]If only rate gyros are available, vehicle yaw position must be calibrated with respect to a known feature prior to generating position estimates.

distinct estimates of vehicle position can be developed and combined by simple averaging. In this case, the observation vector at timestep k becomes:

$$\mathbf{z_k} = \begin{bmatrix} x_{v1} & y_{v1} & \cdots & x_{vm} & y_{vm} & \theta_v \end{bmatrix}^T \tag{3.19}$$

The multi-beam sensor scenario is, in fact, a simplified version of scanning sonar observation. The algorithms presented here can be directly applied to the scanning case, allowing direct vehicle position estimates to be developed when these more advanced sensors are employed in environments of known curvature (further details in Section 3.3.4). It is also worth noting that this localization technique is applicable to environments where features are not accurately described by a single parabolic curve. The estimation equations have been developed for sinusoidal pockets for example (see Section 3.4), and the same procedure can be applied to other types of curvature. Additionally, multiple curves can be combined in a piecewise manner to facilitate vehicle navigation along complex targets like ship hulls (see Section 3.5). In some cases the correct estimate my need to be selected from a set of candidate positions based on recent navigation history.

In addition to the geometric constraints derived in (3.17) and (3.18), it is also important to understand the noise properties of the resulting position estimate. By calculating the partial derivatives of these equations with respect to each range measurement we observe how sensor noise translates into (x_v, y_v) estimate uncertainty. Figures 3-7 and 3-8 show graphical representations of these derivatives which indicate how the vehicle estimate noise properties vary with respect to sensor noise at each location within the space below a curved target. Notice that for chosen surface and sensor geometries the noise on x_v depends strongly upon the distance from the wall while the noise gradient on y_v is much more gentle throughout. Also, notice that the noise on x_v becomes substantially higher when the surface flattens. In Figure 3-8, for example, the vehicle would have to move roughly 26m away from the wall to achieve $\partial x_v/\partial r_a$ and $\partial x_v/\partial r_b$ values as low as ± 5 which occur at a range of only 2m in Figure 3-7. This error analysis supports the intuitive conclusion that targets with higher

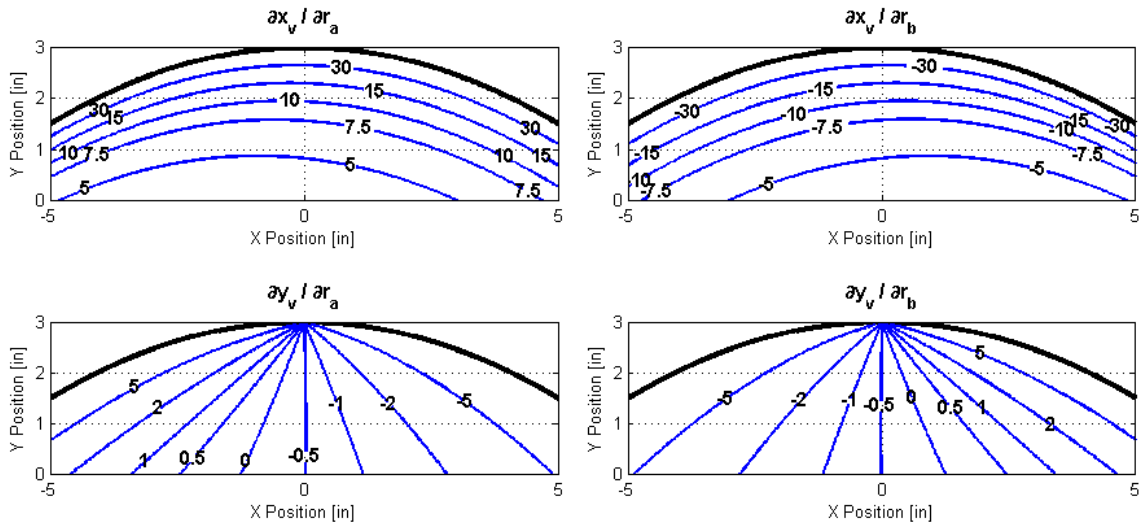

Figure 3-7: Partial derivatives of estimated vehicle position shown for an agent with no yaw and a DVL-like sensor configuration (two symmetric range-finder beams separated by 41.4°) observing a surface conforming to the equation $y = -0.06x^2 + 3$. These non-dimensional derivatives are effectively gains which map sensor noise to error in the x_v and y_v position estimates.

curvature yield more accurate position estimates.

3.3.4 Nonlinear Estimator

An Extended Kalman Filter can be employed to combine estimates developed based on observations of a curved target surface. At each timestep, the filtering process begins by calculating the Jacobian of the nonlinear state propagation function $\mathbf{F}(\mathbf{x}(t), t)$ as well as the Jacobian of the observation model $\mathbf{H_k}$ using (3.20) and (3.21), respectively. Notice that the first two rows of the observation Jacobian are repeated m times, where m reflects the number of range-pair-based estimates included in the

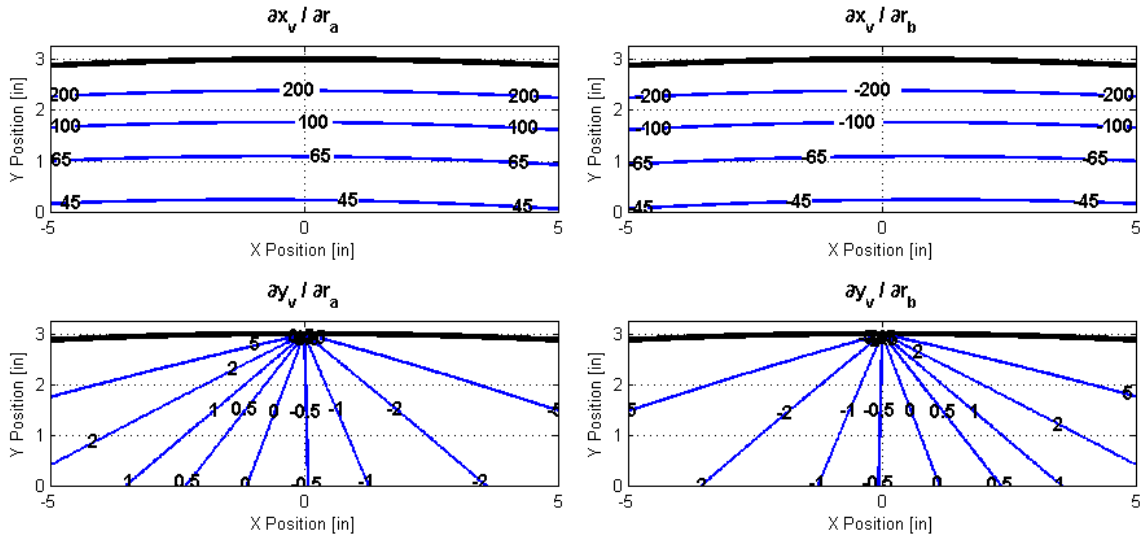

Figure 3-8: Partial derivatives as in Figure 3-7 with an observed surface equation $y = -0.005x^2 + 3$.

observation $\mathbf{z_k}$ (which itself has $2m + 1$ rows as seen in (3.19)).

$$\mathbf{F}(\mathbf{x}(t), t) = \begin{bmatrix} 0 & 0 & 0 & 0 & 0 & 0 \\ 0 & 0 & 0 & 0 & 0 & 0 \\ 0 & 0 & 0 & 0 & 0 & 0 \\ \cos\theta_v & -\sin\theta_v & 0 & 0 & 0 & c_3 \\ \sin\theta_v & \cos\theta_v & 0 & 0 & 0 & c_4 \\ 0 & 0 & 1 & 0 & 0 & 0 \end{bmatrix} \tag{3.20}$$

where:

$$c_3 = -u\dot{\theta}_v \sin\theta_v - v\dot{\theta}_v \cos\theta_v$$

$$c_4 = u\dot{\theta}_v \cos\theta_v - v\dot{\theta}_v \sin\theta_v$$

$$\mathbf{H_k} = \begin{bmatrix} 0 & 0 & 0 & 1 & 0 & 0 \\ 0 & 0 & 0 & 0 & 1 & 0 \\ 0 & 0 & 0 & 1 & 0 & 0 \\ 0 & 0 & 0 & 0 & 1 & 0 \\ \vdots & \vdots & \vdots & \vdots & \vdots & \vdots \\ 0 & 0 & 0 & 0 & 0 & 1 \end{bmatrix} \tag{3.21}$$

With the Jacobians calculated, *a priori* state $\hat{\mathbf{x}}_\mathbf{k}^-$ and error covariance $\mathbf{P_k}^-$ estimates can be generated by means of the standard continuous-discrete EKF formulation found in [6] and shown below in (3.22). When new curvature-based position estimates are available in $\mathbf{z_k}$, a Kalman gain can be calculated and the *a priori* estimates updated with (3.23) and (3.24).

Prediction Step[3]

$$\begin{aligned} \dot{\hat{\mathbf{x}}}(t) &= f(\hat{\mathbf{x}}(t), \mathbf{u_v}(t), t) \\ \dot{\mathbf{P}}(t) &= \mathbf{F}(\hat{\mathbf{x}}(t), t)\mathbf{P}(t) + \mathbf{P}(t)\mathbf{F}^T(\hat{\mathbf{x}}(t), t) + \mathbf{Q}(t) \end{aligned} \tag{3.22}$$

Gain Calculation[3]

$$\mathbf{K_k} = \mathbf{P_k}^-\mathbf{H_k}^T(\hat{\mathbf{x}}_\mathbf{k}^-)\left[\mathbf{H_k}(\hat{\mathbf{x}}_\mathbf{k}^-)\mathbf{P_k}^-\mathbf{H_k}^T(\hat{\mathbf{x}}_\mathbf{k}^-) + \mathbf{R_k}\right]^{-1} \tag{3.23}$$

Correction Step[3]

$$\begin{aligned} \hat{\mathbf{x}}_\mathbf{k}^+ &= \hat{\mathbf{x}}_\mathbf{k}^- + \mathbf{K_k}\left[\mathbf{z_k} - \mathbf{h_k}(\hat{\mathbf{x}}_\mathbf{k}^-)\right] \\ \mathbf{P_k}^+ &= \left[\mathbf{I} - \mathbf{K_k}\mathbf{H_k}(\hat{\mathbf{x}}_\mathbf{k}^-)\right]\mathbf{P_k}^- \end{aligned} \tag{3.24}$$

The predicted observation vector $\mathbf{h_k}(\hat{\mathbf{x}}_\mathbf{k}^-)$ used in estimate correction is constructed based on m range-pair-based estimates, resulting in a $2m+1$ element column vector which must be recomputed at each timestep. Similarly, the observation noise covari-

[3]The continuous-discrete EKF equations shown here are derived by Gelb in §6.1 of [6]

ance R is dependent upon vehicle position and must also be calculated continuously.

$$\mathbf{h_k}(\hat{\mathbf{x}}_\mathbf{k}^-) = \begin{bmatrix} \hat{x}_v & \hat{y}_v & \cdots & \hat{x}_v & \hat{y}_v & \hat{\theta}_v \end{bmatrix}^T \tag{3.25}$$

$$\mathbf{R_k} = \begin{bmatrix} R'_{1,1} & \cdots & R'_{1,2m} & 0 \\ \vdots & \ddots & \vdots & \vdots \\ R'_{2m,1} & \cdots & R'_{2m,2m} & 0 \\ 0 & \cdots & 0 & \sigma^2_{\theta_v} \end{bmatrix} \tag{3.26}$$

where:

$$R'_{i,j} = \frac{\partial z_i}{\partial r_a}\frac{\partial z_j}{\partial r_a}\sigma^2_{r_a} + \frac{\partial z_i}{\partial r_b}\frac{\partial z_j}{\partial r_b}\sigma^2_{r_b}$$

In summary, the curvature-based estimation algorithm follows a simple procedure at each timestep (k) where new range data is available:

1. Perform the EKF prediction step propagating the state and covariance estimates using (3.22).

2. Capture a set of n range measurements taken between the mobile agent and a surface of known curvature.

3. Calculate a set of m agent position estimates $\{x_{vi}, y_{vi}\}$ using (3.17) and (3.18) where each estimate is based on a unique pair of range measurements. This set of positions becomes the actual observation vector $\mathbf{z}_k$ as defined in (3.19).

4. Construct a predicted observation vector $\mathbf{h_k}(\hat{\mathbf{x}}_\mathbf{k}^-)$ as in (3.25) using the estimated state from (3.22), and a covariance matrix $\mathbf{R_k}$.

5. Calculate Jacobians with (3.20) and (3.21) and perform the EKF correction step using (3.23) and (3.24) to generate new state and error covariance estimates.

3.3.5 Dynamic Simulation Results

The performance of the simplified dynamic system developed in Section 3.3.2 with curvature-based observations provided to an EKF has been simulated for a variety

of target and beam configurations. Sensor readings were taken in these simulations discretely at 10Hz as is typical for a DVL, and both the actual vehicle state and the EKF were propagated continuously via the Runge-Kutta method between timesteps. Range sensor noise standard deviations of 2cm were assumed (again to emulate the DVL), as were a nominal yaw sensor deviation of 0.005rad, u and v deviations of 10cm/s, and a $\dot{\theta}_v$ deviation of 0.1rad/s.

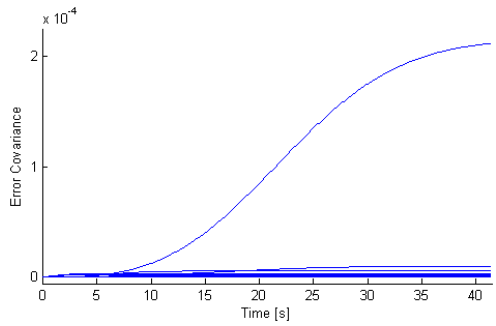

Figure 3-9: Evolution of the elements of the error covariance $\mathbf{P}$ matrix with $(\hat{x}_v, \hat{y}_v)$ starting at $(0, 0)$ and moving to $(1, 1)$.

Figure 3-9 demonstrates the evolution of elements in the error covariance $\mathbf{P}$ matrix over time and indicates, as expected, that the noisy $\hat{x}_v$ and $\hat{y}_v$ estimates take longer to stabilize. Each of the other estimates respond fairly quickly, and care must be taken as the filter bandwidth approaches that of the controller. Figure 3-10 shows the results of a typical dynamic simulation. Notice that the error magnitude in $\hat{x}_v$ is larger than the error in $\hat{y}_v$ due to the increased sensitivity predicted in Figures 3-7 and 3-8. Since position estimate noise rapidly increases close to the observed surface, better results can be obtained by operating farther from the wall.

3.4 Observing Sinusoidal Surfaces

Section 3.3.3 details the procedure for generating an agent position based on range measurements to a known parabolic surface; however, it should be noted that (3.17) and (3.18) can be reformulated for observations made within or external to a single pocket (i.e., half period) of a sinusoidal surface (see Figure 3-11). The prediction

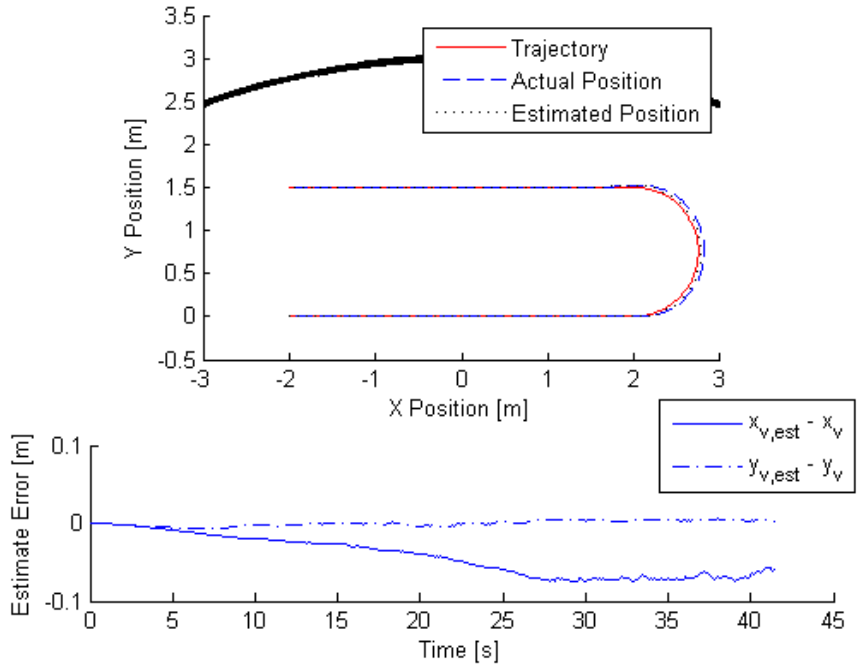

Figure 3-10: Results of a typical simulation with no vehicle yaw, two sensor beams spaced 41.4° apart, and range error deviations of $1mm$. The vehicle followed the 'U'-shaped path from the lower-left at approximately $0.25m/s$.

described in this section assumes a surface represented as:

$$y = A_w \sin(K_w x) \tag{3.27}$$

Given the target parameters A_w and K_w, geometric relations (3.28) and (3.29) can be applied to generate agent position predictions. These predictions can be used in an EKF framework as in Section 3.3.4 providing the noise properties $\{ \frac{\partial x_v}{\partial r_a}, \frac{\partial x_v}{\partial r_b}, \frac{\partial y_v}{\partial r_a}, \frac{\partial y_v}{\partial r_b} \}$ are calculated appropriately and used in the $\mathbf{R_k}$ matrix.

$$x_v = \frac{1}{2}\left[\frac{2}{K_w}c_1 - (r_b - r_a)\sin\theta_d\right] \tag{3.28}$$

$$y_v = A_w \sin\left(\frac{K_w}{2}\left[\frac{2}{K_w}c_1 - (r_a + r_b)\sin\theta_d\right]\right) \tag{3.29}$$

where:

$$c_1 = \arccos\left(\frac{1}{2A_w}\frac{(r_b - r_a)\cos\theta_d}{\sin\left(\frac{K_w}{2}(r_a + r_b)\sin\theta_d\right)}\right)$$

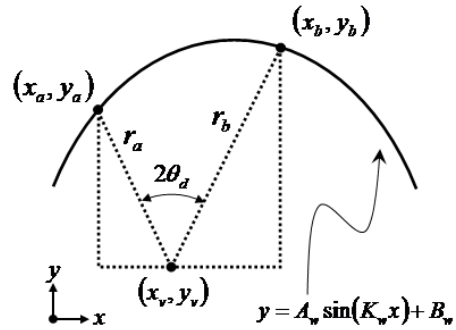

Figure 3-11: Geometry for observing a sinusoidal target surface. Note that $2\theta_d = 41.4°$ for the DVL.

3.5 Spliced Curve Navigation

Sections 3.3 and 3.4 show that range-based navigation is feasible for a vehicle taking measurements to parabolic and sinusoidal surfaces; however, these results are not immediately applicable to the ship hull inspection problem. In practice, we need to navigate relative to a complex curve, but this complexity can be broken-down by representing such surfaces as a combination of simple curves as illustrated in Figure 3-12. For hull inspection, this could mean representing a two-dimensional slice of a ship hull as a series of connected parabolic segments.

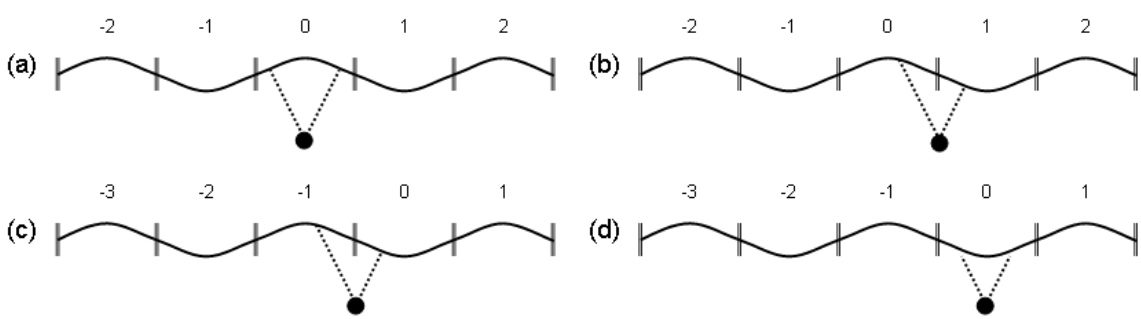

Figure 3-12: Procedure for navigating relative to a series of spliced curves. The agent begins with both beams observing a curve with index 0. Once one beam crosses onto a new parabola, all indices are updated to reflect this new 'home curve.'

In order to join two parabolic segments we require that their respective functions share a single value and a single derivative at the point of intersection; that is, the composite curve and its slope must both be represented by smooth functions.

The following formulation will be employed to describe parabolic curves using three parameters:

$$y = A\left(x - C\right)^2 + B \tag{3.30}$$

Note that this representation is more general than the one used in (3.17) and (3.18) because it allows for the entire parabola to be shifted in the x direction by C. This extra degree of freedom is necessary when splicing curves as each segment will have a local origin which will likely not coincide with the global origin. As expected, this expanded parameterization slightly changes the equations for calculating agent position from range data; thus, revised formulas are presented in this section. As a final comment on notation, when joining curves y_1 and y_2 at an intersection point (x_c, y_c), we choose logical parameter sets $\{A_1, B_1, C_1\}$ and $\{A_2, B_2, C_2\}$.

3.5.1 Vehicle Position Calculations

We now consider a two-beam sensor taking range measurements to a composite curve constructed of many spliced parabolas. Given knowledge that the agent is in the vicinity of one of these curves (the 'home curve') we find that there are three possible observation scenarios:

1. **Both beams intersect the 'home curve'.** In this case, a vehicle position estimate (x_v, y_v) can be developed from the single target curve as in (3.31) and (3.32). This calculation is similar to the one presented in Section 3.3.3 and it yields a single solution.

2. **One beam intersects the 'home curve' and one intersects the curve to its left.** When the sensor 'straddles' a splice point, each curve must be considered in the agent position calculation. Equations (3.33) and (3.34) provide this functionality. Note that two possible solutions exist in this case.

3. **One beam intersects the 'home curve' and one intersects the curve to its right.** Again, equations (3.33) and (3.34) can be used to determine two possible agent locations.

We assume throughout that the two sensor beams will always either intersect a single curve or two adjacent spliced curves. The algorithms presented here do not necessarily hold for cases in which additional curves segments are present between those which intersect sensor beams. This is an important point to consider when decomposing a complex curve into a chain of parabolic segments as too high a resolution will lead to poor (or inexistent) navigation data.

Single Curve Position Calculation

$$x_v = \left(\tfrac{r_a c_a}{A} - \tfrac{r_b c_b}{A} - 2Cr_a s_a + 2Cr_b s_b - r_a^2 s_a^2 + r_b^2 s_b^2\right) / \left(-2r_a s_a + 2r_b s_b\right) \quad (3.31)$$

$$y_v = \tfrac{1}{2}\left(A\left[(x_v - Cr_a s_a)^2 + (x_v - Cr_b s_b)^2\right] + 2B - r_a c_a - r_b c_b\right) \quad (3.32)$$

where:

$$s_a = \sin(\theta_v + \theta_a) \quad s_b = \sin(\theta_v + \theta_b)$$
$$c_a = \cos(\theta_v + \theta_a) \quad c_b = \cos(\theta_v + \theta_b)$$

Double Curve Position Calculation

$$0 = d_2 x_v^2 + d_1 x_v + d_0 \quad (3.33)$$

$$y_v = \tfrac{1}{2}\left[A_1 (x_v - r_a s_a - C_1)^2 + A_2 (x_v - r_b s_b - C_2)^2 + c_1\right] \quad (3.34)$$

where additionally:

$$d_2 = A_1 - A_2$$
$$d_1 = -2A_1 r_a s_a - 2A_1 C_1 + 2A_2 r_b s_b + 2A_2 C_2$$
$$d_0 = 2A_1 C_1 r_a s_a + A_1 r_a^2 s_a^2 + A_1 C_1^2 - 2A_2 C_2 r_b s_b - A_2 r_b^2 s_b^2 - A_2 C_2^2 + B_1 - B_2 - r_a c_a + r_b c_b$$
$$c_1 = B_1 + B_2 - r_a c_a - r_b c_b$$

Notice that (3.33) leads to two valid solutions for agent position when the sensor beams intersect different adjacent curved surfaces. Section 3.5.2 presents a method for choosing the correct solution when in this regime.

3.5.2 Configuration Selection

Now that we know that there are three possible observation configurations we need a procedure to select the appropriate calculation for any set of range measurements, and also potentially select the proper estimate from that calculation if multiple solutions exist. Section 3.5.1 implies that there are effectively four solutions for two spliced curves and seven for three curves[4]. Given an initial 'home curve' we can always limit the problem to a range of three curves (home, previous, and next), thus, we seek a procedure to select the correct position calculation from these multiple solutions. Once such procedure has been successfully implemented in a MATLAB simulation and is described below:

1. Begin in a position such that both beams intersect a single 'home curve' (index 0 in panel (a) of Figure 3-12). Develop an initial position estimate using (3.31) and (3.32).

2. Take new range measurements on the next timestep. Compute five potential positions as follows: one assuming both beams observe the home curve, two assuming one beam intersects the left-hand curve and one the home curve, and two assuming that one beam intersects the home curve and one the curve to its right.

3. Validate each of these solutions. Since the splice points between each curve are known, beams can be virtually projected from the calculated estimates to determine whether their endpoints lie on physically meaningful sections of the appropriate curves. Invalid solutions should be discarded at this step.

4. For all remaining valid solutions, calculate a hybrid angle/distance metric α:

$$\alpha = \quad \arccos\left(\frac{\mathbf{a}\cdot\mathbf{b}}{|\mathbf{a}|\cdot|\mathbf{b}|}\right) \cdot |\mathbf{a}-\mathbf{b}| \tag{3.35}$$

where:

[4]Again, we require that a maximum of one splice point (curve intersection) may exist between the sensor beams.

$$\mathbf{a} = \begin{bmatrix} x_i - x_k & y_i - y_k \end{bmatrix}^T$$
$$\mathbf{b} = \begin{bmatrix} x_k - x_{k-1} & y_k - y_{k-1} \end{bmatrix}^T$$

5. Select the current agent position estimate to be the one with the smallest α value.

6. If chosen estimate is straddling a splice point and previous estimate was not, shift indices to make the new curve become the 'home curve.'

3.6 Feature-Based Navigation

The previous localization methods presented in this chapter all involve fitting range measurements from the DVL to surfaces of known curvature. While these methods can be useful in many real-world applications, there are a number of cases in which the principle of fitting range data to a curve is not feasible. Figure 3-8, for example, shows that positioning errors increase drastically when the curvature of a surface becomes small from the agent's viewpoint. In the case of flat surfaces we can revert to the procedure presented in Section 3.2; however, this method provides no means of estimating the agent's horizontal position. Furthermore, the DVL curve-fitting localization methods also require complete *a priori* knowledge of the target surface. This is a reasonable demand in ship-hull inspection; however, removing this restriction would be desirable as it would widen the applications for AUVs operating under range-based localization.

If a surface is either too flat or too complex to apply curve-fitting localization procedures, the next logical choice would be to navigate relative to features identified through repeated observations. After features are extracted from raw sonar returns, their estimated locations can be integrated into a SLAM framework which allows for both recursive vehicle position estimation and environmental map construction. These methods are commonly applied to data from scanning sonars such as the Blue-View Blazed Array; however, it is also possible to 'mechanically scan' the DVL and

generate a coarse approximation of what a multi-beam or true scanning sonar would observe.

Once a set of data is recorded using two beams of the DVL, features must be extracted. A major drawback of searching for features with the DVL beams is that if the sensor is pitched downward for use as a pair of range-finders, it can no longer provide hull-relative velocity information. Without a good estimate of vehicle location, data cannot be appropriately reconstructed. This issue can be partially circumvented by taking data during a series of yaw-only maneuvers. Typically vehicle yaw sensors are fairly accurate over short time intervals, allowing for decent data reconstruction.

A series of experiments was performed in a controlled environment in which the DVL was mounted on the end of a gantry robot and scanned along the inner surface of a tank. Data were recorded with known sensor positioning to analyze the DVL's ability to recognize various features placed along the tank wall. Figure 3-13 illustrates how a relatively steep-angled target was accurately observed.

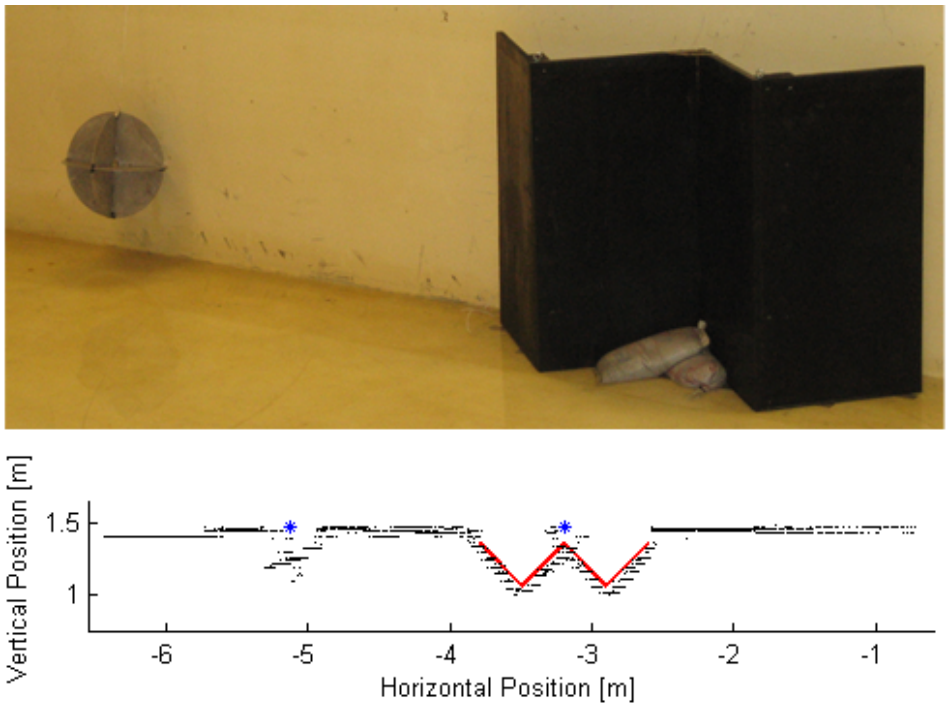

Figure 3-13: DVL data taken in an indoor tank showing both a radar reflector and a 'w'-shaped target. Notice that feature-extraction techniques have been successfully employed on this data.

In these experiments, a simple least squares algorithm was implemented based on principles presented in §1.4 of [14] to fit data to straight lines. These lines and their points of intersection were used to identify simple features in the data. Use of the Hough Transform [1] was also explored as applied by Tardos in [15]. While initially appearing promising, this method is ultimately better-suited for scanning sensors (i.e., laser scanners, imaging sonars, etc.) that return a large array of points at each timestep. With many sonar returns from a single point source, each can be represented by an arc indicating the beam spread. Features can then be extracted as intersections and shared tangents of these arcs as reported by the Hough Transform. Since the DVL produces only two range measurements per timestep, the Hough Transform method does not appear to be an efficient way to extract features.

In addition to testing with the DVL in a tank attached to a gantry system, we also experimented with taking range data while the DVL was integrated with the HAUV. Figure 3-14 illustrates this scenario with range vs. time plots for the case where the vehicle was pushed laterally back and forth in front of a 'step' target on the pool wall. The target is clearly visible in the raw time data, inferring that taking a range-derivative would be an acceptable method of locating the ends of such a feature. Again, using this sensor information for navigation with no prior knowledge of vehicle position would be quite difficult.

Although not conclusive, the tests described in this section and several others have shown that the DVL is capable of obtaining sufficient range data to generate a fairly good representation of its observed two-dimensional environment. At least in the short term, the limitations of the data reconstruction and feature extraction processes described above casts range-based feature detection as a suitable supplement for a larger localization procedure rather stand-alone navigation tool. Further effort would be required before these procedures are developed to a point where they can be applied on a vehicle.

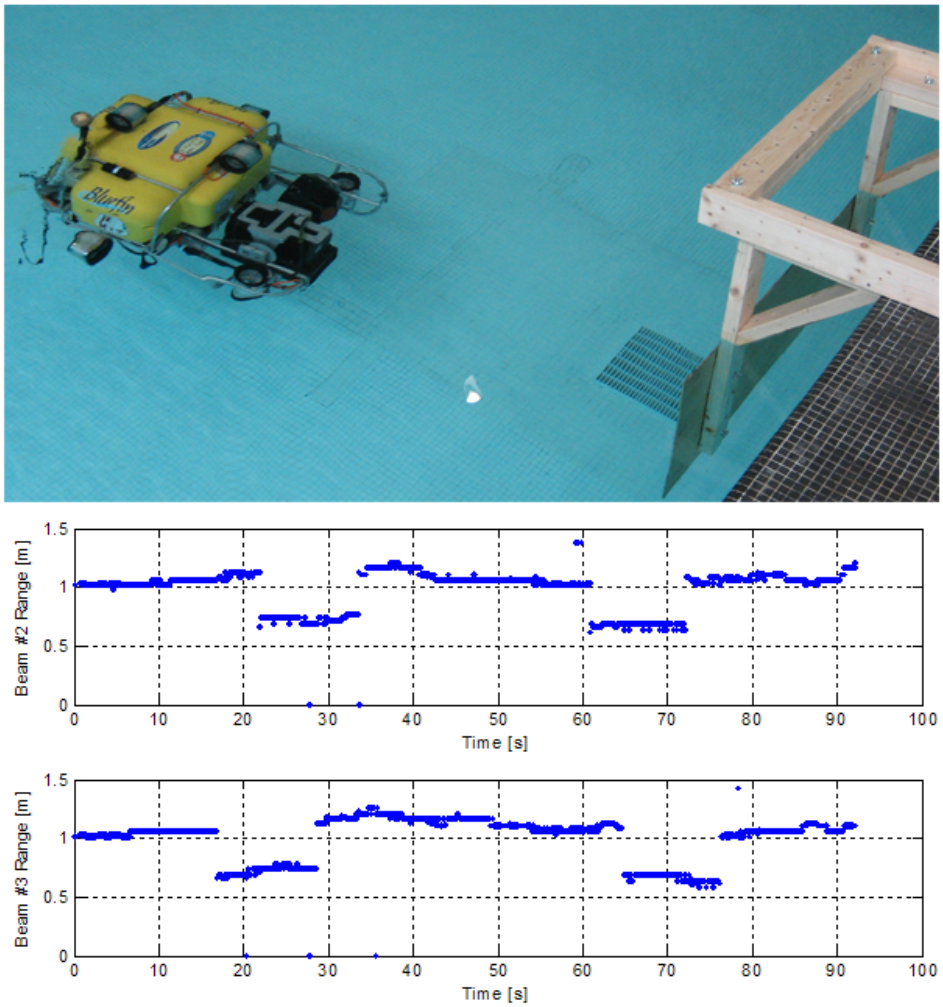

Figure 3-14: DVL data recorded while translating the HAUV laterally across a 'step' target in a swimming pool.

3.7 Summary and Extensions

This chapter presented several methods of range-based navigation and an EKF framework for their simulation and implementation. The utility of these methods is limited by several assumptions including that the target curvature is known, that it can be modeled by a series of simple functions, and that accurate vehicle yaw information is available. Initial results and simulations indicate that such procedures are indeed useful as presented in a certain set of inspection-related scenarios; however, the scope of applicability of curvature-based localization can be greatly expanded with further

developmental effort.

Although more advanced image- and scanning-sonar- based navigation techniques have been widely adopted, the present curvature-based solution is attractive because of its simplicity, minimal computational requirements, and application to navigation in truly hostile environments. The algorithms presented in this chapter rely on a minimum of two range measurements which need not always be provided by a DVL as we consider here; rather, this method can be implemented on nearly any land, air, or undersea craft equipped with at least two range-finders. The curvature-based localization technique can either serve as a redundant pose estimator to more complex scanning techniques or it can assume full localization responsibility in situations where more sophisticated sensors are inoperable, e.g., replacing a vision-based system in dark or murky environments.

In addition to extending this chapter's localization methods to other forms of curvature, improving the spliced-curve navigation algorithms, and developing the feature-detection capabilities, it may also be interesting to consider the case of three-dimensional curvature-based localization using the DVL. In this scenario, the sensor would be aimed normal to the ship hull as in the current inspection procedure (see Figure 1-4) to allow for both a velocity estimate and four range observations. Given this sensor information and a prior map of the target, the inspection vehicle would ideally be able to correct its dead-reckoned position with localization updates based on where the observed ranges fit with the target surface.

Chapter 4

Experimental Range-Based Navigation

A simple surface craft was developed as a cost-effective method of performing initial range-based navigation algorithm testing without requiring extensive HAUV operation time. Guaranteed planar motion and use of an available laser range-finding sensor are among the advantages realized by using a floating robot over an AUV for these tests. This chapter provides an overview of the hardware and software associated with the raft system and its real-time application to curvature-based localization. Results from servoing trials are shown in Section 4.6 to confirm expected performance characteristics.

4.1 Raft Overview and Development

The raft platform was designed to be inexpensive, straightforward to model, and relatively simple to fabricate. As a system, the raft has three degrees of freedom (two planar translations and a yaw rotation) which are fully controlled by a set of four thrusters placed at each of its corners. The thrusters are mounted on cylindrical foam pontoons which support a square aluminum frame and a smaller acrylic deck. A Hokuyo URG miniature laser scanner is affixed to the center of the deck and is used to both simulate DVL beam returns and to determine the raft's relative yaw angle.

In order to keep the raft relatively light and the size of its pontoons small, all power and control electronics are housed external to the vehicle and are connected via a tether cable. Although this cable adds non-trivial torque and drag disturbances to the system, the feedback controller employed has sufficient authority to overcome most of these dynamic effects. Overall system control is handled by software running on a local computer which can be accessed remotely via SSH over a network for both development and execution.

The raft hardware and software were developed and tested in a confined tank environment. Initial experimentation was carried-out by taking range measurements to the flat tank walls; however, a free-standing acrylic parabolic surface was also constructed to test the algorithms developed in Chapter 3. While this raft system does not capture all aspects of localization using sonar-based sensors, it does provide an inexpensive, accessible system for developing a real-time implementation of these navigation algorithms.

4.1.1 Mechanical Structure

The major mechanical design objectives for the raft were to minimize both overall size and weight (and thus also mass and rotational inertia) while maintaining pitch and roll stability. The former issues of weight and size minimization were accomplished by constructing a small frame to hold only the necessary components (sensor and actuators) and by using shore power and control electronics, while the latter stability issues were addressed by providing a relatively wide base.

Ample raft buoyancy is attributable to $6''$ diameter pontoons that reside at each of the four corners of the frame. Each pontoon is constructed from two joined $1''$ thick foam cylinders giving the raft an absolute maximum buoyancy of approximately 8lbs (about 225in^3 displacement) in fresh water. Acrylic mounting plates located above and below each pontoon were fabricated on a standard laser-cutter. These plates allow the pontoons to be connected by a frame made of $\frac{1}{2}''$ aluminum bar stock which also serves to support the raft's main acrylic deck. When fully assembled, the vehicle measures approximately $17.5''$ on each side although the pontoons are spaced

just 11.5″ on center. CAD drawings of the raft's main structural components are provided in Appendix B. Table 4.1 gives an overview of the mass distribution:

Component	**Qty.**	m_i $[kg]$	J_i $[kg \cdot m^2]$	r_i $[m]$	**Mass** $[kg]$	**Inertia** $[kg \cdot m^2]$
Laser Scanner	1	0.144	3.000e-7	0.000	0.144	3.000e-7
Deck Plate	1	0.337	4.676e-4	0.000	0.337	4.676e-4
Frame Bar	4	0.136	9.816e-5	0.146	0.544	1.200e-2
Pontoon	4	0.220	0.000e+0	0.207	0.880	3.754e-2
Total					1.905	5.000e-2

Table 4.1: Actual raft mass distribution. Columns 3 - 5 indicate measured component mass, calculated inertia, and distance from vehicle center of mass. The last two columns indicate total component mass and inertia contributions (inertia calculated by the parallel axis theorem).

4.1.2 Electrical Systems

Thrusters

Simple, inexpensive thrusters were built for the raft similar to those used in the Sea Perch educational Remotely-Operated Vehicle (ROV) developed by the MIT Sea Grant College Program[1]. Each thruster consists of a RadioShack 9-18V DC hobby motor (part number 273-256) placed inside a standard film canister and potted with sealing wax. A $1\frac{3}{4}''$ propeller from Dumas Products, Inc. (part number 3003) is pressed onto the motor shaft. While these thrusters are fairly imprecise and difficult to characterize, their low cost (roughly $7.00 each) and relative ease of manufacture makes them well-suited for this application. When used in conjunction with the motor controller described in Section 4.1.2, these thrusters were experimentally found to have force constants of approximately 0.0035N/count.

Motor Controller

The raft motor control unit serves as an interface between the PC-based control software and the robot's four thrusters. Pulse Width Modulation (PWM) is one

[1]Construction details for the Sea Perch are available online from the MIT Sea Grant College Program at http://web.mit.edu/seagrant/edu/seaperch/BuildingSP/BuildingSP.html.

Figure 4-1: A Sea Perch style thruster constructed from a DC hobby motor sealed inside a standard film canister.

of the simplest methods for controlling DC motors from a digital source, and an initial motor controller was developed based on this concept. In this design, an Atmel Atmega32 AVR microcontroller received commands from the PC and produced four channels of 8-bit PWM. These inputs were fed to a pair of JRC NJM2670 H-bridge driver chips which modulated current to the thrusters. This design was indeed functional; however, peak current loads approached the H-bridge maximums and the PWM induced motor voltages were incapable of driving the thrusters through their desired operating velocity ranges.

To overcome the challenges associated with the PWM-based motor controller, a second unit was designed using operational amplifiers (op-amps) for more precise, analog control. An Atmega32 is again at the heart of the motor controller; however, the microcontroller in the new unit is connected to a Maxim 5250 Digital to Analog Converter (DAC) configured in bipolar output mode. The four DAC voltages in turn are routed to a bank of TI OPA548T power op-amps which are each rated for 3A continuous (5A peak) current. This DAC-based controller performs much better than the PWM version and was integrated into the final raft system. A full schematic for this design is provided in Appendix C.

Both motor controllers share a very similar interface for communication between the high-level algorithmic software and the physical thrusters. Shown in Figure 4-2, the DAC-based motor controller communicates with the control PC via a 9800-N-1

serial link (see commands in Table 4.2).

Function	Command Syntax	Definitions
Set Motor Speed	`m#%xxx<CR>`	`#` = {1-4} to set motor # `%` = {f,r} (f)orward or (r)everse `xxx` = {0-511} motor voltage 0-12 VDC `<CR>` = ASCII `0x0D` character
Read A/D Channel	`a#<CR>`	`#` = {0-1} channel to read `<CR>` = ASCII `0x0D` character
Zero All Speeds	`k`	ASCII `0x6B` character
Toggle All Outputs	`<SPACEBAR>`	ASCII `0x20` character

Table 4.2: Commands recognized by the raft motor controller. Note that the serial connection is specified at 9800-N-1 with no flow control. Controller unit returns * for success and ! for failure, preceded by a 10-bit integer if reading an A/D channel. The two A/D channels are connected to the DAC reference voltages.

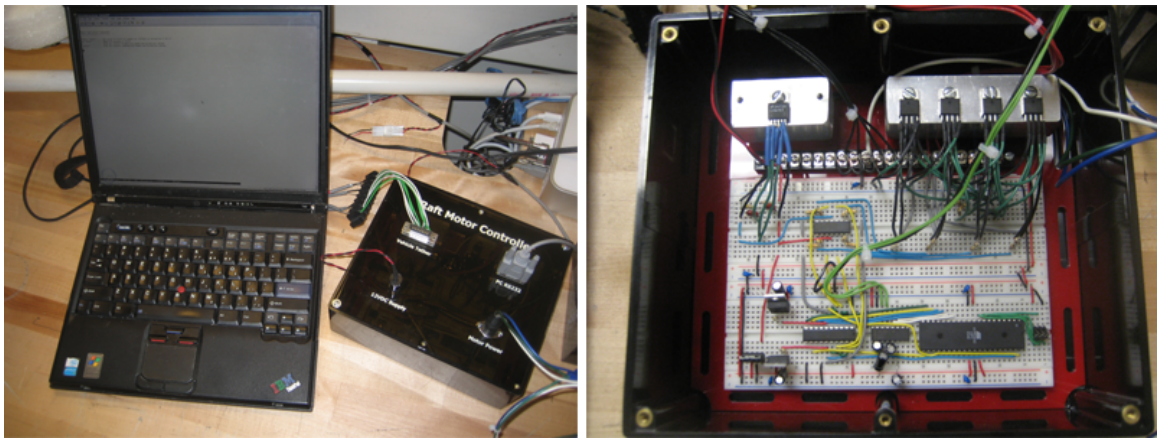

Figure 4-2: The custom-built motor controller used to drive the raft's four thrusters.

4.1.3 Sensors

The Hokuyo URG laser scanner[2] is the only sensor employed by the raft. This miniature scanner (shown in Figure 4-3) measures 50mm x 50mm x 70mm and weighs a mere 160g. With a 240° operating window and a range of 20mm to 4m, the sensor is well suited for the present application. Communication between the scanner and

[2]Some limited sensor information is available from the Hokuyo Automatic Co., LTD website at: http://www.hokuyo-aut.jp/products/urg/urg.htm

the control PC occurs over a USB 2.0 cable which comes through the tether together with its external 5.0VDC supply power and the individual thruster currents.

The navigation algorithms presented in Chapter 3 require two range measurements and a yaw angle, all of which can be derived from the laser scanner. Specifically, two range bins separated by a pre-determined angle are used in place of the two planar DVL beams (arranged 20.7° on either side of center for a total separation of 41.4°). As explained in Section 3.3, the DVL curvature-based localization algorithm relies not only on two acoustic range measurements, but also on a world-referenced vehicle heading. On the HAUV, this quantity is obtained by means of blending a compass reading (when available) with an integrated rate gyro. Since such sensors are not available on the raft platform, the Hokuyo is again employed and the vehicle yaw is determined by the relative position of the parabolic target surface. The algorithms for obtaining both the vehicle (x_v, y_v) position and its θ_v yaw orientation are explained in Section 4.2.

Figure 4-3: The Hokuyo URG laser scanner is used on the raft to simulate all relevant HAUV sensors.

4.1.4 Parabolic Target

An 8″-tall parabolic target was fabricated from 4.5mm acrylic to fit the equation $y = -0.015x^2$ where x and y are taken in inches. The target measures 36″ across $(-18'' \leq x \leq 18'')$ and it can be easily tied to the side of a tank for use in raft

navigation (see Figure 4-9). Figure 4-4 shows the noise properties for the actual target where partial derivatives transform range measurement errors into x_v and y_v position deviations (similar to Figures 3-7 and 3-8 in Section 3.3.3). Notice that this target is flatter than the one used in Chapter 3 which implies that the experimental horizontal positioning should be somewhat less accurate than the simulated results.

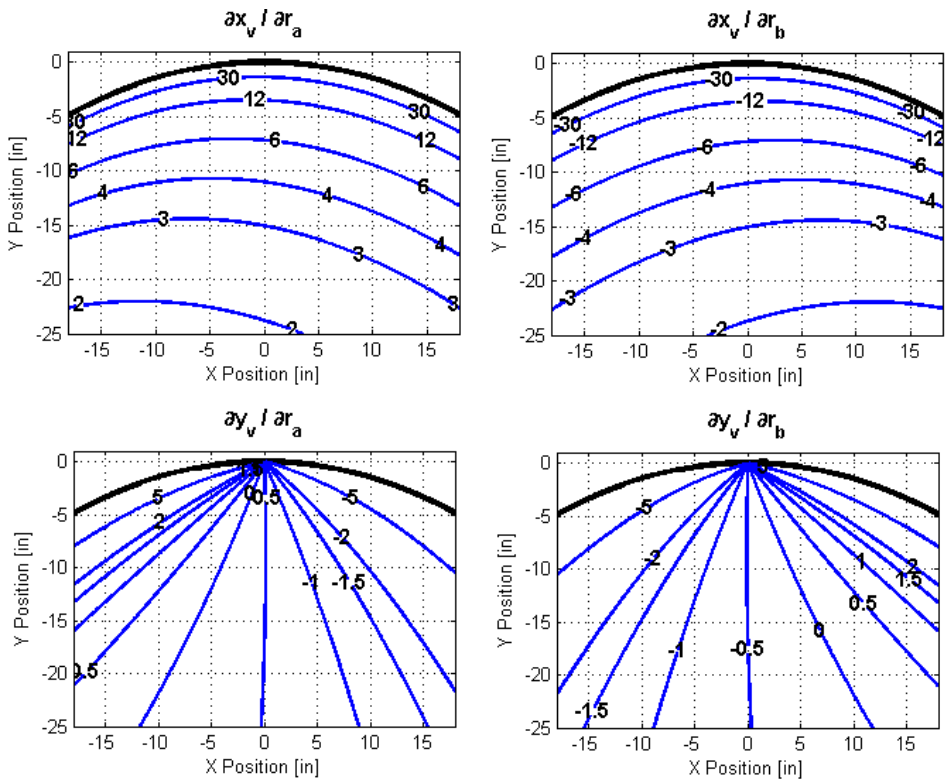

Figure 4-4: Noise properties for the actual parabolic target used in testing. Note that while the length scale for this figure can be taken as any unit of distance, dimensions are labeled in inches as the target is approximately 36″ wide.

4.2 Yaw and Position Calculation Algorithms

Sections 4.2.1 and 4.2.2 present algorithms for using the Hokuyo URG laser scanner to determine raft yaw and planar position with respect to a parabolic wall. These algorithms rely on the the vehicle heading vector as well as the two range measurement vectors intersecting the target at all times.

4.2.1 Vehicle Yaw Calculation

1. Read in a vector r containing 769 laser range measurements. These measurements correspond to observations made at roughly 0.3516° increments for 135° on either side of the forward direction. Data are arranged from from rightmost to leftmost observation in the counter-clockwise scan (as viewed from above). Thus, the middle element ($r[385]$) corresponds to a range measurement made directly in front of the scanner.

2. Compute a 768-element difference vector $q = \delta r$ where $q[i] = |r[i+1] - r[i]|$. Note that this is essentially the absolute value of a derivative of the range measurements with respect to their angular positions. Since the target surface is curved, its angular derivative is nearly unity and the edges of the parabolic wall appear as spikes in q.

3. Select a threshold value p which will be used to identify the wall's edges.

4. Starting from index $i = 385$, *increment* i until $q[i] \geq p$. Store the first value of i which satisfies this inequality as *top*.

5. Compute the first endpoint position (x_1, y_1) where $x_1 = r[top] \cos\theta_{top}$, $y_1 = r[top] \sin\theta_{top}$, and $\theta_{top} = -45 + top * 360/1024$ in degrees.

6. Starting from index $i = 385$, *decrement* i until $q[i] \geq p$. Store the first value of i which satisfies this inequality as *bot*.

7. Compute the second endpoint position (x_2, y_2) where $x_2 = r[bot] \cos\theta_{bot}$, $y_2 = r[bot] \sin\theta_{bot}$, and $\theta_{bot} = -45 + bot * 360/1024$ in degrees.

8. Calculate the vehicle yaw as $\theta_v = -\arctan\frac{y_2 - y_1}{x_2 - x_1}$.

4.2.2 Vehicle Position Calculation

1. Start with desired angles θ_{ad} and θ_{bd} at which range measurements should be taken relative to the vehicle's forward direction. When simulating the DVL, $\theta_{ad} = +20.7°$ and $\theta_{bd} = -20.7°$.

2. Calculate the indices of the Hokuyo bins closest to each desired measurement as $idx = round\left((\theta_d + 135°) * 1024/360\right)$.

3. Calculate the actual angles θ_a and θ_b represented by the indices determined above. Each angle (in degrees) can be determined through $\theta = idx*(360/1024) - 135°$.

4. Determine observed ranges $r_a = r[idx_a]$ and $r_b = r[idx_b]$.

5. Apply (3.17) and (3.18) or other geometry-appropriate set of equations using r_a, r_b, θ_a, θ_b, and θ_v (from above) to determine the vehicle's Cartesian position (x_v, y_v).

4.3 Software Architecture

The real-time control for the raft platform was handled by software written in C++ on a Mac Mini PC running Ubuntu Linux. A simple matrix class called `easyMatrix` was created as part of this software for handling basic linear algebra operations. The matrix inverse and pseudoinverse functionalities of this package were developed using the code from the LU and SV decomposition methods presented in §2.3 and §2.6 of [11]. Figure 4-5 follows program flow through the major software components. While the main execution loop was successfully stabilized at 10Hz, latencies in retrieving sensor updates increased the minimum achievable sampling period to 0.4 seconds. Implications of this large delay are discussed in Section 4.5.

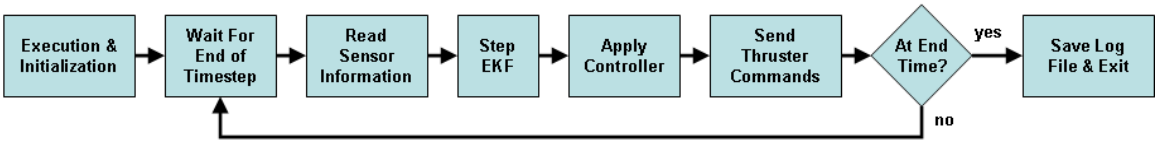

Figure 4-5: Overview of the raft control software. Code was written entirely in C++ and run in real-time with a sampling frequency of 2.5Hz.

4.4 Filter Implementation

An Extended Kalman Filter similar to the one described in Section 3.3.4 was included in the software to generate raft position estimates for use in control. The real-time implementation follows the theoretical development closely, however, the fully discrete form of the EKF was chosen to avoid difficulties associated with propagating the covariance matrix in continuous time. Durrant-Whyte presents a clear development of these filtering equations in [2]. The exact form of the EKF implemented on the raft system is given by (4.1) through (4.3).

<u>Prediction Step</u>

$$\begin{aligned} \hat{\mathbf{x}}_{\mathbf{k|k-1}} &= \mathbf{f}(\hat{\mathbf{x}}_{\mathbf{k-1|k-1}}, \mathbf{u}_{\mathbf{k-1}}) \\ \mathbf{P}_{\mathbf{k|k-1}} &= \mathbf{F}(\hat{\mathbf{x}}_{\mathbf{k-1|k-1}})\mathbf{P}_{\mathbf{k-1|k-1}}\mathbf{F}^T(\hat{\mathbf{x}}_{\mathbf{k-1|k-1}}) + \mathbf{G_k Q G_k}^T \end{aligned} \tag{4.1}$$

<u>Gain Calculation</u>

$$\begin{aligned} \mathbf{S_k} &= \mathbf{H_k P_{k|k-1} H_k}^T + \mathbf{R_k} \\ \mathbf{K_k} &= \mathbf{P_{k|k-1} H_k}^T \mathbf{S_k}^{-1} \end{aligned} \tag{4.2}$$

<u>Correction Step</u>

$$\begin{aligned} \hat{\mathbf{x}}_{\mathbf{k|k}} &= \hat{\mathbf{x}}_{\mathbf{k|k-1}} + \mathbf{K_k}[\mathbf{z_k} - \mathbf{h}(\hat{\mathbf{x}}_{\mathbf{k|k-1}})] \\ \mathbf{P}_{\mathbf{k|k}} &= \mathbf{P}_{\mathbf{k|k-1}} - \mathbf{K_k S_k K_k}^T \end{aligned} \tag{4.3}$$

Notice that the prior propagation step in (4.1) uses forward Euler integration in keeping with standard practice which makes the state transition jacobian $\mathbf{F}(\hat{\mathbf{x}}_{\mathbf{k-1|k-1}})$ relatively easy to compute. The large errors and potential for instability associated with this basic method of numerical integration can be minimized by reducing the size of the prediction timestep. Measurement-related quantities $\mathbf{z_k}$, $\mathbf{h}(\hat{\mathbf{x}}_{\mathbf{k|k-1}})$, $\mathbf{H_k}$, and $\mathbf{R_k}$ are identical for the discrete case to those presented in (3.19), (3.25), (3.21), and (3.26) where $m = 1$ for a single reading. The remaining matrices required for the

discrete EKF are computed as given below:

$$\mathbf{f}(\hat{\mathbf{x}}_{\mathbf{k-1|k-1}}, \mathbf{u}_{\mathbf{k-1}}) = \hat{\mathbf{x}}_{\mathbf{k-1|k-1}} + \Delta T \begin{bmatrix} \frac{X}{m} - \frac{b}{m}\dot{u} & \frac{Y}{m} - \frac{b}{m}\dot{v} & \frac{M}{J} & c_1 & c_2 & \dot{\theta}_v \end{bmatrix}^T \quad (4.4)$$

where:

$$c_1 = u\cos\theta_v - v\sin\theta_v$$
$$c_2 = u\sin\theta_v + v\cos\theta_v$$

$$\mathbf{F}(\hat{\mathbf{x}}_{\mathbf{k-1|k-1}}) = \begin{bmatrix} 1 & 0 & 0 & 0 & 0 & 0 \\ 0 & 1 & 0 & 0 & 0 & 0 \\ 0 & 0 & 1 & 0 & 0 & 0 \\ \Delta T\cos\theta_v & -\Delta T\sin\theta_v & 0 & 1 & 0 & \Delta T c_3 \\ \Delta T\sin\theta_v & \Delta T\cos\theta_v & 0 & 0 & 1 & \Delta T c_4 \\ 0 & 0 & \Delta T & 0 & 0 & 1 \end{bmatrix} \quad (4.5)$$

where:

$$c_3 = -u\dot{\theta}_v\sin\theta_v - v\dot{\theta}_v\cos\theta_v$$
$$c_4 = u\dot{\theta}_v\cos\theta_v - v\dot{\theta}_v\sin\theta_v$$

$$\mathbf{G_k} = \begin{bmatrix} \frac{\Delta T}{m} & 0 & 0 & 0 & 0 & 0 \\ 0 & \frac{\Delta T}{m} & 0 & 0 & 0 & 0 \\ 0 & 0 & \frac{\Delta T}{J} & 0 & 0 & 0 \end{bmatrix}^T \quad (4.6)$$

4.5 Testing and Tuning

As an initial filter accuracy test, the laser scanner was held stationary relative to the parabolic target described in Section 4.1.4, the raft controller was disabled (all gains zeroed), and the filter response was recorded. Figure 4-6 shows that the filter converges within the first two seconds to produce a vehicle position estimate that is both more accurate and precise than the raw sensor estimate from (3.17) and (3.18).

As expected, the vertical positioning accuracy greatly exceeds the horizontal accuracy.

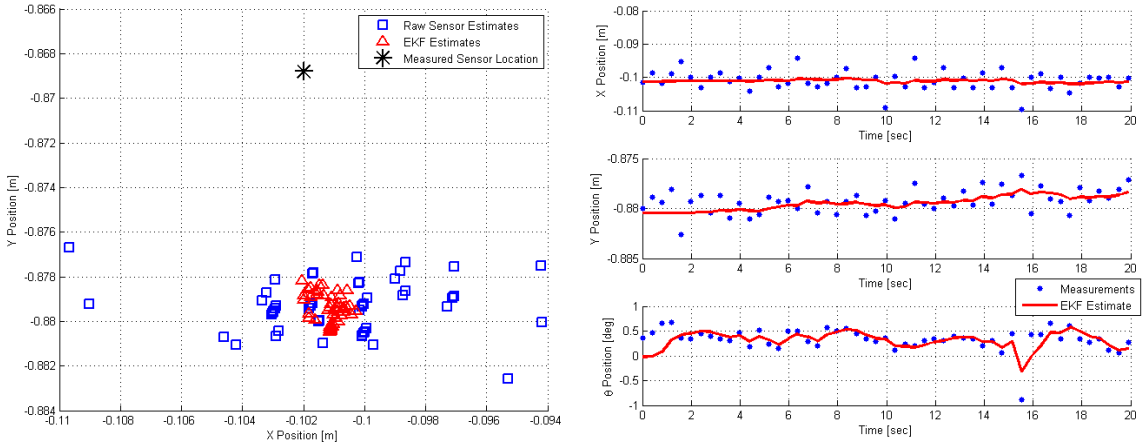

Figure 4-6: Static EKF positioning accuracy observed by holding the laser scanner stationary behind a downward-facing parabolic target centered on (0,0), setting all controller gains to zero, and significantly reducing the non-zero elements of $\mathbf{Q}$. Notice that the 0.1cm x position error represents 9.8% of the horizontal distance to the parabola's center while the 1.1cm y error represents only 1.3% of the vertical distance.

Controller gains for the first dynamic raft tests were selected using a linearized model of the system in the same manner as outlined in Section 3.3.2. Achieving a rapid responses was not feasible, though, due to the low (2.5Hz) system sampling rate imposed by latencies in reading from the laser scanner. With a Nyquist frequency of 1.25Hz bounding the estimator bandwidth, the maximum compensated system bandwidth was further reduced to 0.4Hz.

Manually tuning both controller gains and the elements of $\mathbf{Q}$, the estimator response time was set slightly slower than the Nyquist frequency at approximately 2 seconds (see Figure 4-7) while the compensated system responses were each tuned to damp-out in around 17 seconds (see Figure 4-10). Since the position responses had to be severely restricted, additional mechanical damping was introduced in the form of drag plates shown in Figure 4-8. With this addition, an approximate damping coefficient $b = 0.45$ was calculated for use in (4.4) and mass and inertia properties were adjusted to 2.4kg and 0.058kg·m^2, respectively.

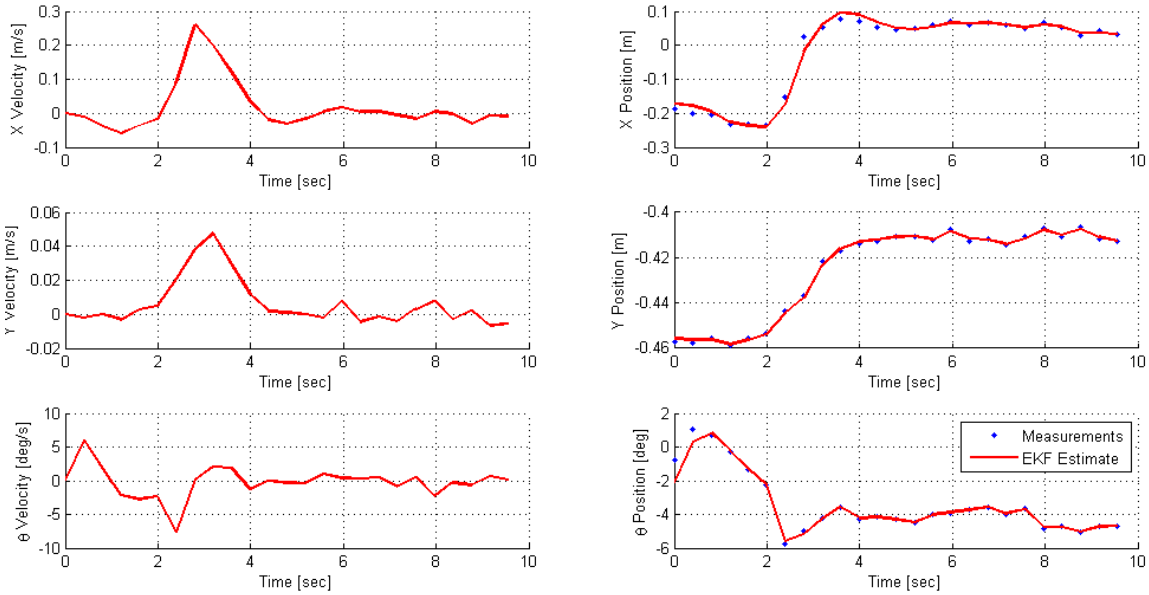

Figure 4-7: Response of the EKF state estimate to a step input in the x direction with all controller gains zeroed and elements of $\mathbf{Q}$ set at the values given in (4.8). Notice that the filter converges in around 2 seconds which is slightly slower than the 1.25Hz Nyquist frequency.

The tuned parameters chosen for final raft testing are given below:

$$\mathbf{K_c} = \begin{bmatrix} 0.80 & 0 & 0 & 32.00 & 0 & 0 \\ 0 & 0.20 & 0 & 0 & 28.00 & 0 \\ 0 & 0 & 0.13 & 0 & 0 & 3.55 \end{bmatrix} \tag{4.7}$$

$$\mathbf{Q} = \begin{bmatrix} 0.160^2 & 0 & 0 \\ 0 & 0.055^2 & 0 \\ 0 & 0 & 0.013^2 \end{bmatrix} \tag{4.8}$$

4.6 Results and Conclusions

Sensor and EKF position data from two raft missions are presented in Figures 4-10 and 4-12. Both missions involved servoing to and holding station at (0m,-0.635m) relative to the parabolic target with vehicle zero yaw. The first mission lasted roughly 40

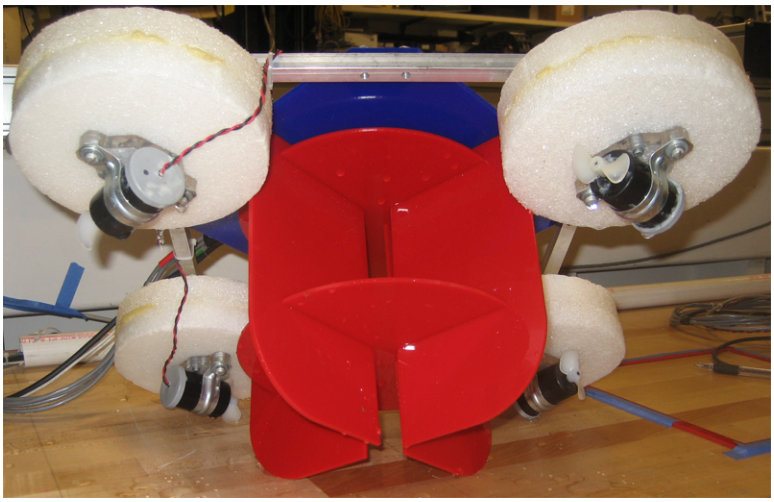

Figure 4-8: The raft equipped with drag fins designed to provide the system with additional mechanical damping.

seconds while the duration of the second was nearly 3.5 minutes. Controller response and closed-loop estimator convergence properties can be observed from the short mission data (see Figure 4-11). Each degree of freedom was independently disturbed during the longer mission to demonstrate system response characteristics.

While servoing at the desired position the range-based estimates have noise properties characterized by $\partial x_v/\partial r_a = 1.91$, $\partial x_v/\partial r_b = -1.9$, and $\partial y_v/\partial r_a = \partial y_v/\partial r_b = -0.52$. Range measurements $r_a = r_b = 0.646$m corresponding to the nominal raft location have associated standard deviations of 3.3mm according to Hokuyo specifications. Given these values, the expected x and y deviations are calculated from (3.26) as $\sigma_x = \sqrt{R_{11}} = 8.9$mm and $\sigma_y = \sqrt{R_{22}} = 2.4$mm.

Data from the final 15 seconds of the shorter run indicate experimental deviations of $\sigma_x = 5.5$mm and $\sigma_y = 2.3$mm. Position variations during the last 50 seconds of the longer test were slightly higher at $\sigma_x = 8.1$mm and $\sigma_y = 4.1$mm. In both cases these deviations lie within millimeters of their predicted values, validating the measurement sensitivity analysis as presented in Figure 4-4.

The data in in Figures 4-10 and 4-12 also provide insight into controller performance. Each of the three PD compensators yielded an under-damped response with a settling time on the order of 17 seconds which is very conservative considering

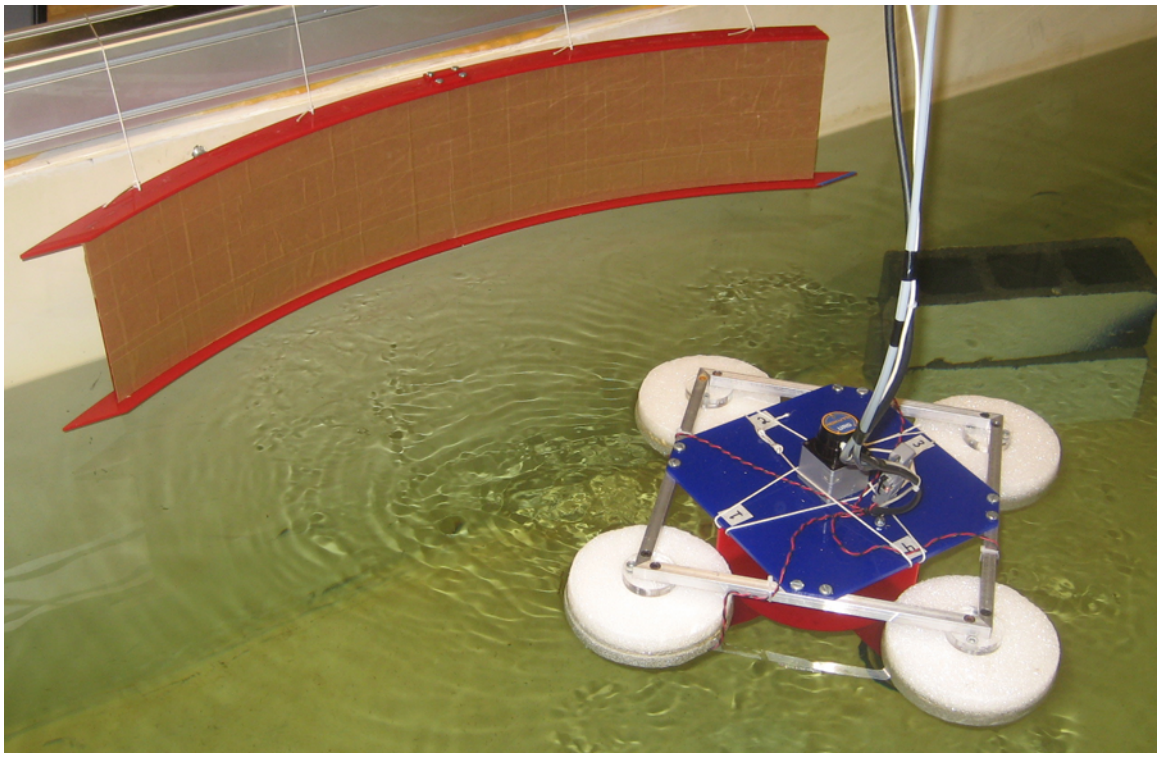

Figure 4-9: The raft robot servoing relative to a parabolic wall.

the average open-loop filter convergence time of roughly 2 seconds (see Figure 4-7). Performance of the raft itself could be greatly improved by increasing the sampling frequency, decreasing static friction in the thrusters, and eliminating tether effects. These modifications would increase the Nyquist frequency (allowing for higher controller bandwidth), boost *controller* positioning accuracy, and improve steady-state EKF estimation accuracy by eliminating DC position errors.

Despite sluggish controller response times, the raft robot has successfully demonstrated the validity of the range-based navigation algorithms developed in Chapter 3. It should be noted that this navigation strategy has not yet been implemented on an AUV using DVL range measurements. Future work required to achieve such results will involve examining the reflective properties of sonar beams incident upon parabolic surfaces as well as integrating the navigation filter with low-level vehicle attitude and depth controllers.

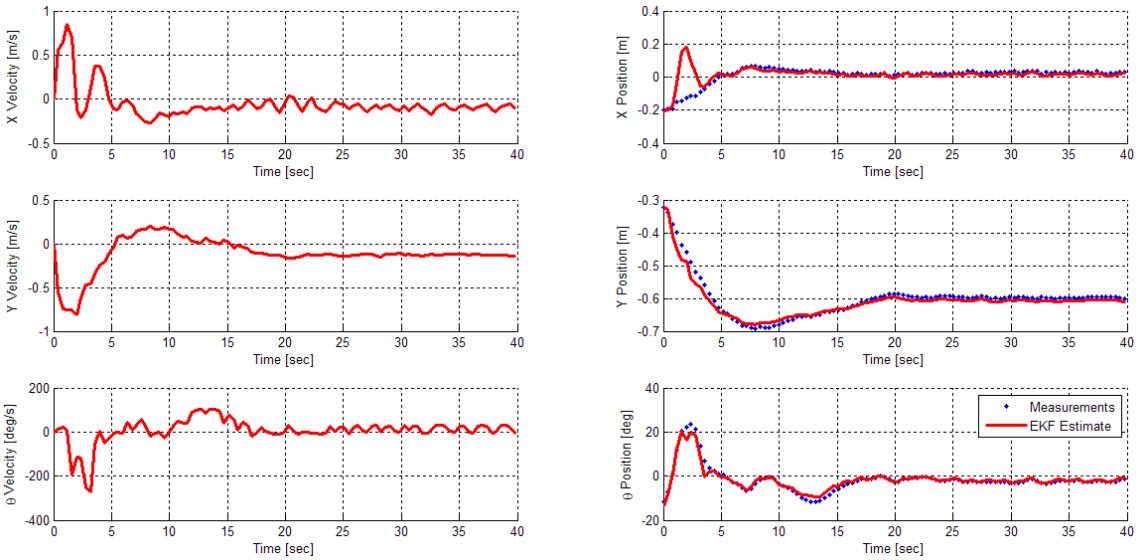

Figure 4-10: Estimated velocity and position data for the first raft mission. Average compensated system response time is approximately 17 seconds in each degree of freedom.

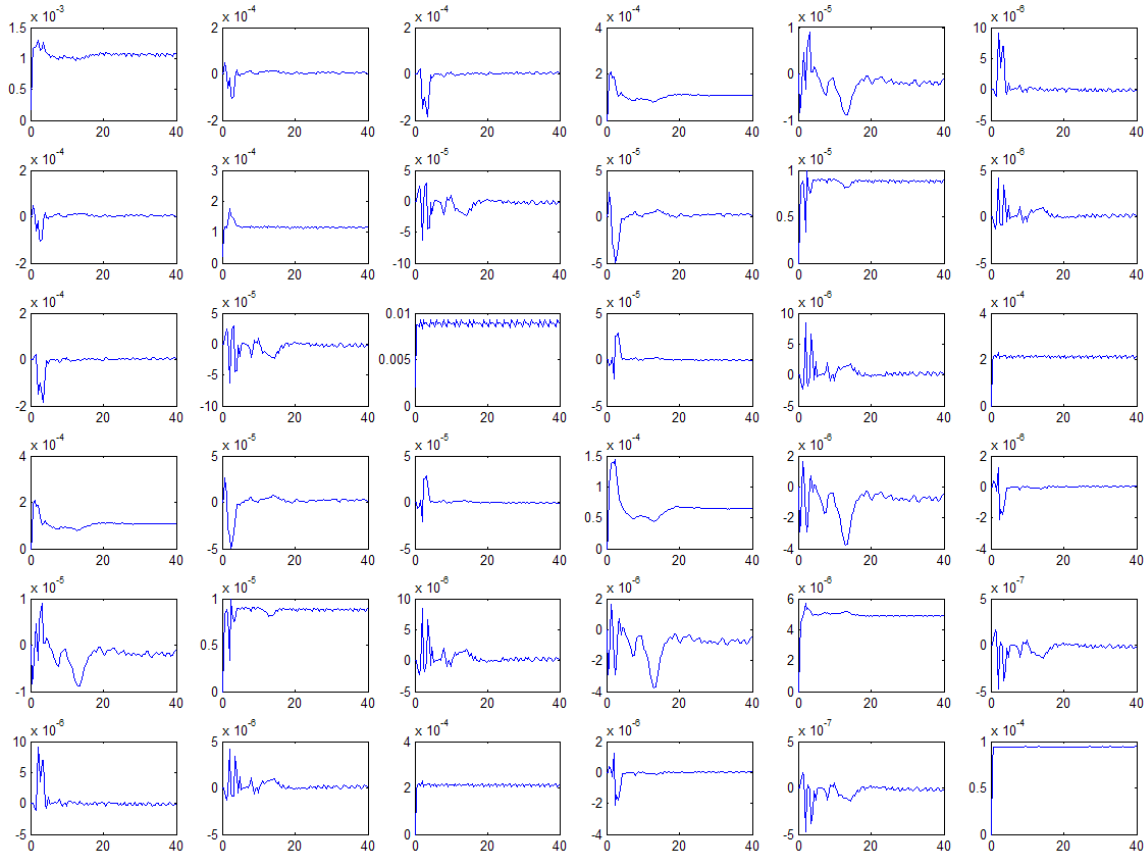

Figure 4-11: Evolution of elements in the error covariance matrix for the short raft mission from Figure 4-10. Notice that most correlated elements converge within about 5 seconds.

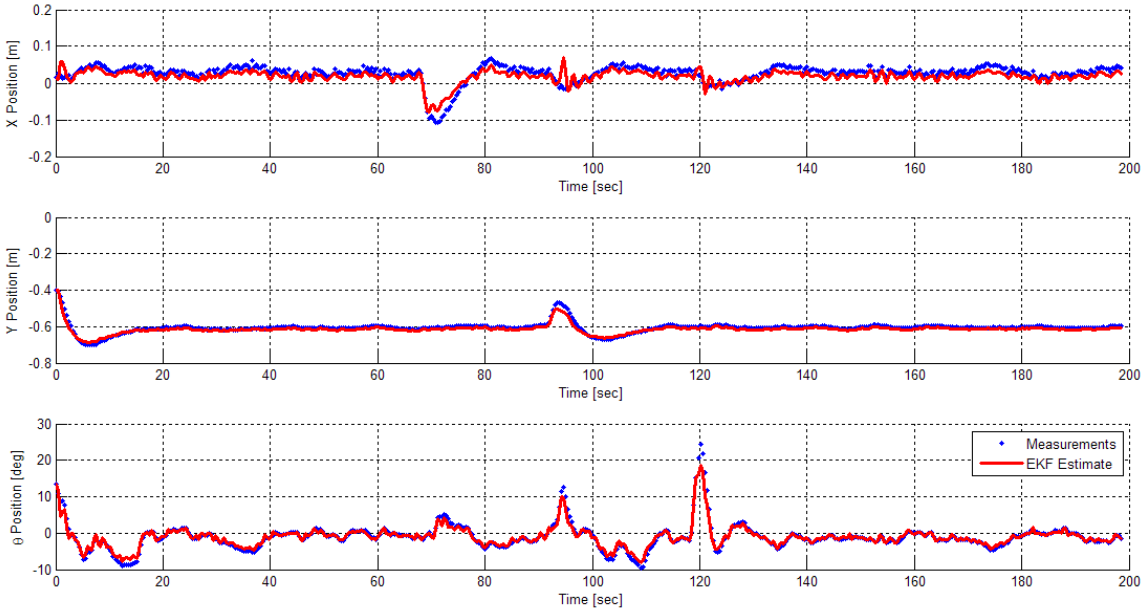

Figure 4-12: This 200-second test demonstrates the system's ability to hold station for a longer period of time. Disturbances were applied in the x, y, and θ directions after about 70 seconds, 90 seconds, and 120 seconds (respectively).

Chapter 5

Contributions and Future Work

5.1 Contributions

This thesis documents three main contributions to the hull inspection effort at MIT: a mechanical redesign of the initial HAUV prototype, development of range-based navigation algorithms to perform agent localization relative to a curved target, and creation of a floating robotic platform for algorithmic testing. Chapter 2 reviews the HAUV1B design process through which a new frame and foam body were designed. The range-based navigation work described in Chapter 3 has also been included in a paper to be presented at the July 2007 Field and Service Robotics conference in Chamonix, France. Finally, while scheduling conflicts prevented implementation of the curvature-based localization methods on the HAUV, Chapter 4 documents the design, fabrication, and testing of a robotic raft platform which navigates in real-time using these algorithms.

5.2 Future Work

With the HAUV1B operational, the project team is now implementing the hull-relative navigation capabilities demonstrated by the initial HAUV prototype. Once this process is complete, the next step will be to run real-time DIDSON-based SLAM on the HAUV1B using targets identified by a Computer-Aided Detection and Clas-

sification (CAD/CAC) program written by SeeByte Ltd. of Edinburgh, Scotland. HAUV development will continue through at least 2010 with the long-term goal of producing a compact system which can be quickly deployed and perform hull inspection autonomously with little (if any) *a priori* information.

Although not as critical as implementing DIDSON SLAM, significant opportunities also exist for integrating range-based localization into the overall HAUV navigation scheme. The algorithms developed in Chapter 3 have only been initially tested on the raft platform and have not yet been verified with acoustic sensors. Additionally, the raft robot itself would benefit from further hardware and software development to increase its sampling rate and reduce tether effects on the system dynamics.

The general curvature-based navigation algorithms must be further expanded prior to their application on actual ship hulls. The splicing procedure from Section 3.5 and in particular the switching metric α in (3.35) need to be carefully examined and tested for robustness. Development and testing of the two-dimensional slicing algorithm and spliced curve fitter explained in Figure 3-2 should proceed based on data from real ship hulls.

Also interesting are two potential extensions of curvature-based navigation. First, expanding the observation and state models to three dimensions could potentially allow for the use of all four DVL beams in developing $\{x, y, z\}$ vehicle position estimates. This procedure would permit much richer navigation trajectories as it removes the planar restriction of the algorithms from Chapter 3, but it would still require an accurate *a priori* hull model. A second logical extension to this work would employ a framework similar to Moran's multiple hypothesis tracking-based curvature reconstructor in [10] to simultaneously model the curvature of an unknown hull section and navigate based on that prediction.

Appendix A

HAUV1B Frame CAD Drawings

Note: The CAD drawings on the following pages are not reproduced in this document at their indicated scales.

HAUV 1B

Hovering Autonomous Underwater Vehicle

- MIT OCEAN ENGINEERING
- MIT SEA GRANT
- BLUEFIN CORPORATION

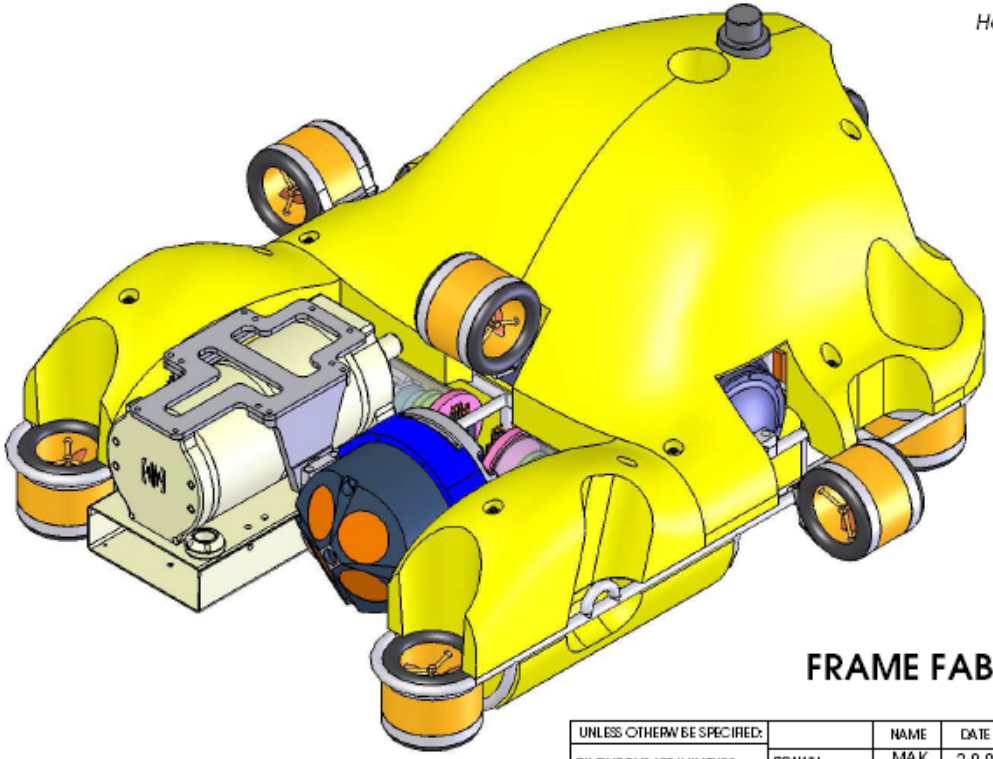

FRAME FABRICATION DRAWINGS

UNLESS OTHERWISE SPECIFIED:		NAME	DATE
DIMENSIONS ARE IN INCHES TOLERANCES: FRACTIONAL ± 0.005 TWO PLACE DECIMAL ± 0.005 THREE PLACE DECIMAL ± 0.005	DRAWN	MAK	2-9-06
	CHECKED		
	ENG APPR.		
FRAME MATERIAL ALUMINUM	MFG APPR.		
	Q.A.		
FINISH STANDARD	COMMENTS: CONTACT: MIKE KOKKO EMAIL: KOKKOM@MIT.EDU PHONE: 3-3075		
DO NOT SCALE DRAWING			

TITLE:

Cover / Iso. Assy.

SIZE	DWG. NO.	REV
A	HAUV1B	01

SCALE: 1:6 | SHEET 1 OF 16

5 4 3 2 1

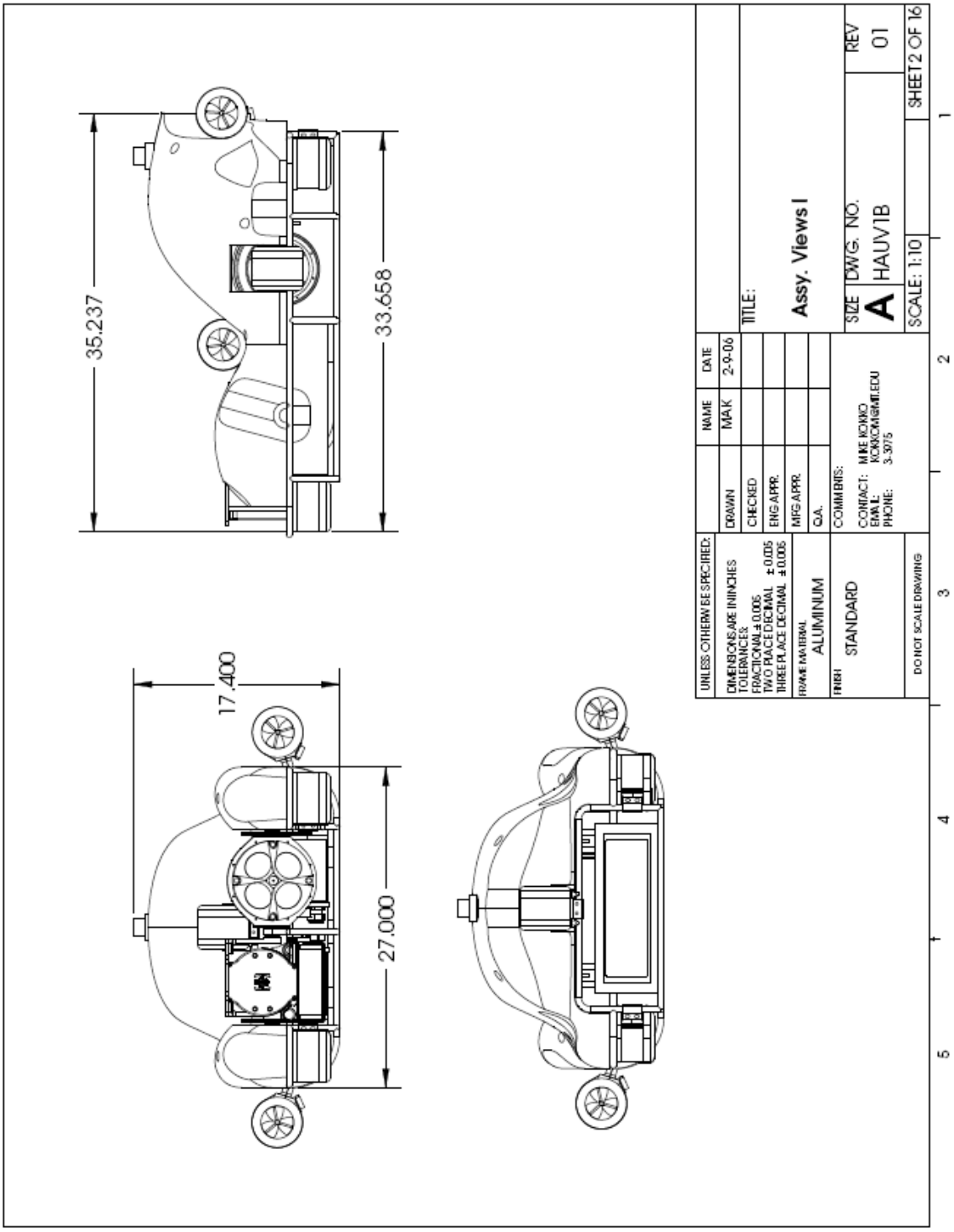
35.237
33.658
17.400
27.000
UNLESS OTHERWISE SPECIFIED:
DIMENSIONS ARE IN INCHES
TOLERANCES:
FRACTIONAL ± 0.005
TWO PLACE DECIMAL ± 0.005
THREE PLACE DECIMAL ± 0.005
FRAME MATERIAL
ALUMINUM
FINISH
STANDARD
DO NOT SCALE DRAWING
NAME
DATE
DRAWN
MAK
2-9-06
CHECKED
ENG APPR.
MFG APPR.
Q.A.
COMMENTS:
CONTACT: MIKE KOKKO
EMAIL: KOKKO@MTU.EDU
PHONE: 3-3075
TITLE:
Assy. Views I
SIZE
A
DWG. NO.
HAUV1B
REV
01
SCALE: 1:10
SHEET 2 OF 16
1
2
3
4
5

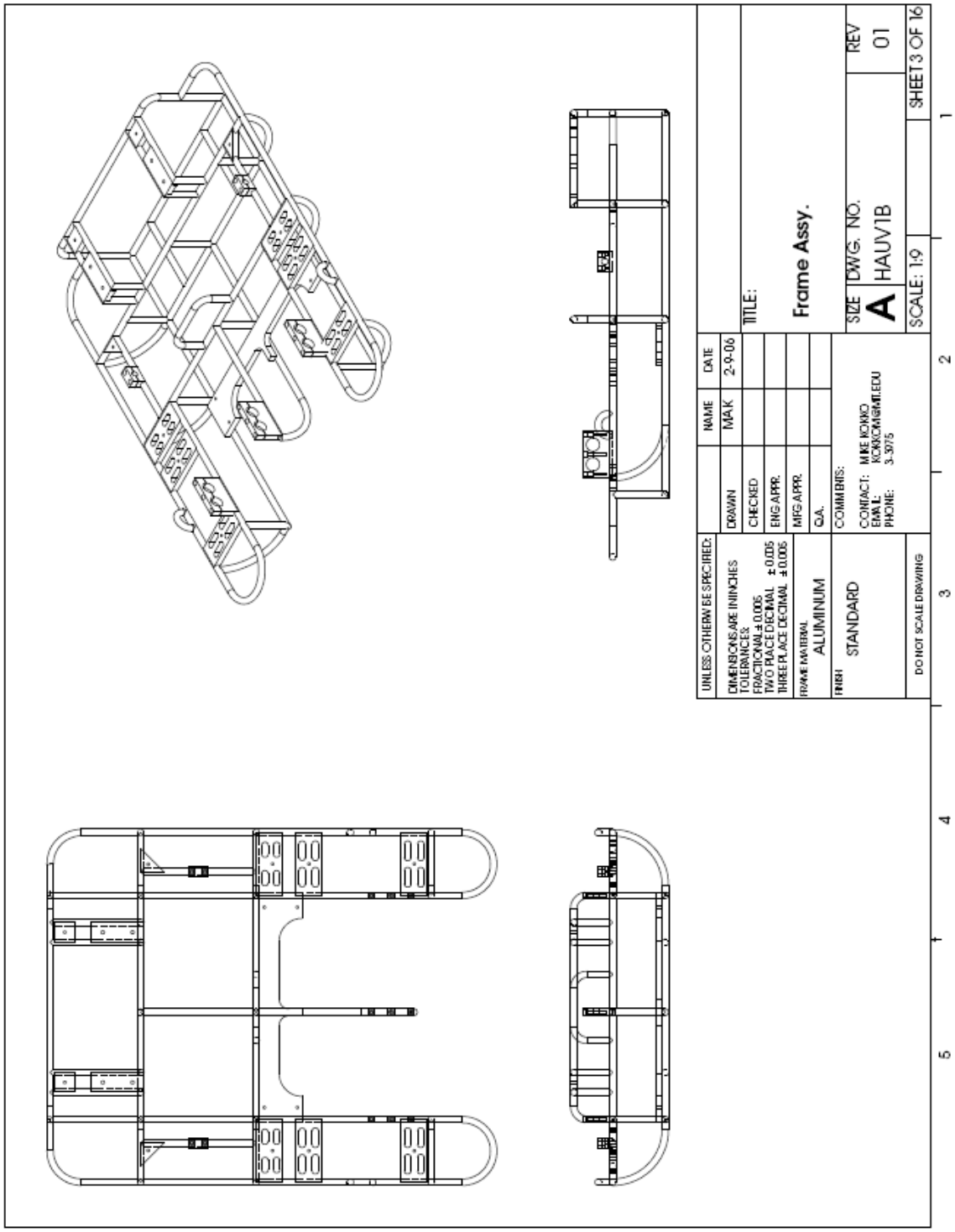
UNLESS OTHERWISE SPECIFIED:
DIMENSIONS ARE IN INCHES
TOLERANCES:
FRACTIONAL ± 0.005
TWO PLACE DECIMAL ± 0.005
THREE PLACE DECIMAL ± 0.005
FRAME MATERIAL
ALUMINUM
FINISH
STANDARD
DO NOT SCALE DRAWING
NAME
DATE
DRAWN
MAK
2-9-06
CHECKED
ENG APPR.
MFG APPR.
Q.A.
COMMENTS:
CONTACT: MIKE KOKKO
EMAIL: KOKKOK@MI.EDU
PHONE: 3-3075
TITLE:
Frame Assy.
SIZE
A
DWG. NO.
HAUV1B
REV
01
SCALE: 1:9
SHEET 3 OF 16

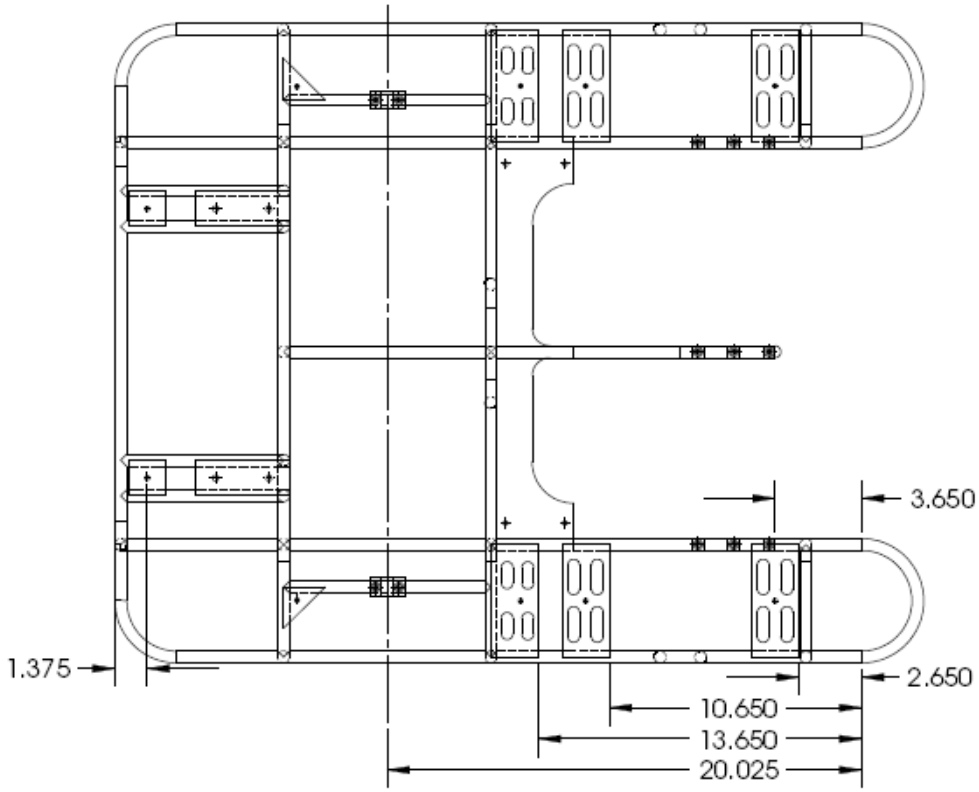

UNLESS OTHERWISE SPECIFIED:		NAME	DATE
DIMENSIONS ARE IN INCHES TOLERANCES: FRACTIONAL ± 0.005 TWO PLACE DECIMAL ± 0.005 THREE PLACE DECIMAL ± 0.005	DRAWN	MAK	2-9-06
	CHECKED		
	ENG APPR.		
	MFG APPR.		
FRAME MATERIAL ALUMINUM	Q.A.		
FINISH STANDARD	COMMENTS: CONTACT: MIKE KOKKO EMAIL: KOKKOM@MIT.EDU PHONE: 3-3975		
DO NOT SCALE DRAWING			

TITLE:

Frame Assy. Layout

SIZE	DWG. NO.	REV
A	HAUV1B	01

SCALE: 1:6 | SHEET 4 OF 16

5 4 3 2 1

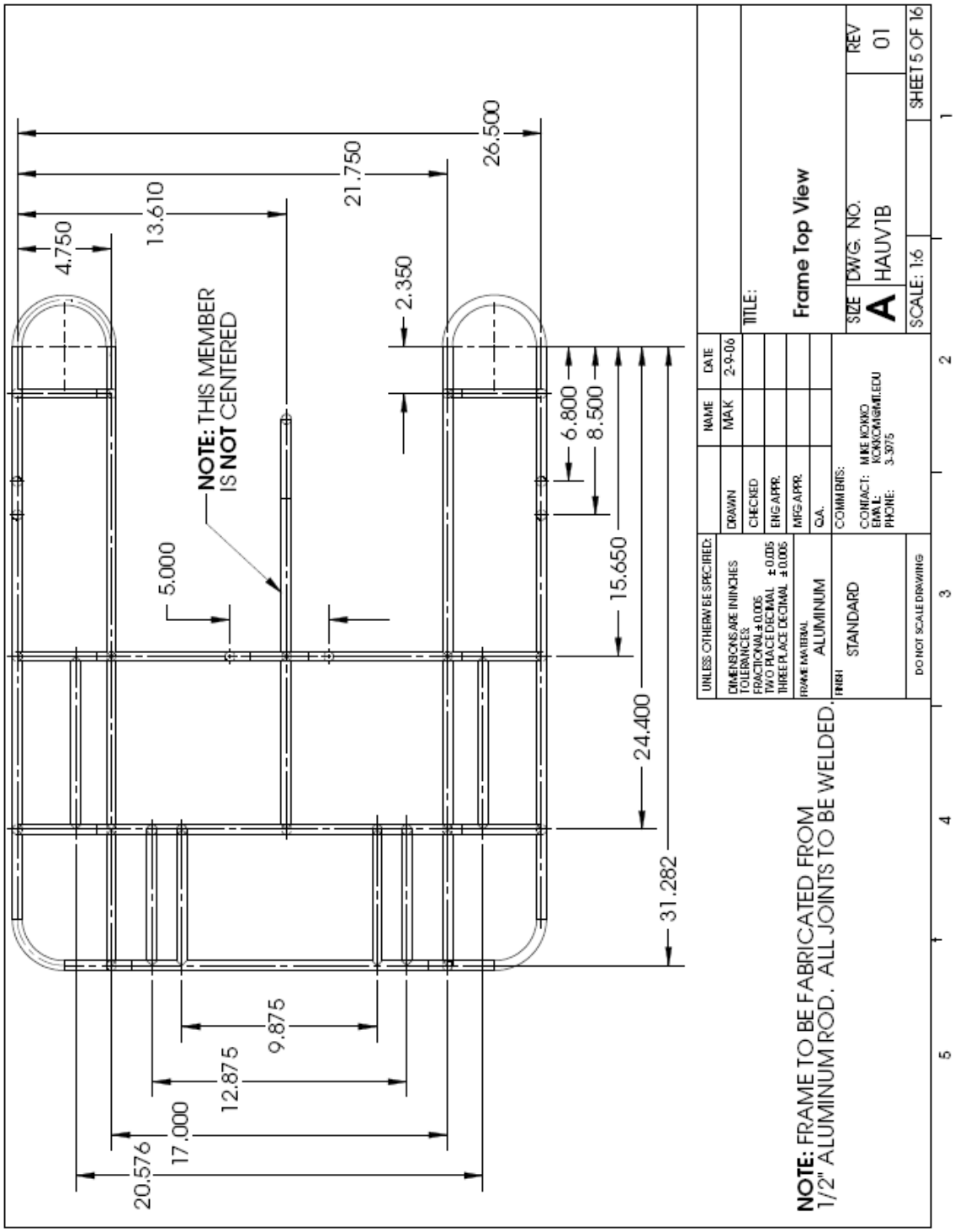
26.500
21.750
13.610
4.750
2.350
NOTE: THIS MEMBER IS NOT CENTERED
5.000
6.800
8.500
15.650
24.400
31.282
9.875
12.875
17.000
20.576
NOTE: FRAME TO BE FABRICATED FROM 1/2" ALUMINUM ROD. ALL JOINTS TO BE WELDED.
UNLESS OTHERWISE SPECIFIED:
DIMENSIONS ARE IN INCHES
TOLERANCES:
FRACTIONAL ± 0.005
TWO PLACE DECIMAL ± 0.005
THREE PLACE DECIMAL ± 0.005
FRAME MATERIAL
ALUMINUM
FINISH
STANDARD
DO NOT SCALE DRAWING
NAME
DATE
DRAWN
MAK
2-9-06
CHECKED
ENG APPR.
MFG APPR.
Q.A.
COMMENTS:
CONTACT: MIKE NOWKO
EMAIL: KONKOK@GMU.EDU
PHONE: 3-3075
TITLE:
Frame Top View
SIZE
A
DWG. NO.
HAUV1B
REV
01
SCALE: 1:6
SHEET 5 OF 16

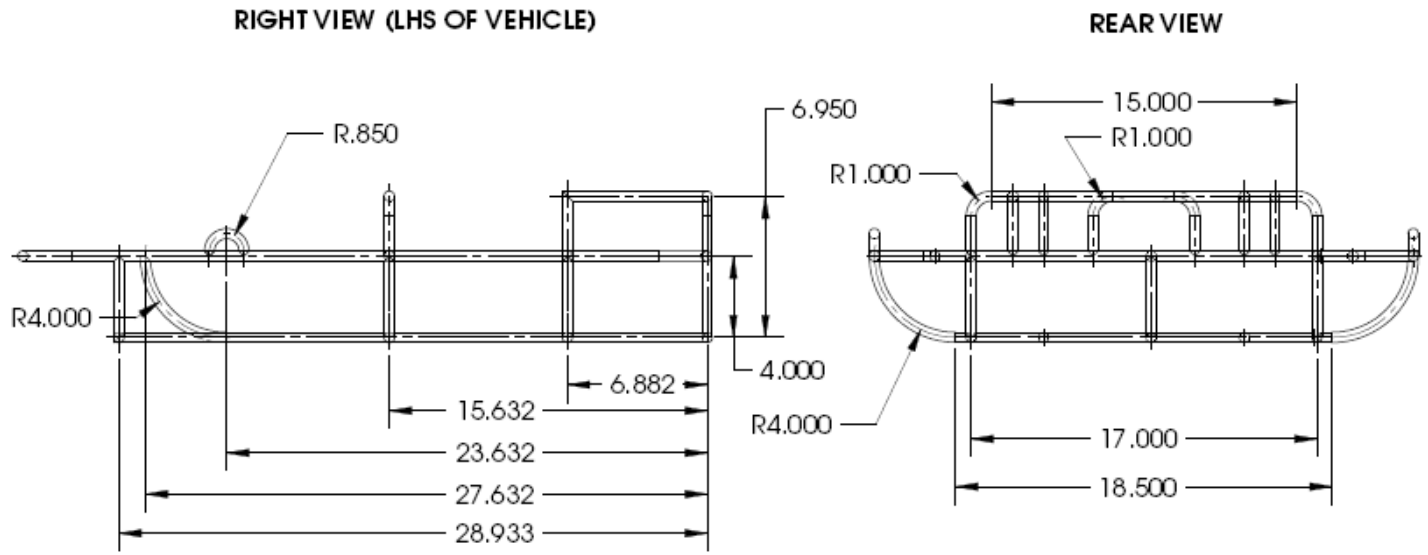

NOTE: FRAME TO BE FABRICATED FROM 1/2" ALUMINUM ROD. ALL JOINTS TO BE WELDED.

UNLESS OTHERWISE SPECIFIED:		NAME	DATE
DIMENSIONS ARE IN INCHES TOLERANCES: FRACTIONAL ± 0.005 TWO PLACE DECIMAL ± 0.005 THREE PLACE DECIMAL ± 0.005	DRAWN	MAK	2-9-06
	CHECKED		
	ENG APPR.		
	MFG APPR.		
FRAME MATERIAL ALUMINUM	Q.A.		
FINISH STANDARD	COMMENTS: CONTACT: MIKE KOKKO EMAIL: KOKKOM@MIT.EDU PHONE: 3-3975		
DO NOT SCALE DRAWING			

TITLE:

Frame Side/Back View

SIZE	DWG. NO.	REV
A	HAUV1B	01

SCALE: 1:7 SHEET 6 OF 16

5 4 3 2 1

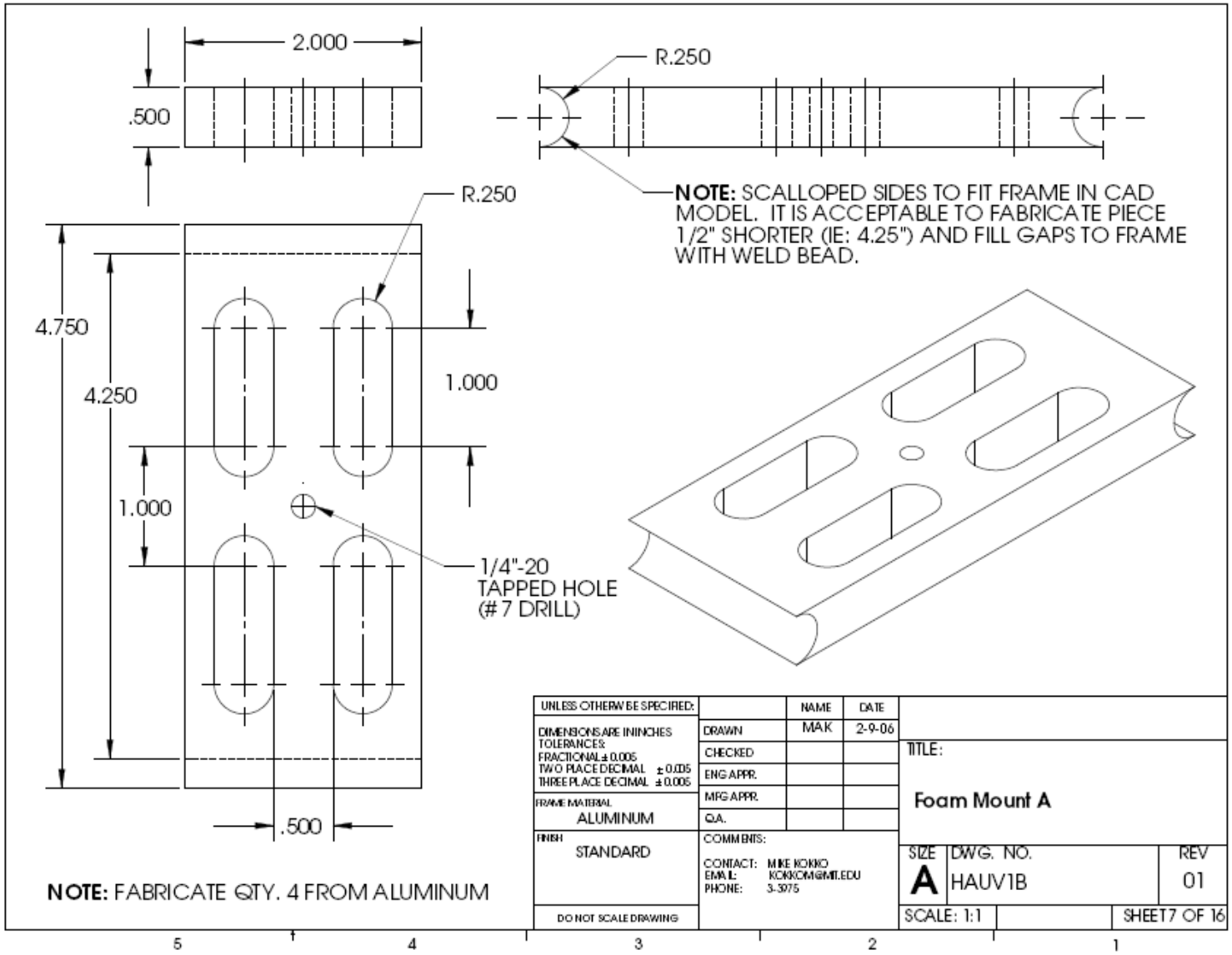
2.000
.500
R.250
NOTE: SCALLOPED SIDES TO FIT FRAME IN CAD MODEL. IT IS ACCEPTABLE TO FABRICATE PIECE 1/2" SHORTER (IE: 4.25") AND FILL GAPS TO FRAME WITH WELD BEAD.
R.250
4.750
4.250
1.000
1.000
1/4"-20
TAPPED HOLE
(#7 DRILL)
.500
NOTE: FABRICATE QTY. 4 FROM ALUMINUM
UNLESS OTHERWISE SPECIFIED:
DIMENSIONS ARE IN INCHES
TOLERANCES:
FRACTIONAL ± 0.005
TWO PLACE DECIMAL ± 0.005
THREE PLACE DECIMAL ± 0.005
FRAME MATERIAL
ALUMINUM
FINISH
STANDARD
DO NOT SCALE DRAWING
NAME
DATE
DRAWN
MAK
2-9-06
CHECKED
ENG APPR.
MFG APPR.
Q.A.
COMMENTS:
CONTACT: MIKE KOKKO
EMAIL: KOKKOM@MIT.EDU
PHONE: 3-3975
TITLE:
Foam Mount A
SIZE
A
DWG. NO.
HAUV1B
REV
01
SCALE: 1:1
SHEET 7 OF 16
5
4
3
2
1

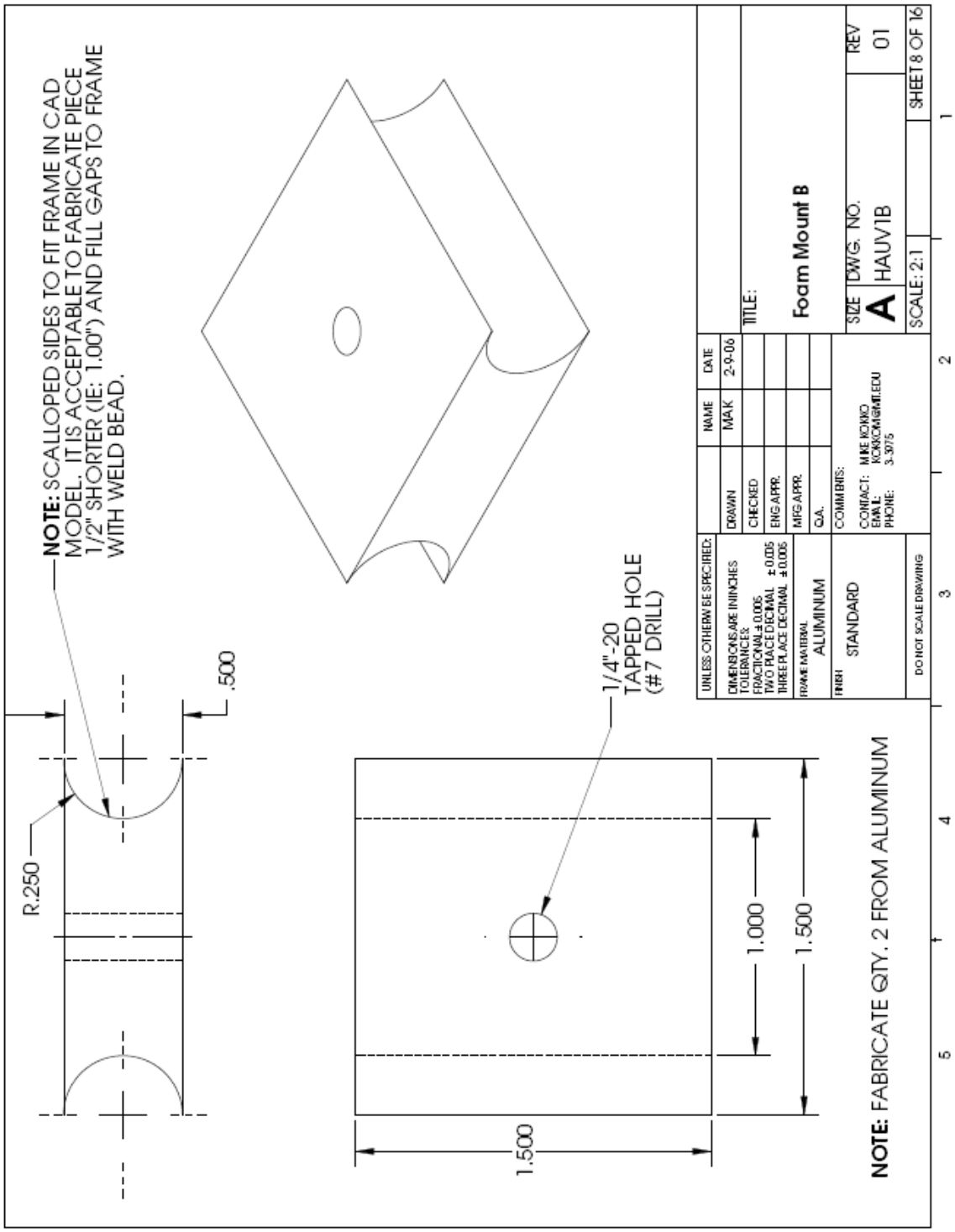
NOTE: SCALLOPED SIDES TO FIT FRAME IN CAD MODEL. IT IS ACCEPTABLE TO FABRICATE PIECE 1/2" SHORTER (IE: 1.00") AND FILL GAPS TO FRAME WITH WELD BEAD.
R.250
.500
1/4"-20 TAPPED HOLE (#7 DRILL)
1.000
1.500
1.500
NOTE: FABRICATE QTY. 2 FROM ALUMINUM
UNLESS OTHERWISE SPECIFIED:
DIMENSIONS ARE IN INCHES
TOLERANCES:
FRACTIONAL ± 0.005
TWO PLACE DECIMAL ± 0.005
THREE PLACE DECIMAL ± 0.005
FRAME MATERIAL
ALUMINUM
FINISH
STANDARD
DO NOT SCALE DRAWING
NAME
DATE
DRAWN
MAK
2-9-06
CHECKED
ENG APPR.
MFG APPR.
Q.A.
COMMENTS:
CONTACT: MIKE NOWKO
EMAIL: NOWKO@GMAIL.EDU
PHONE: 3-3975
TITLE:
Foam Mount B
SIZE
A
DWG. NO.
HAUV1B
REV
01
SCALE: 2:1
SHEET 8 OF 16

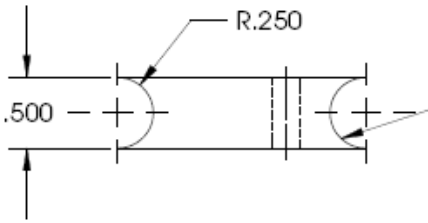

NOTE: SCALLOPED SIDES TO FIT FRAME IN CAD MODEL. IT IS ACCEPTABLE TO FABRICATE PIECE 1/2" SHORTER (IE: 1.25" x 1.25") AND FILL GAPS TO FRAME WITH WELD BEAD.

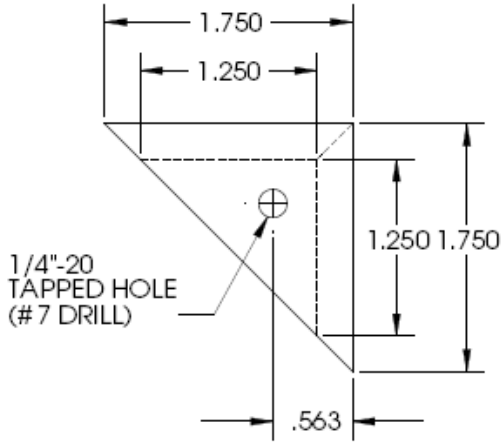

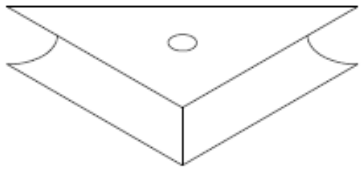

NOTE: FABRICATE QTY. 2 FROM ALUMINUM

UNLESS OTHERWISE SPECIFIED:		NAME	DATE
DIMENSIONS ARE IN INCHES TOLERANCES: FRACTIONAL ± 0.005 TWO PLACE DECIMAL ± 0.005 THREE PLACE DECIMAL ± 0.005	DRAWN	MAK	2-9-06
	CHECKED		
	ENG APPR.		
	MFG APPR.		
FRAME MATERIAL ALUMINUM	Q.A.		
FINISH STANDARD	COMMENTS: CONTACT: MIKE KOKKO EMAIL: KOKKOM@MIT.EDU PHONE: 3-3075		
DO NOT SCALE DRAWING			

TITLE:

Foam Mount C

SIZE	DWG. NO.	REV
A	HAUV1B	01

SCALE: 1:1 | SHEET 9 OF 16

5 4 3 2 1

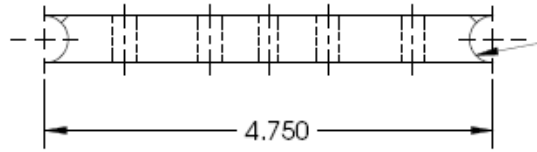

NOTE: SCALLOPED SIDES TO FIT FRAME IN CAD MODEL. IT IS ACCEPTABLE TO FABRICATE PIECE SHORTER (IE: 1.75" x 4.25") AND FILL GAPS TO FRAME WITH WELD BEAD.

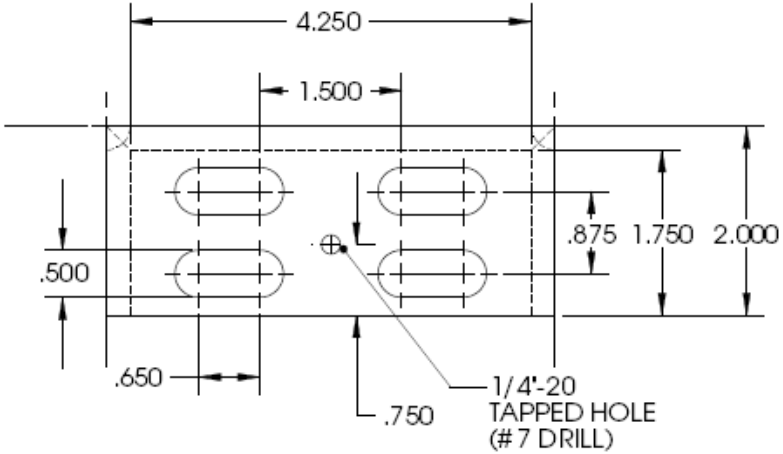

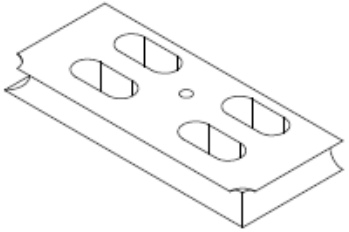

NOTE: FABRICATE QTY. 2 FROM ALUMINUM

UNLESS OTHERWISE SPECIFIED:		NAME	DATE
DIMENSIONS ARE IN INCHES TOLERANCES: FRACTIONAL ± 0.005 TWO PLACE DECIMAL ± 0.005 THREE PLACE DECIMAL ± 0.005	DRAWN	MAK	2-9-06
	CHECKED		
	ENG APPR.		
	MFG APPR.		
FRAME MATERIAL ALUMINUM	Q.A.		
FINISH STANDARD	COMMENTS: CONTACT: MIKE KOKKO EMAIL: KOKKOM@MIT.EDU PHONE: 3-3975		
DO NOT SCALE DRAWING			

TITLE:

Foam Mount D

SIZE	DWG. NO.	REV
A	HAUV1B	01

SCALE: 2:3 | SHEET 10 OF 16

5 4 3 2 1

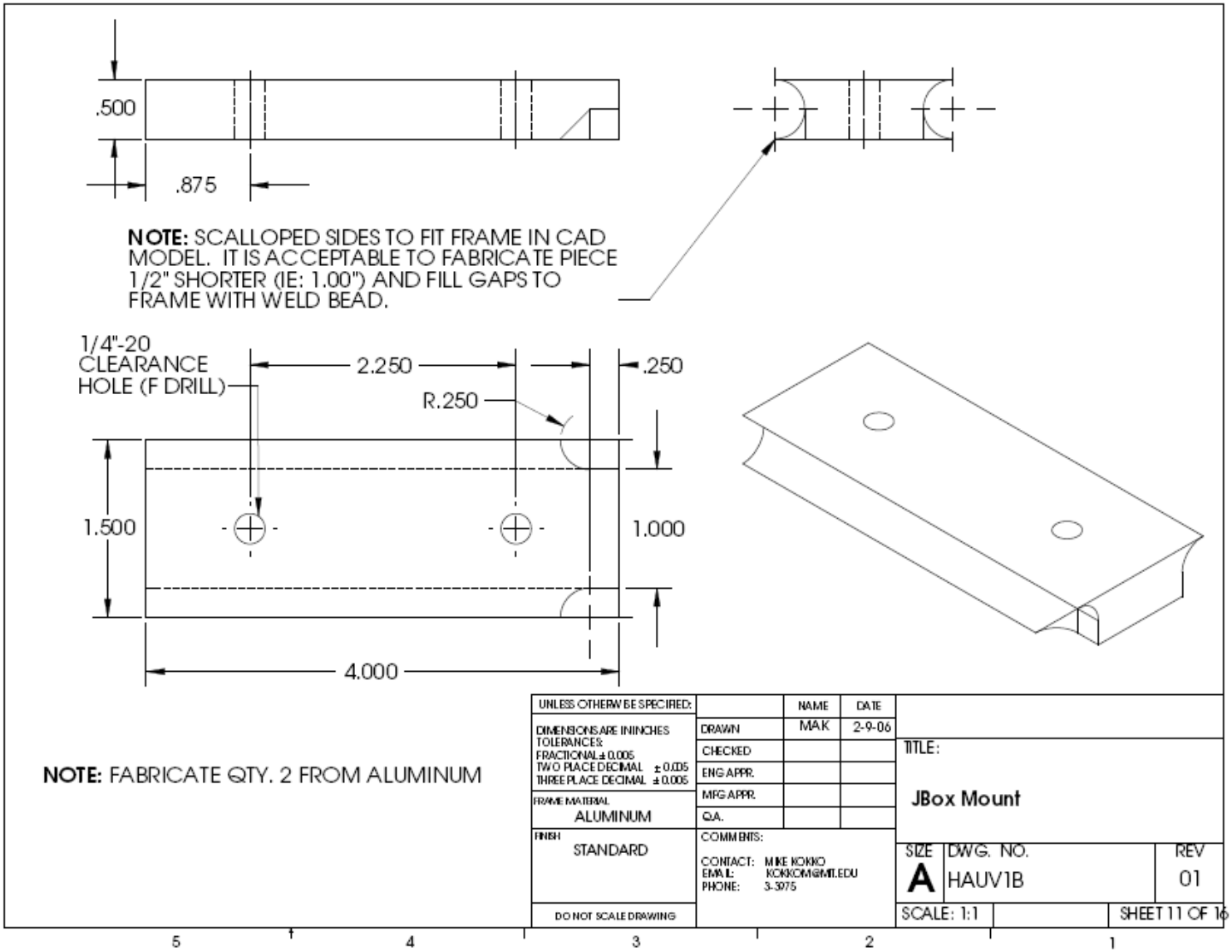
.500
.875
NOTE: SCALLOPED SIDES TO FIT FRAME IN CAD MODEL. IT IS ACCEPTABLE TO FABRICATE PIECE 1/2" SHORTER (IE: 1.00") AND FILL GAPS TO FRAME WITH WELD BEAD.
1/4"-20 CLEARANCE HOLE (F DRILL)
2.250
.250
R.250
1.500
1.000
4.000
NOTE: FABRICATE QTY. 2 FROM ALUMINUM
UNLESS OTHERWISE SPECIFIED:
DIMENSIONS ARE IN INCHES
TOLERANCES:
FRACTIONAL ± 0.005
TWO PLACE DECIMAL ± 0.005
THREE PLACE DECIMAL ± 0.005
FRAME MATERIAL
ALUMINUM
FINISH
STANDARD
DO NOT SCALE DRAWING
NAME
DATE
DRAWN
MAK
2-9-06
CHECKED
ENG APPR.
MFG APPR.
Q.A.
COMMENTS:
CONTACT: MIKE KOKKO
EMAIL: KOKKOM@MIT.EDU
PHONE: 3-3975
TITLE:
JBox Mount
SIZE
A
DWG. NO.
HAUV1B
REV
01
SCALE: 1:1
SHEET 11 OF 16
5
4
3
2
1

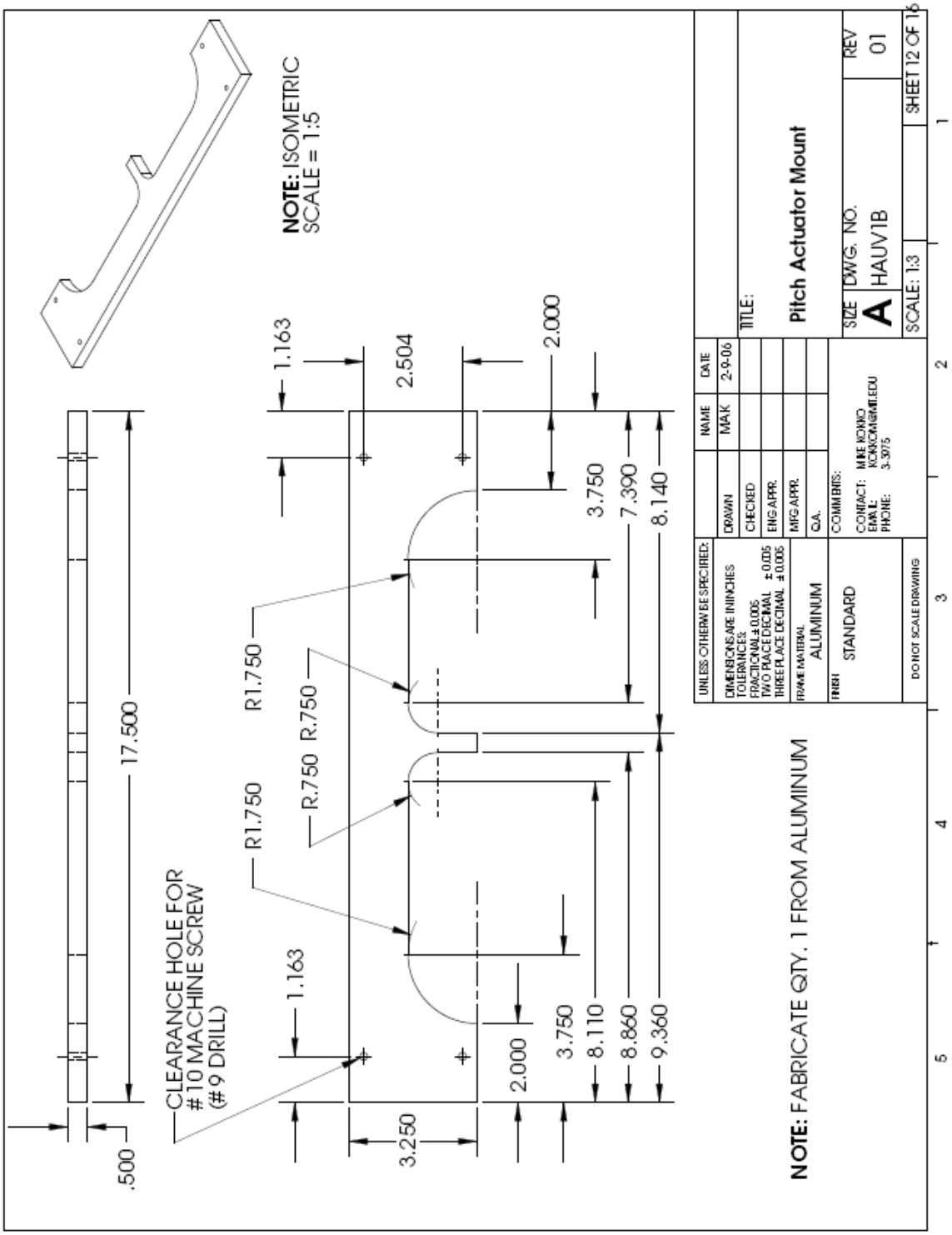
NOTE: ISOMETRIC
SCALE = 1:5
1.163
2.504
2.000
3.750
7.390
8.140
R1.750
R.750
R.750
R1.750
17.500
CLEARANCE HOLE FOR
#10 MACHINE SCREW
(#9 DRILL)
1.163
3.250
2.000
3.750
8.110
8.860
9.360
.500
NOTE: FABRICATE QTY. 1 FROM ALUMINUM
UNLESS OTHERWISE SPECIFIED:
DIMENSIONS ARE IN INCHES
TOLERANCES:
FRACTIONAL ± 0.005
TWO PLACE DECIMAL ± 0.005
THREE PLACE DECIMAL ± 0.005
FRAME MATERIAL
ALUMINUM
FINISH
STANDARD
DO NOT SCALE DRAWING
NAME
DATE
DRAWN
MAK
2-9-06
CHECKED
ENG APPR.
MFG APPR.
Q.A.
COMMENTS:
CONTACT: MIKE KONKO
EMAIL: KONKO@MIT.EDU
PHONE: 3-3075
TITLE:
Pitch Actuator Mount
SIZE
A
DWG. NO.
HAUV1B
REV
01
SCALE: 1:3
SHEET 12 OF 16

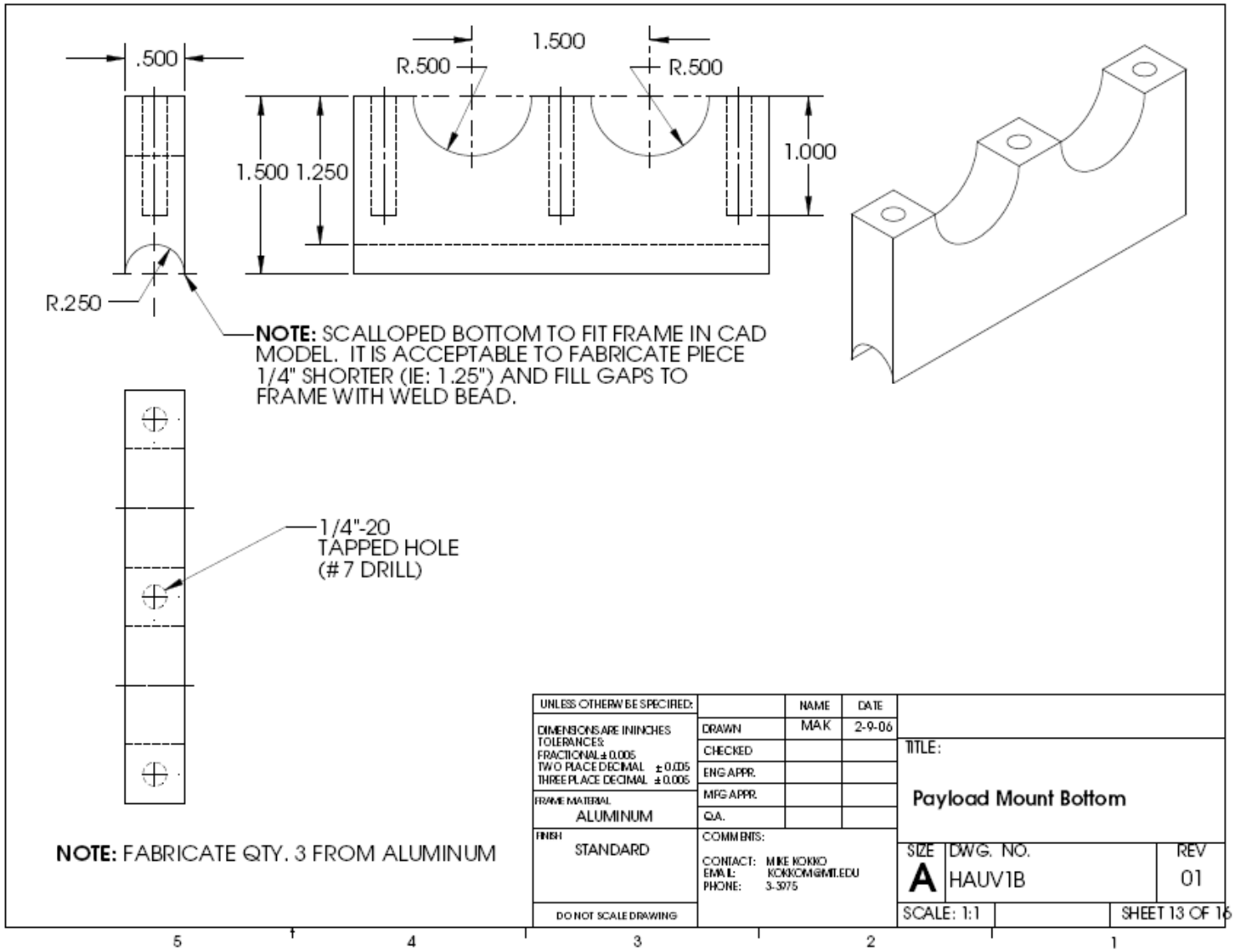
.500
1.500
R.500
R.500
1.500 1.250
1.000
R.250
NOTE: SCALLOPED BOTTOM TO FIT FRAME IN CAD MODEL. IT IS ACCEPTABLE TO FABRICATE PIECE 1/4" SHORTER (IE: 1.25") AND FILL GAPS TO FRAME WITH WELD BEAD.
1/4"-20 TAPPED HOLE (#7 DRILL)
NOTE: FABRICATE QTY. 3 FROM ALUMINUM
UNLESS OTHERWISE SPECIFIED:
DIMENSIONS ARE IN INCHES
TOLERANCES:
FRACTIONAL ± 0.005
TWO PLACE DECIMAL ± 0.005
THREE PLACE DECIMAL ± 0.005
FRAME MATERIAL
ALUMINUM
FINISH
STANDARD
DO NOT SCALE DRAWING
NAME
DATE
DRAWN
M.A.K.
2-9-06
CHECKED
ENG APPR.
MFG APPR.
Q.A.
COMMENTS:
CONTACT: MIKE KOKKO
EMAIL: KOKKOM@MIT.EDU
PHONE: 3-3075
TITLE:
Payload Mount Bottom
SIZE
A
DWG. NO.
HAUV1B
REV
01
SCALE: 1:1
SHEET 13 OF 16
5
4
3
2
1

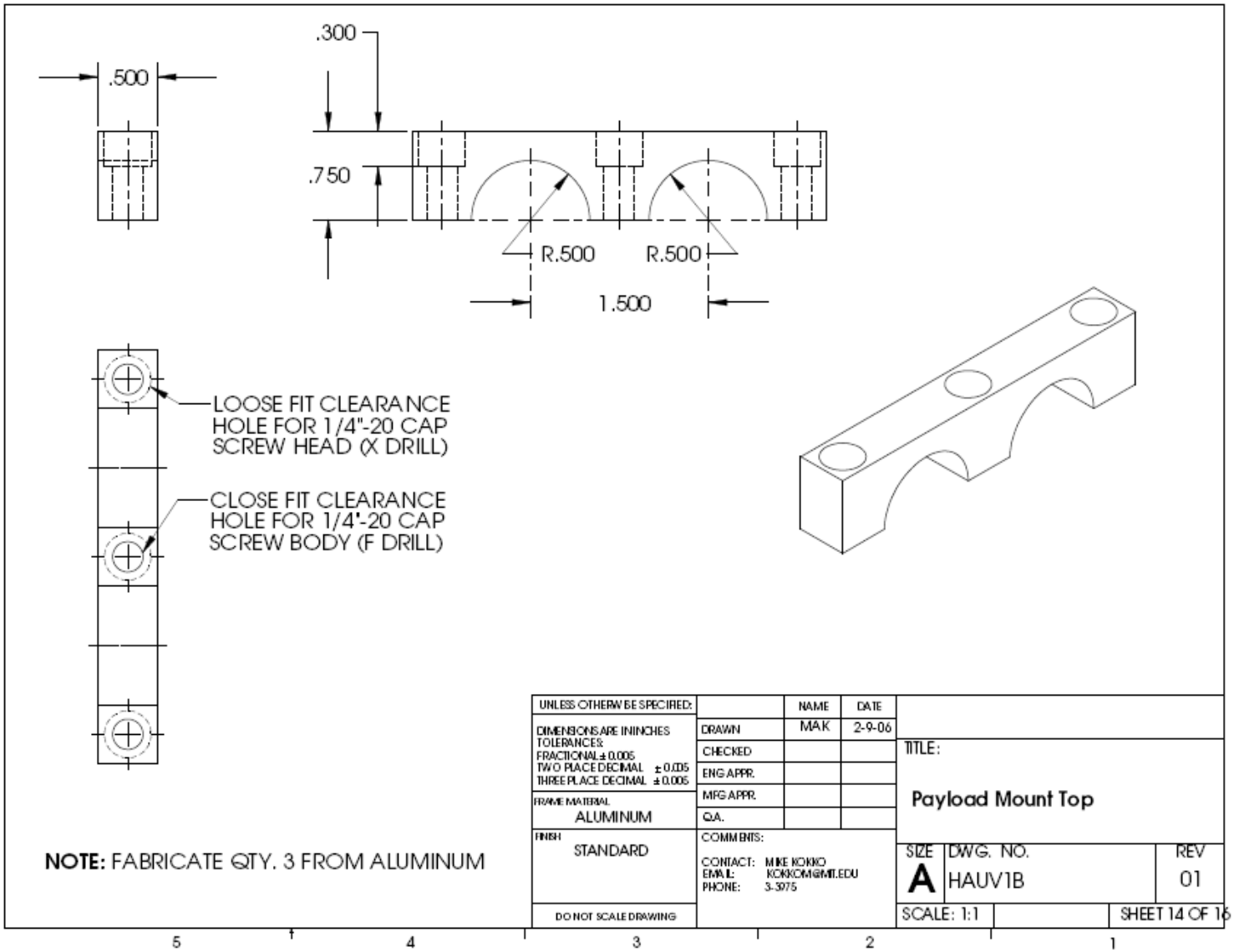
.500
.300
.750
R.500
R.500
1.500
LOOSE FIT CLEARANCE HOLE FOR 1/4"-20 CAP SCREW HEAD (X DRILL)
CLOSE FIT CLEARANCE HOLE FOR 1/4"-20 CAP SCREW BODY (F DRILL)
NOTE: FABRICATE QTY. 3 FROM ALUMINUM
UNLESS OTHERWISE SPECIFIED:
DIMENSIONS ARE IN INCHES
TOLERANCES:
FRACTIONAL ± 0.005
TWO PLACE DECIMAL ± 0.005
THREE PLACE DECIMAL ± 0.005
FRAME MATERIAL
ALUMINUM
FINISH
STANDARD
DO NOT SCALE DRAWING
NAME
DATE
DRAWN
MAK
2-9-06
CHECKED
ENG APPR.
MFG APPR.
Q.A.
COMMENTS:
CONTACT: MIKE KOKKO
EMAIL: KOKKOM@MIT.EDU
PHONE: 3-3975
TITLE:
Payload Mount Top
SIZE
A
DWG. NO.
HAUV1B
REV
01
SCALE: 1:1
SHEET 14 OF 16
5
4
3
2
1

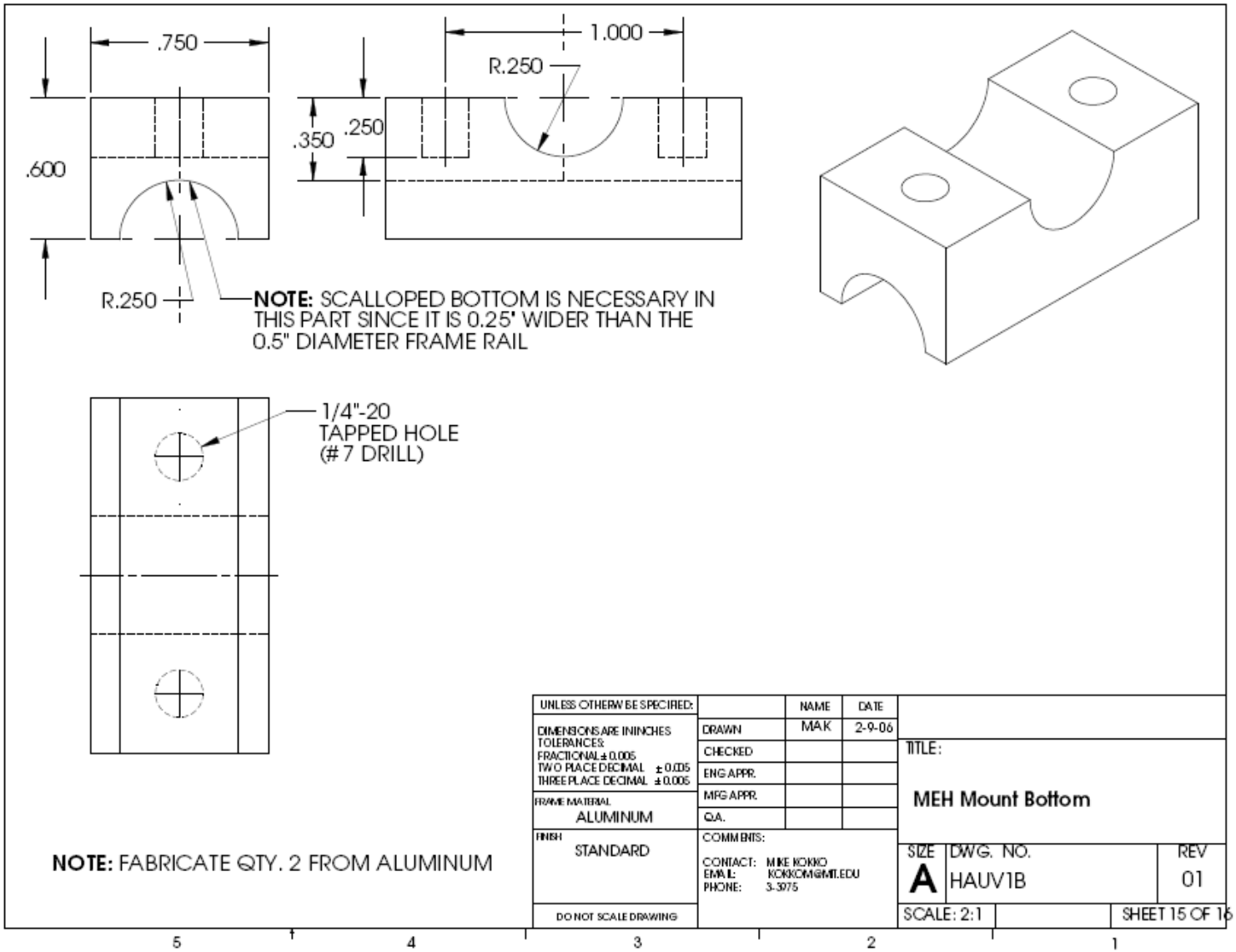
.750
.600
R.250
1.000
R.250
.350
.250
NOTE: SCALLOPED BOTTOM IS NECESSARY IN THIS PART SINCE IT IS 0.25" WIDER THAN THE 0.5" DIAMETER FRAME RAIL
1/4"-20 TAPPED HOLE (#7 DRILL)
NOTE: FABRICATE QTY. 2 FROM ALUMINUM
UNLESS OTHERWISE SPECIFIED:
DIMENSIONS ARE IN INCHES
TOLERANCES:
FRACTIONAL ± 0.005
TWO PLACE DECIMAL ± 0.005
THREE PLACE DECIMAL ± 0.005
FRAME MATERIAL
ALUMINUM
FINISH
STANDARD
DO NOT SCALE DRAWING
NAME
DATE
DRAWN
MAK
2-9-06
CHECKED
ENG APPR.
MFG APPR.
Q.A.
COMMENTS:
CONTACT: MIKE KOKKO
EMAIL: KOKKOM@MIT.EDU
PHONE: 3-3975
TITLE:
MEH Mount Bottom
SIZE
A
DWG. NO.
HAUV1B
REV
01
SCALE: 2:1
SHEET 15 OF 16
5
4
3
2
1

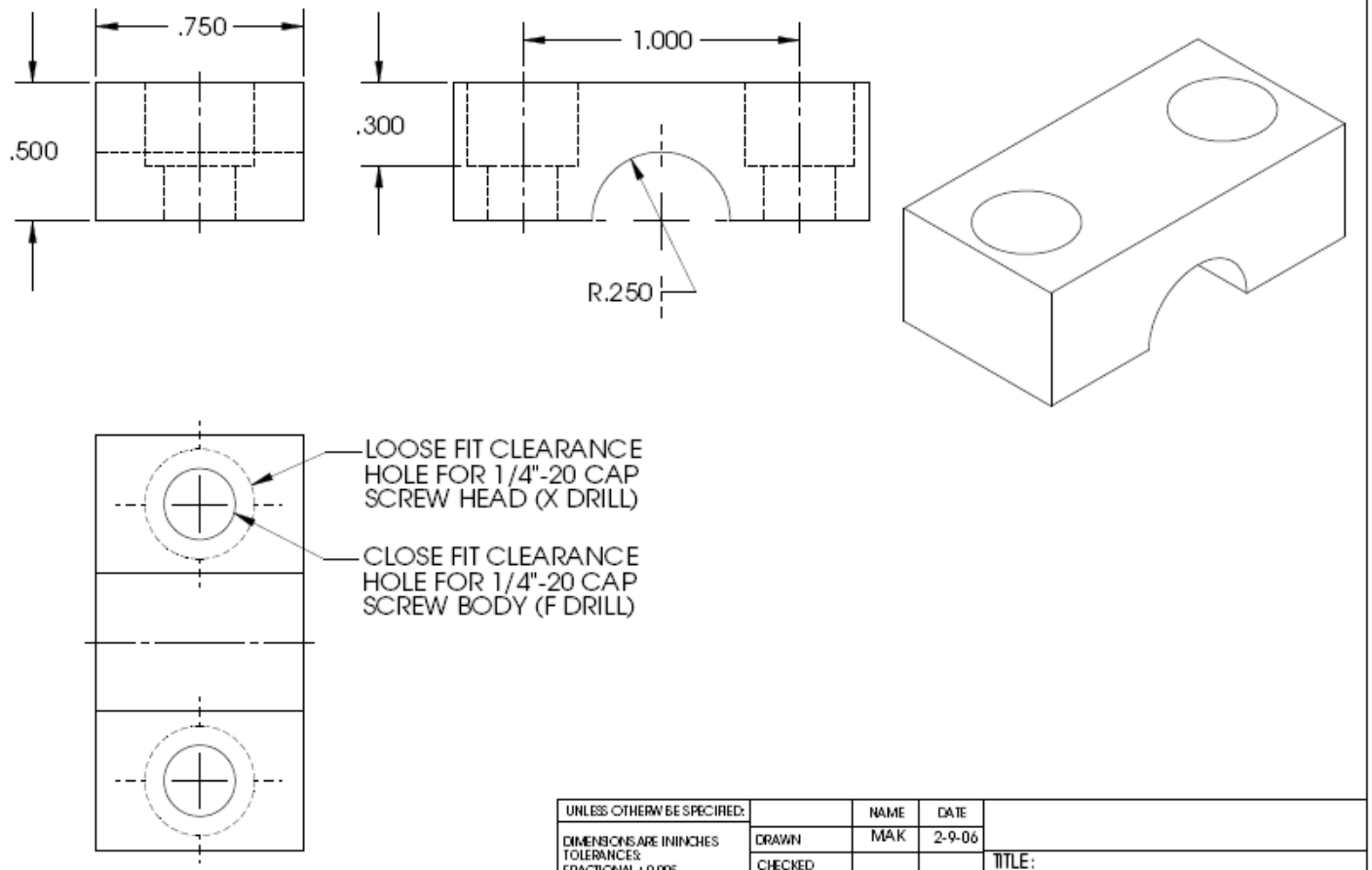

NOTE: FABRICATE QTY. 2 FROM ALUMINUM

UNLESS OTHERWISE SPECIFIED:		NAME	DATE
DIMENSIONS ARE IN INCHES TOLERANCES: FRACTIONAL ± 0.005 TWO PLACE DECIMAL ± 0.005 THREE PLACE DECIMAL ± 0.005	DRAWN	MAK	2-9-06
	CHECKED		
	ENG APPR.		
	MFG APPR.		
FRAME MATERIAL ALUMINUM	Q.A.		
FINISH STANDARD	COMMENTS: CONTACT: MIKE KOKKO EMAIL: KOKKOM@MIT.EDU PHONE: 3-3075		
DO NOT SCALE DRAWING			

TITLE:

MEH Mount Top

SIZE	DWG. NO.	REV
A	HAUV1B	01

SCALE: 2:1 | SHEET 16 OF 16

5 4 3 2 1

Appendix B

Raft CAD Drawings

Note: The CAD drawings on the following pages are not reproduced in this document at their indicated scales.

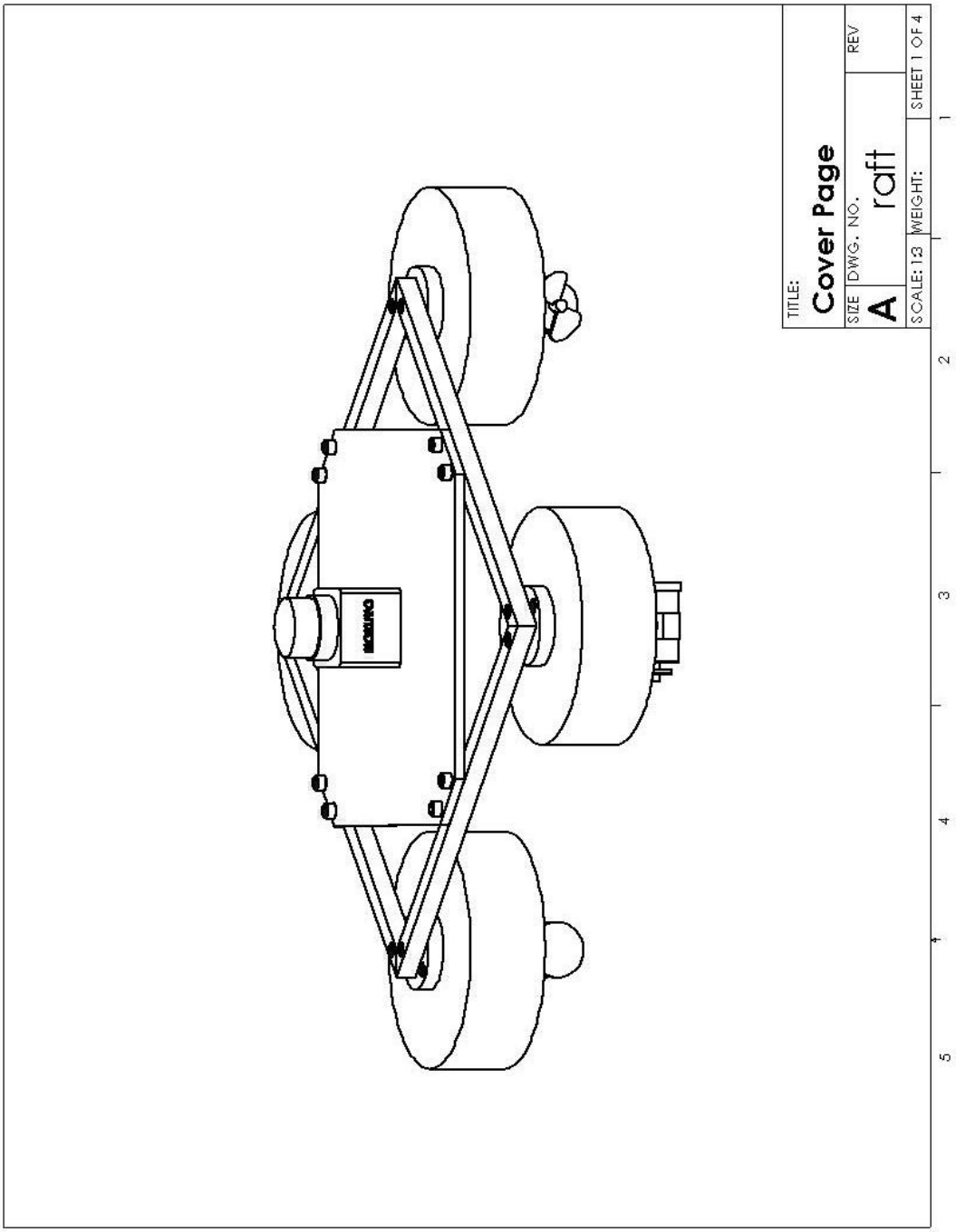
TITLE:
Cover Page
SIZE
A
DWG. NO.
raft
REV
SCALE: 1:3
WEIGHT:
SHEET 1 OF 4

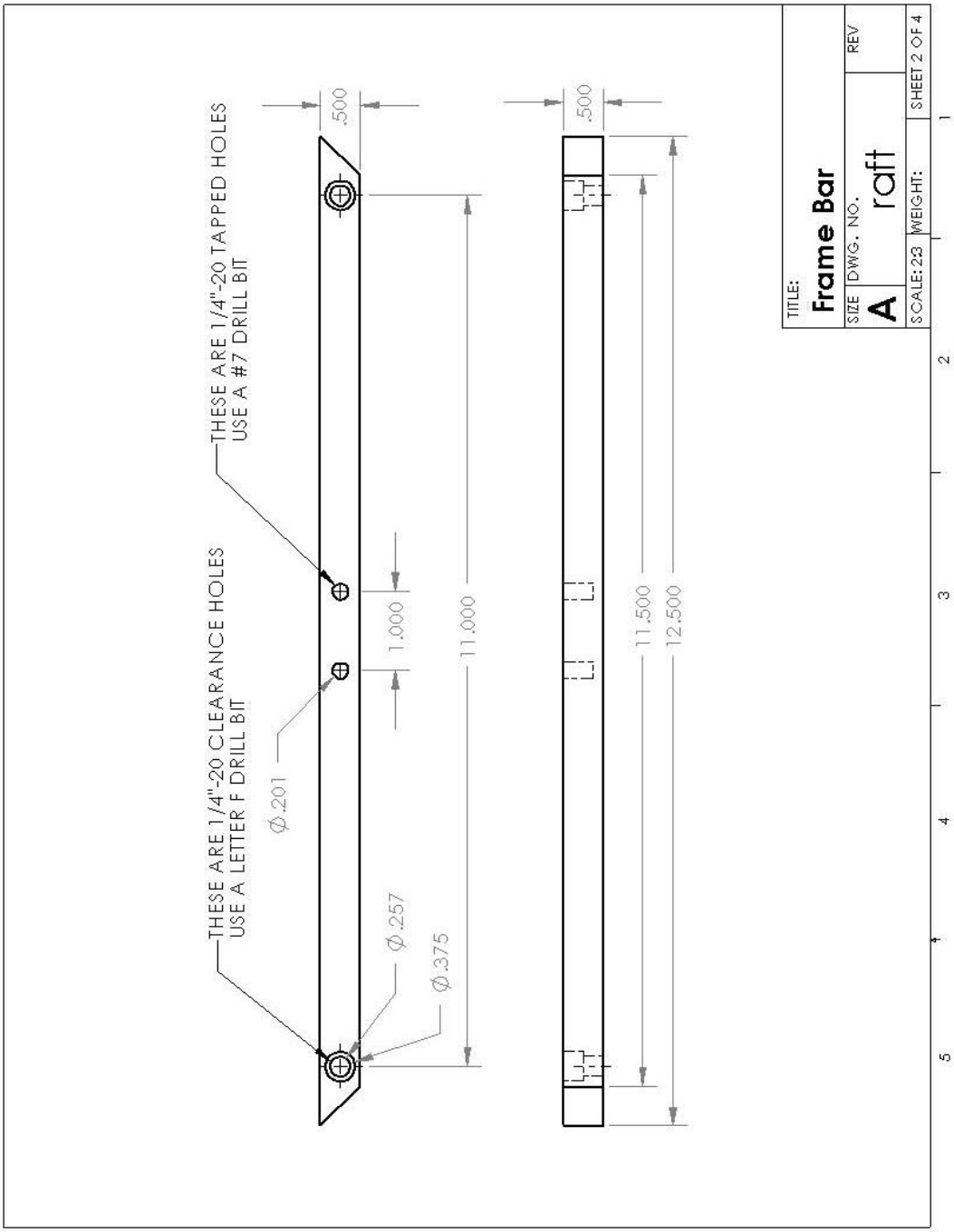
THESE ARE 1/4"-20 TAPPED HOLES
USE A #7 DRILL BIT
THESE ARE 1/4"-20 CLEARANCE HOLES
USE A LETTER F DRILL BIT
.500
.500
1.000
11.000
11.500
12.500
Ø.201
Ø.257
Ø.375
TITLE:
Frame Bar
SIZE
A
DWG. NO.
raft
REV
SCALE: 2:3
WEIGHT:
SHEET 2 OF 4

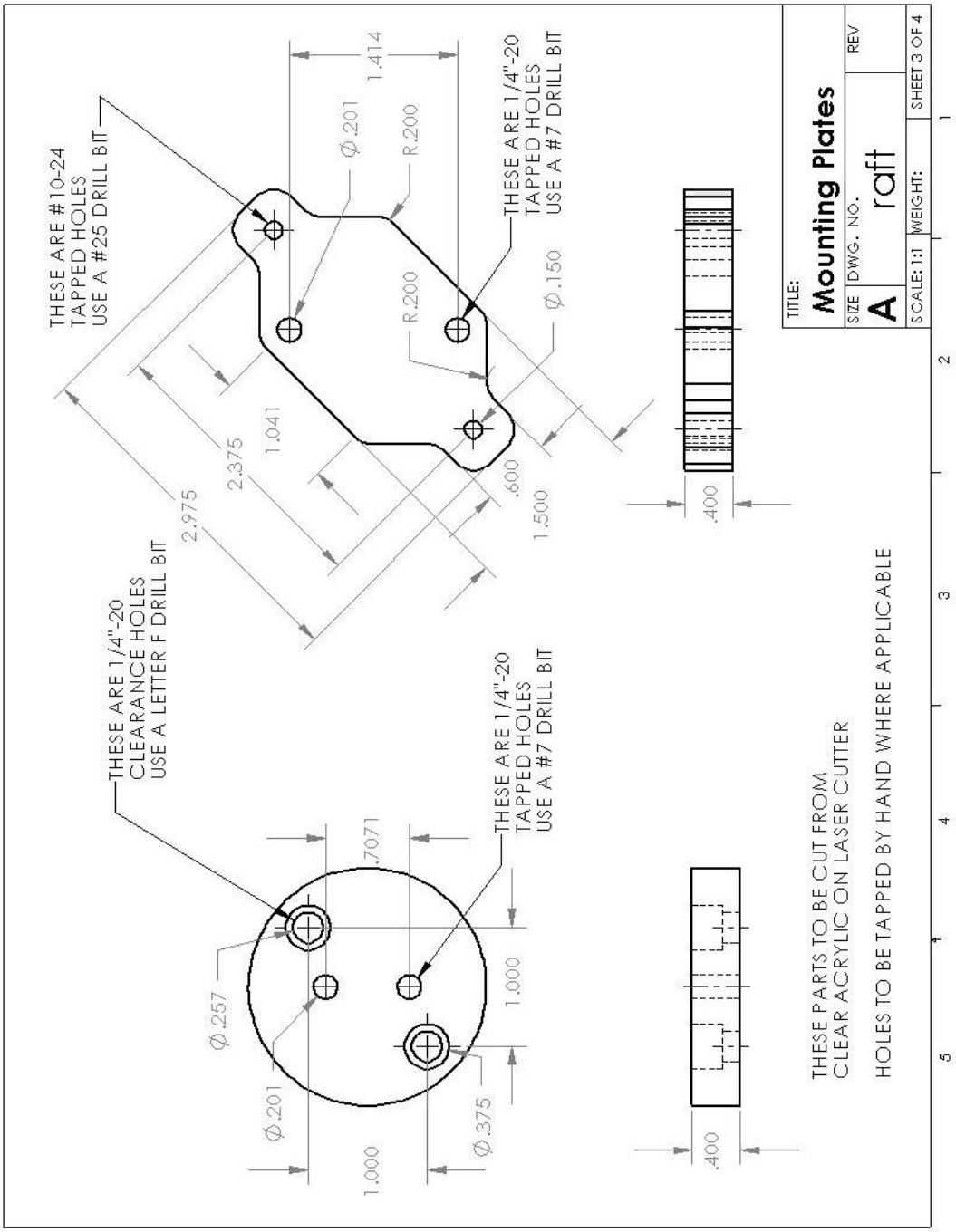
THESE ARE #10-24
TAPPED HOLES
USE A #25 DRILL BIT
THESE ARE 1/4"-20
TAPPED HOLES
USE A #7 DRILL BIT
THESE ARE 1/4"-20
CLEARANCE HOLES
USE A LETTER F DRILL BIT
THESE ARE 1/4"-20
TAPPED HOLES
USE A #7 DRILL BIT
Ø.201
R.200
R.200
Ø.150
1.414
1.041
2.375
2.975
.600
1.500
.400
.7071
Ø.257
Ø.201
1.000
1.000
Ø.375
.400
THESE PARTS TO BE CUT FROM
CLEAR ACRYLIC ON LASER CUTTER
HOLES TO BE TAPPED BY HAND WHERE APPLICABLE
TITLE:
Mounting Plates
SIZE
A
DWG. NO.
raft
REV
SCALE: 1:1
WEIGHT:
SHEET 3 OF 4

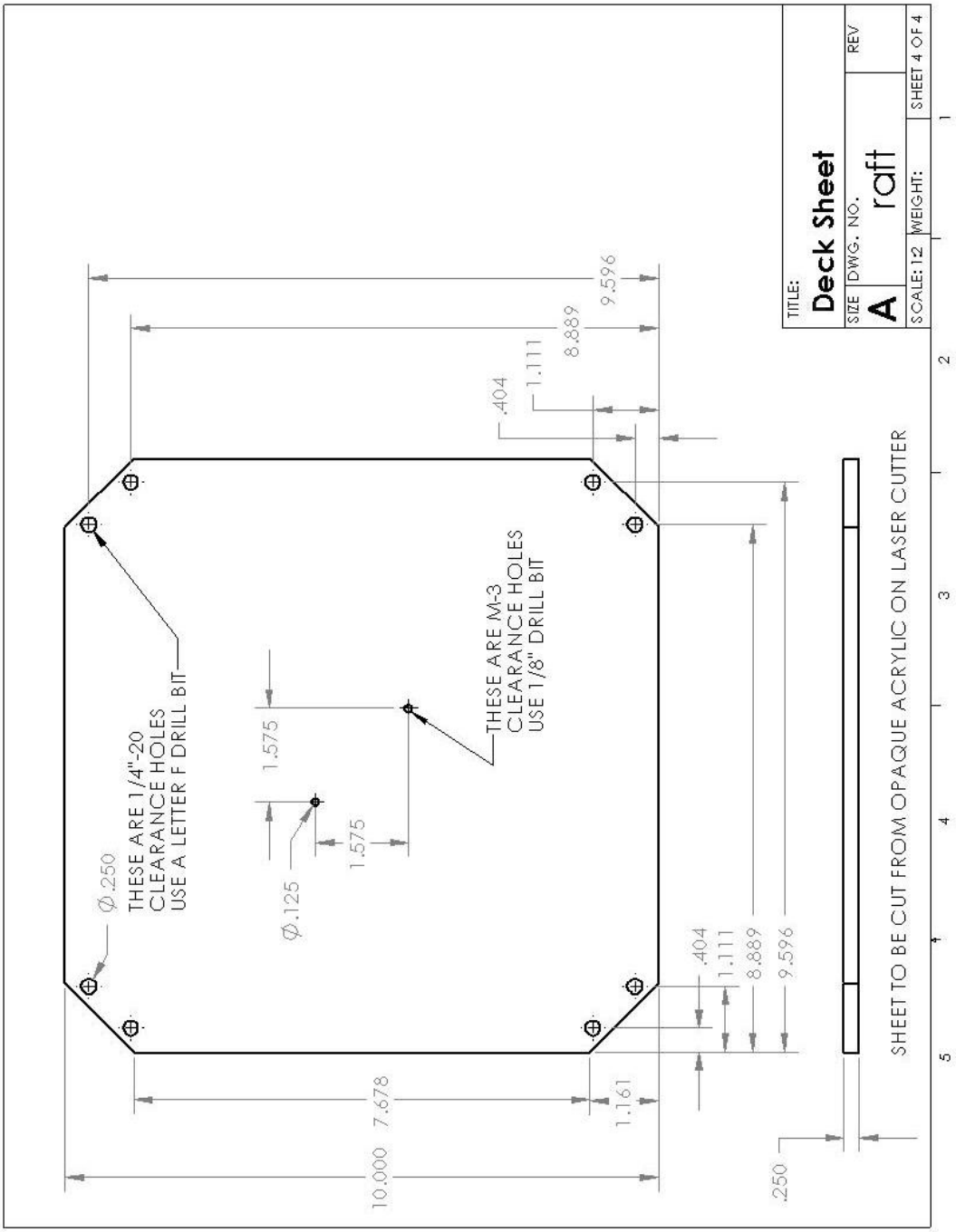
TITLE:
Deck Sheet
SIZE
A
DWG. NO.
raft
REV
SCALE: 1:2
WEIGHT:
SHEET 4 OF 4
THESE ARE 1/4"-20
CLEARANCE HOLES
USE A LETTER F DRILL BIT
Ø.250
Ø.125
1.575
1.575
THESE ARE M-3
CLEARANCE HOLES
USE 1/8" DRILL BIT
.404
1.111
8.889
9.596
.404
1.111
8.889
9.596
10.000
7.678
1.161
.250
SHEET TO BE CUT FROM OPAQUE ACRYLIC ON LASER CUTTER

Appendix C

Motor Controller Schematic

Raft Motor Controller V2.0

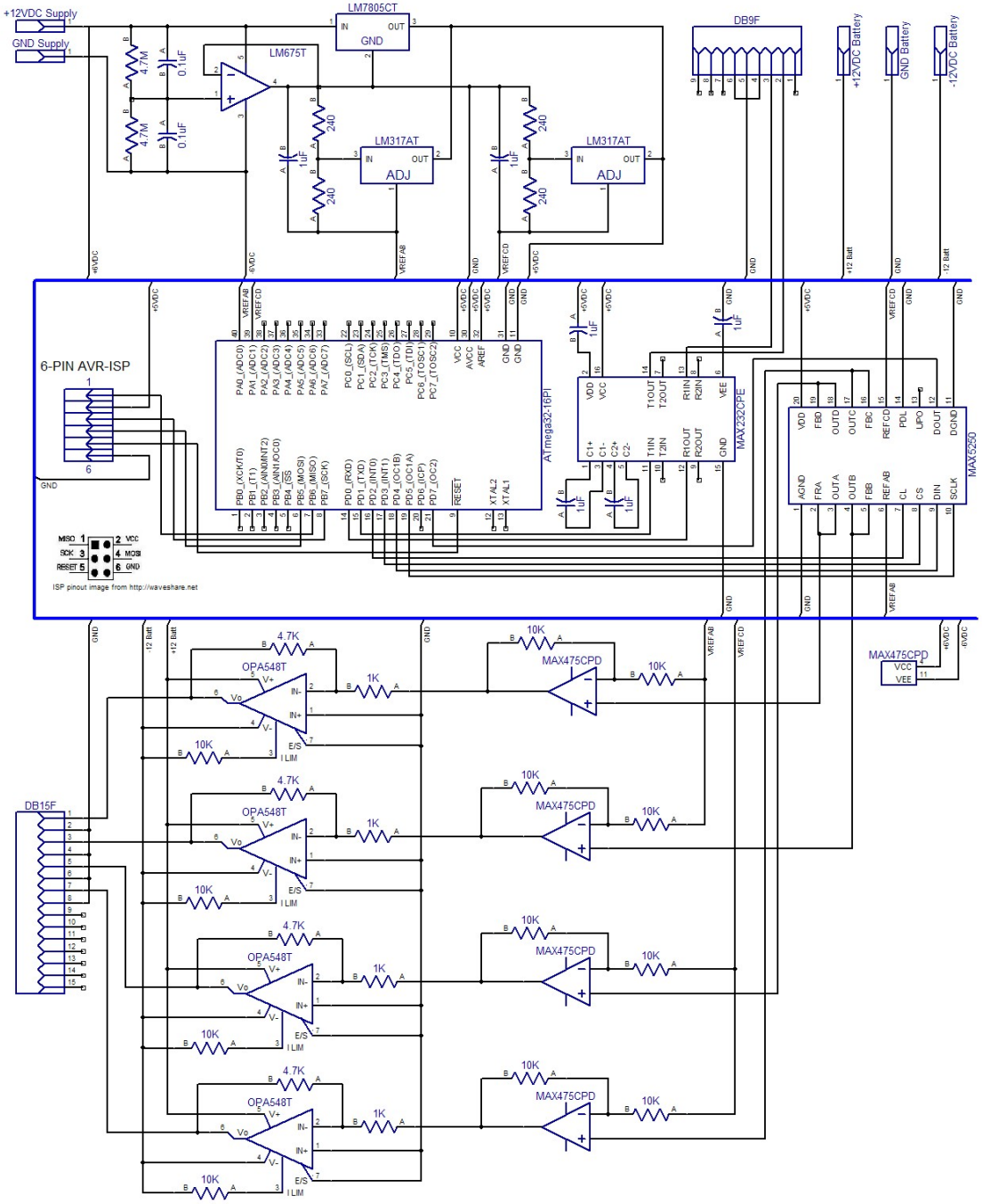

Note: Include 0.1uF capacitors between +5VDC and GND near all power connections.

Bibliography

[1] Richard O. Duda and Peter E. Hart. Use of the hough transformation to detect lines and curves in pictures. *Communications of the ACM*, 15(1):11–15, 1972.

[2] Hugh Durrant-Whyte. Localisation, Mapping and the Simultaneous Localisation and Mapping (SLAM) Problem. In *SLAM Summer School 2002*, August 2002. http://www.cas.kth.se/SLAM/Presentations/hdw-slides.pdf.

[3] R. Eustice, O. Pizarro, and H. Singh. Visually Augmented Navigation in an Unstructured Environment Using a Delayed State History. In *Proceedings of the 2004 IEEE International Conference on Robotics and Automation*, volume 1, pages 25–32, New Orleans, USA, April 2004.

[4] Ryan M. Eustice, Hanumant Singh, John J. Leonard, and Matthew R. Walter. Visually mapping the RMS Titanic: conservative covariance estimates for SLAM information filters. *Intl. J. Robotics Reserach*, 25(12):1223–1242, 2006.

[5] Hans Jacob S. Feder, John J. Leonard, and Christopher M. Smith. Adaptive mobile robot navigation and mapping. *The International Journal of Robotics Research*, 18(7), July 1999.

[6] Arthur Gelb, editor. *Applied Optimal Estimation*. The M.I.T. Press, Cambridge, 1974.

[7] Hayato Kondo and Tamaki Ura. Underwater structure observation by the AUV with laser pointing device. In *Underwater Technology, 2002. Proceedings of the 2002 International Symposium on*, page 178, 2002.

[8] Hayato Kondo and Tamaki Ura. Navigation of an AUV for investigation of underwater structures. *Control Engineering Practice*, 12(12):1551–1559, December 2004.

[9] R. Madhavan and H. F. Durrant-Whyte. Natural landmark-based autonomous vehicle navigation. *Robotics and Autonomous Systems*, 46(2):79–95, February 2004.

[10] Bradley A. Moran, John J. Leonard, and Chryssostomos Chryssostomidis. Curved shape reconstruction using multiple hypothesis tracking. *Oceanic Engineering, IEEE Journal of*, 22(4):625–638, 1997.

[11] William H. Press, William T. Vetterling, Saul A. Teukolsky, and Brian P. Flannery. *Numerical Recipes in C++: the art of scientific computing*. Cambridge University Press, Cambridge, UK, 2002.

[12] A. S. Sekmen and B. Barshan. Estimation of object location and radius of curvature using ultrasonic sonar. *Applied Acoustics*, 62(7):841–865, July 2001.

[13] S. M. A. Sharkh, S. H. Lai, and S. R. Turnock. Structurally integrated brushless PM motor for miniature propeller thrusters. *Electrical Power Applications, IEE Proceedings*, 151(5):513 – 519, 2004. SP: - 513.

[14] Gilbert Strang. *Introduction to Applied Mathematics*. Wellesley-Cambridge Press, Wellesley, MA, 1986.

[15] Juan D Tardos, Jose Neira, Paul M Newman, and John J Leonard. Robust mapping and localization in indoor environments using sonar data. *The International Journal of Robotics Research*, 21(4):311–330, 2002.

[16] Robert J. Urick. *Principles of Underwater Sound*. Peninsula Publishing, Los Altos, CA, third edition, 1983.

[17] Jerome Vaganay, Mike Elkins, Dave Esposito, Will O'Halloran, Franz Hover, and Mike Kokko. Ship Hull Inspection with the HAUV: US Navy and NATO Demonstration Results. In *Proceedings of IEEE / MTS Oceans 2006*, 2006.

[18] Jerome Vaganay, Mike Elkins, Scott Wilcox, Franz Hover, Rob Damus, Sam Desset, James Morash, and Victor Polidoro. Ship hull inspection by hull relative navigation and control. In *Proceedings of IEEE / MTS Oceans 2005*, 2005.

[19] L.L. Whitcomb, D.R. Yoerger, and H. Singh. Towards Precision Robotic Manuvering, Survey and Manipulation in Unstructured Undersea Environments. In *Robotics Research - The Eighth International Symposium*, pages 45–54, Springer Verlag, London, 1998.